

AD-A273 800



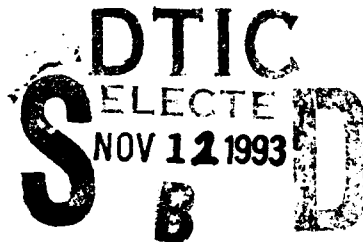
2

PL-TR-93-2012

Instrumentation Papers, No. 345

**REPORT ON OPERATIONS OF THE AIR FORCE  
GEOPHYSICS LABORATORY INFRARED  
ARRAY SPECTROMETER**

G. C. Sloan  
P. D. LeVan  
P. C. Tandy



25 January 1993

**APPROVED FOR PUBLIC RELEASE; DISTRIBUTION UNLIMITED**




**PHILLIPS LABORATORY  
Directorate of Geophysics  
AIR FORCE MATERIEL COMMAND  
HANSCom AIR FORCE BASE, MA 01731-3010**

**93-27655**



This technical report has been reviewed and is approved for publication

  
\_\_\_\_\_  
ROGER A. VAN TASSEL  
Division Director

  
\_\_\_\_\_  
STEPHAN D. PRICE  
Branch Chief

This report has been reviewed by the ESC Public Affairs Office (PA) and is releasable to the National Technical Information Service (NTIS).

Qualified requestors may obtain additional copies from the Defense Technical Information Center. All others should apply to the National Technical Information Service.

If your address has changed, or if you wish to be removed from the mailing list, or if the addressee is no longer employed by your organization, please notify PL/TSI, Hanscom AFB, MA 01731-3010. This will assist us in maintaining a current mailing list.

Do not return copies of this report unless contractual obligations or notices on a specific document requires that it be returned.

# REPORT DOCUMENTATION PAGE

Form Approved  
OMB No. 0704-0188

Public reporting burden for this collection of information is estimated to average 1 hour per response, including the time for reviewing instructions, searching existing data sources, gathering and maintaining the data needed, and completing and reviewing the collection of information. Send comments regarding this burden estimate or any other aspect of this collection of information, including suggestions for reducing this burden, to Washington Headquarters Service, Directorate for Information Operations and Reports, 1215 Jefferson Davis Highway, Suite 1204, Arlington, VA 22202-4302, and to the Office of Management and Budget, Paperwork Reduction Project (0704-0188), Washington, DC 20503.

1. AGENCY USE ONLY (Leave blank)		2. REPORT DATE 25 January 1993		3. REPORT TYPE AND DATES COVERED Scientific Final	
4. TITLE AND SUBTITLE  Report on Operations of the Air Force Geophysics Laboratory Infrared Array Spectrometer				5. FUNDING NUMBERS  PE: 61102F PR: 2311 TA: 2311G7 WU: 2311G701	
6. AUTHOR(S)  G.C. Sloan, P.D. LeVan, and P.C. Tandy					
7. PERFORMING ORGANIZATION NAME(S) AND ADDRESS(ES)  Phillips Laboratory/GPOB 29 Randolph Road Hanscom AFB, MA 01731-3010				8. PERFORMING ORGANIZATION REPORT NUMBER  PL-TR-93-2012 IP, No. 345	
9. SPONSORING/MONITORING AGENCY NAME(S) AND ADDRESS(ES)				10. SPONSORING/MONITORING AGENCY REPORT NUMBER	
11. SUPPLEMENTARY NOTES					
12a. DISTRIBUTION/AVAILABILITY STATEMENT  Approved for public release; Distribution unlimited				12b. DISTRIBUTION CODE	
13. ABSTRACT (Maximum 200 words)  We describe the Geophysics Laboratory Infrared Array Spectrometer, a long-slit spectrometer configured for astronomical observations at wavelengths of 7 to 14 $\mu$ m. We present the history of the instrument's development and use at the Wyoming Infrared Observatory, discuss some of the problems faced, and describe the resultant scientific publications. The appendices to this report contain several of the more important scientific publications.					
14. SUBJECT TERMS  Infrared astronomy Infrared spectroscopy Circumstellar dust				15. NUMBER OF PAGES 120	
				16. PRICE CODE	
17. SECURITY CLASSIFICATION OF REPORT  Unclassified	18. SECURITY CLASSIFICATION OF THIS PAGE  Unclassified	19. SECURITY CLASSIFICATION OF ABSTRACT  Unclassified	20. LIMITATION OF ABSTRACT  Same as Report		

## Contents

1. INTRODUCTION	1
2. ORIGINAL CONFIGURATION	1
3. FIRST OBSERVATIONS AT WIRO	2
4. IMPROVEMENTS TO THE SYSTEM	3
5. CULMINATION OF THE PROJECT	5
6. THE NEW ELECTRONICS	5
References	7
Appendix A: Ten-Micron Observations of Bright Circumstellar Shells —Spectral Properties and a Search for Extended Emission	11
Appendix B: Capabilities of the AFGL Mosaic Array Spectrometer —Ten-Micron Spectra of Bright Infrared Stars	23
Appendix C: Confirmation of Emission Features near 13 $\mu\text{m}$ ir. Spectra of RX Bootis and S Draconis	35
Appendix D: Spatial Structure in the 10 Micron Spectrum of HD 44179 (The Red Rectangle)	37
Appendix E: Introduction to: <i>Spatially Resolved 10 Micron Spectra of Circumstellar Material around Evolved Stars</i>	43
Appendix F: 8 - 14 Micron Spectroscopy of Carbon Stars Associated with Silicate Dust	63
Appendix G: Spatially Resolved Spectra of Silicate Dust Around $\alpha$ Orionis	69
Appendix H: Spatially Resolved Spectra of the Unidentified Infrared Features Around HD 44179 (The Red Rectangle)	75



## ACKNOWLEDGMENT

We are grateful to the Air Force Office of Scientific Research, especially Henry Radowski, for their financial commitment to this project. We also acknowledge the support of Stephan Price. The Wyoming Infrared Observatory donated large amounts of observing time, as well as the observing and technical assistance of their staff and students. Particularly significant were the expertise of Mel Dyke, Gary Grasdalen, and Ron Canterna, all of whom served as observatory directors during phases of this project.

DTIC QUALITY INSPECTED 6

Accession For	
NTIS GRA&I	<input checked="" type="checkbox"/>
DTIC TAB	<input type="checkbox"/>
Unannounced	<input type="checkbox"/>
Justification	
By _____	
Distribution/	
Availability Codes	
Dist	Avail and/or Special
A-1	

# **Report on Operations of the Air Force Geophysics Laboratory Infrared Array Spectrometer**

## **1. INTRODUCTION**

Ground-based infrared astronomy is limited to several discrete wavelength regions where atmospheric absorption is at a minimum. One of these windows, the N-band, runs from 7 to 14  $\mu\text{m}$  (the mid-infrared) and is ideal for the study of circumstellar dust shells. These dust shells are typically cool (300-500 K), and have spectral energy distributions that peak in the mid-infrared. For most of the brightest sources in the mid-infrared, emission from the circumstellar shell dominates the emission from the star itself. In addition, the strongest spectral features from these dust shells also appear in the 10  $\mu\text{m}$  window: the 10  $\mu\text{m}$  silicate feature, the 11.2  $\mu\text{m}$  SiC feature, and several of the unidentified infrared features (at 7.7, 8.6, 11.3, and 12.7  $\mu\text{m}$ ).

Prior to the development of infrared arrays, spectroscopic observations of these shells were made using a circularly variable filter-wheel and a single detector. The filter wheel was positioned to transmit a small range of wavelengths, a source would be observed, and the wheel would be rotated slightly for the next measurement. To cover the 7-14  $\mu\text{m}$  range at sufficient resolution was usually time consuming. Calibration of these observations could prove very difficult because of variations of atmospheric transmission with time. With the development of infrared arrays, observations could be made at all wavelengths simultaneously, dramatically improving the observing efficiency and also reducing the complications of calibration.

The Air Force Geophysics Laboratory (AFGL) array spectrometer, also known as GLADYS (for Geophysics Laboratory Array Detector Spectrometer), represents a further step forward. Before GLADYS, the only two-dimensional infrared arrays used for astronomical purposes made images of objects, usually in a narrow wavelength band. GLADYS is used as a long-slit spectrometer, allowing spectral and spatial data to be taken simultaneously. On the array, one axis is the spectral axis, while the other axis represents the spatial position in the slit.

## **2. ORIGINAL CONFIGURATION**

We present here a brief description of the instrument; more details can be found in LeVan and Tandy (1987), LeVan (1990, reprinted as Appendix B; 1991), and Sloan (1992, Chapter I, hereafter Appendix E).

The development of GLADYS began in the early 1980s. By 1984, Dr. Paul LeVan was directly responsible for the project, both in terms of design and supervision of construction. Early in the project, the decision was made to configure the instrument specifically for observations at the Wyoming Infrared Observatory (WIRO), a 2.3 meter reflecting telescope designed for infrared observations. Dr. LeVan designed the electronics and assisted Dr. Stephen Little in the optical design; Dr. LeVan, Peter Tandy, and Wentworth Institute of Technology in Boston built the electronics, while Sensor Systems Group in Waltham, Massachusetts constructed the optics. The detector chip, a 58 x 62 Si:Ga photoconductor array, was constructed by Santa Barbara Research Center. The array and optical workbench reside inside a dewar designed by Dr. Frank Low. Both the array and optics operate at liquid He temperature.

The spectrometer is a Czerny-Turner design, with a collimator mirror of focal length 270 mm and a camera mirror of focal length 75 mm. The mirrors re-image the  $f/27$  beam from the Cassegrain focus of the WIRO telescope to  $f/7.5$  on the array. Five additional folding mirrors are required to place the collimator one focal length from both the slit and the Lyot stop. All the mirrors are Ni-coated Al. A NaCl prism disperses the beam across the array. Originally, the prism was placed so that the short wavelength cut-off on the array was 8.5  $\mu\text{m}$ , but has since been shifted so that radiation from 7 to 14  $\mu\text{m}$  falls onto the array. The beam originally entered the dewar through a BaF<sub>1</sub> window, but this was later replaced with a ZnSe window, which provided better transmission near the red end of the 10  $\mu\text{m}$  window. The prism, window, and the seven Ni-coated Al mirrors have a total transmission of 0.55. The effective resolution ( $\lambda/\Delta\lambda$ ) of the instrument ranges from 50 at 7  $\mu\text{m}$  to 100 at 14  $\mu\text{m}$ .

The heart of GLADYS is a 58 x 62 Si:Ga array of photoconductors. The detectors are spaced 75  $\mu\text{m}$  apart, which translates to a detector spacing of 0.88 arcsec along the slit. The array is oriented with the 58-element axis along the slit and the 62-element axis along the dispersion direction, and it is bump-bonded to a CRC-228 Direct Read Out (DRO) multiplexer. Pixels are read in pairs with two parallel sets of electronics. To read one of the 1798 pixel pairs, the pair must first be addressed. Then the system samples the signal voltages, resets the pixels, samples the reset voltage, and passes the difference between signal and reset voltage to a 12-bit analog-digital convertor. Because these arrays are quickly saturated by the ambient emission, mostly from the telescope, they must be read very rapidly. This requires an electronic co-adder, which constantly reads the array at a rate of 3  $\mu\text{sec}$  per pixel (originally 4  $\mu\text{sec}$  per pixel). To read the entire array requires 5.4 msec (originally 7.2 msec).

To remove the background radiation from astronomical observations, the co-adder electronics control the secondary mirror on the telescope to chop it so that the astronomical source moves in and out of the beam. The electronic co-adder sums data in the two secondary mirror positions in different memory locations and can calculate the difference so that the background can be subtracted in real time. Typically, the co-adder would read the array 58 times per chop position for up to 8 chop cycles, and then transfer the difference of the sums in each chop position to a controlling computer, originally a PDP-11 from Digital Equipment Corporation.

### 3. FIRST OBSERVATIONS AT WIRO

The early observations made by GLADYS were of limited value because of the data acquisition software being used at that time. The software did not provide for a real-time display, which meant that actually getting the beam from an astronomical source to fall on the narrow (3.3 arcsec) slit and centering it ("peaking up") could prove very time consuming. Without a real-time display, observers were forced to look at print-outs to determine if they had the source in the beam or not. Even when a source had finally been centered in the slit, it would slowly drift out again, due to imperfect telescope tracking. The source would then have to be centered once more.

The first observing run for GLADYS at WIRO occurred 1986 October 13-20. Software at this time was still rudimentary, and the observations succeeded only in detecting  $\alpha$  Orionis. The next run, 1987 February 5-11, was more productive. The software was now reading the full array, and spectra were taken of IRC+10216, the brightest object beyond the Solar System in the 10  $\mu\text{m}$  sky. The next run, 1987 April 14-20, proved even more successful; spectra were taken of  $\alpha$  Ori,  $\mu$  Cep, and NML Cyg.



Now that observing procedures with GLADYS had been worked out, observing was growing efficient enough to make another major limitation to the original data-acquisition software apparent: it did not co-add. Instead, each frame read from the electronic co-adder was saved on disk. These transfers typically occurred once every two seconds while integrating, and each transfer took up at least 14.4 kbytes of disk space. It did not take too many clear nights to completely fill the hard disk space available.

Nonetheless, GLADYS was used at Wyoming in its basic configuration for three more observing runs. One improvement was made: the original BaF<sub>1</sub> dewar window was replaced with ZnSe, which had better long-wavelength transmission properties. These runs were 1987 October 11-17, 1988 March 9-14, and 1988 May 30 — June 6. Spectra of several bright infrared sources were obtained; these results are described in a series of abstracts, conference proceedings, and articles (LeVan and Tandy 1987; LeVan and Sloan 1987; LeVan, Tandy, and Hayward 1988; LeVan, Tandy, and Sloan 1988). The first refereed articles from these data were published by LeVan and Sloan (1989, Appendix A), and LeVan (1990, Appendix B).

The method of wavelength calibration was settled at this time and has remained unchanged since. To obtain a wavelength calibration, a piece of polystyrene is inserted into the beam while a bright astronomical source is being observed. The polystyrene absorption spectrum is isolated by dividing the resultant spectrum by a spectrum of the same astronomical source taken with nothing in the beam. Matching the absorption features in the spectrum with their known wavelengths allows a polynomial wavelength fit to the dispersion on the GLADYS array to be obtained.

#### 4. IMPROVEMENTS TO THE SYSTEM

After the summer 1988 observing run, the decision was made to overhaul the data-acquisition system for GLADYS. Plans were in place at the time to replace the computer used to point and track the telescope, also a PDP-11, with a Masscomp-5500. This new computer was fast enough to assume the responsibilities for data acquisition as well.

The new data acquisition system involved a number of improvements, including a real-time color image display and the ability to co-add up to 40 frames of data from the electronic co-adder before writing them to disk. In addition, data were saved in FITS format, a standard format for the storage and transmission of astronomical data (FITS stands for Flexible Image Transport System; Wells, Greisen and Harten 1981). These data images were stored as 58 x 62 x 2 matrices; the third dimension allowed both the mean and the uncertainty in the mean for each pixel to be written to disk.

The software was developed in the spring of 1989 and in June, was integrated with GLADYS. As it turned out, the data acquisition software was ready before the telescope tracking software for the new computer, and for the next few observing runs, the Masscomp ran GLADYS, while the old Forth-based system on the PDP-11 ran the telescope.

The new data acquisition system was tested at the telescope for the first time 1989 July 25-27. Some bugs were found in the software and repaired, but in all the run was quite successful. Prior to the run, the original spectrometer slit had been replaced with a narrower, 2 arcsecond slit to improve the spectroscopic resolution of the instrument.

During the fall of 1989, the original array, which had been obtained on loan, was replaced with a more sensitive array. Because of concerns that the increased sensitivity might saturate the pixels, the integration time per pixel was shortened by reading only 10 rows out of the 29 in each half of the array. Some notable improvements were made to the system at the same time, including re-aligning the prism to shift the effective wavelength coverage of the array to 7-14  $\mu\text{m}$ , and adding a cold snout below the dewar window to limit stray off-axis radiation falling on the detector. These modifications and their effects on the system are described by LeVan (1991). The limiting magnitude of the system at this time was about 1.1 (this is defined to be the magnitude of a source for which a spectrum with a signal/noise of 3 per pixel could be obtained in a 30 minute integration). Subsequent tests showed that the instrument was not background-limited. Some system noise, probably read noise, dominated the counting noise from the background.

Observations were first made with the new array 1989 December 17-21, but this run was marred by poor weather. The next observing runs, 1990 March 3-9 and 1990 April 14-19, were also impaired by poor observing conditions. The latter run was notable in that students at WIRO were now using the instrument on their own, with no supervision from astronomers at AFGL. This was a major step toward GLADYS becoming an observatory instrument at WIRO. By this time, the data acquisition software had been improved by adding a video mode to monitor the array output without writing data to disk, saving substantial disk space by throwing away observations made while focusing or peaking up on a source.

Another substantial step during the spring 1990 runs was the implementation of a three-beam chop, as described by Landau, Grasdalen, and Sloan (1992). Previously, background subtraction had been performed by a chop-and-nod sequence. The chopping scheme described in Section 2 does not account for any gradients in either telescope or sky emission, so periodically, the entire telescope is shifted to move the astronomical source into the opposite beam. If we refer to the first telescope position as position A, and the second as position B, the nod sequence A-B-B-A will remove all linear spatial gradients in the sky emission, as well as linear gradients in emission over time. Most importantly, any spatial gradients in the telescope emission, whether linear or not, will be canceled out in this scheme. In the new three-beam chop, the telescope never moves. Instead, the off-source chops are alternated, first to one side of the astronomical source, then the other, then back to the first. The paper by Landau et al. shows that at WIRO, as long as the chopping angle is small (less than 40 arcsec or so), the telescope emission is nearly linear and completely removed in this scheme. The three-beam chop provides much better spatial stability, as the telescope is never moved. Because most extended sources studied by GLADYS are extended only on the order of an arcsec or so, this spatial stability is critical.

The next observing run, 1990 June 22-24, suffered from uncooperative weather. The following observing runs, 1990 July 7-11 and 1990 September 2-4, were more successful. During the period 1989-90, three separate scientific programs were pursued: a study of carbon stars associated with oxygen-rich dust, a study of sources showing a 13  $\mu$ m bump on the broad 10  $\mu$ m silicate emission feature, and the monitoring of the spectra of long-period variables. Preliminary results for these programs were presented by LeVan, Sloan, and Grasdalen (1990), LeVan and Tandy (1990, Appendix C), and LeVan, Sloan, and Grasdalen (1991) respectively.

Wyoming astronomers using GLADYS data found a serious problem with the data at this time. For reasons which have remained mysterious, the electronic co-adder frequently failed, producing glitches in the data. These glitches characteristically reduced the co-adder output from the correct value by roughly 5-10 percent, although occasionally the error was substantially larger. The problem was difficult to detect prior to flat-fielding the data.

To flat-field the data (that is, to correct for the variations in the assumed linear responsivities from one pixel to the next) observations of foam impregnated with liquid nitrogen are made. As the nitrogen evaporates, the foam warms up. By taking a difference between an image of warm foam and an image of cold foam, the y-intercepts of the response functions of each pixel are canceled out and one is left with the slopes of the response function, which are the sensitivities of the pixels. These flat-fields are not true flat-fields, since the transmission of the dewar optics and the sensitivities of the detectors are both functions of wavelength, and the actual spectrum of the foam itself is also present in the images, but when one obtains a calibrated spectrum by dividing a program spectrum by the spectrum of a standard star, this spectral information is divided out.

The method used at AFGL was different from that just described, in that attempts were made to remove the wavelength information in the flat-fields themselves, instead of just dividing it out when the near-final spectra were calibrated. For this reason, the co-adder errors went unnoticed at AFGL. Soon, though, it had become painfully obvious that the co-adder was in some way degrading the quality of the data. Observations made on the night of 1990 October 5 clinched the issue when co-added observations of Jupiter were compared to single-frame observations of Mars. After flat-fielding, the Mars observations were beautifully smooth, while the Jupiter data still appeared noisy (see Appendix E, Figure 1-4).

Through November and December, 1990 students and staff at Wyoming, as well as Dr. LeVan at AFGL, conducted a series of tests to determine the source of the co-adder errors. While the problem was isolated and characterized, its

source was never found. The problem was *eliminated*, however, when the wire-wrapped counter boards in the electronic co-adder were replaced with printed circuit boards. The weather remained poor, and only one set of observations of Mars on 1990 December 16 was possible. The next observing run, in mid-January, 1991 was completely clouded out.

## 5. CULMINATION OF THE PROJECT

The corrections to the electronic co-adder could not be thoroughly tested until the next run, 1991 February 6-12. On this run, GLADYS performed almost flawlessly, and the weather was excellent. Over 60 Mbytes of data were taken on a wide variety of sources. Several publications and a Ph.D. dissertation have resulted from data taken on this run. Much of the data remains untouched; more publications from this one run will undoubtedly follow.

The study of carbon stars with silicate dust emission was brought to fruition by LeVan et al. (1992, Appendix F). They confirmed that two carbon stars, BM Gem and V778 Cyg were both sources of silicate emission, discovered similar emission in another source, HD 189605, and showed that an additional suspected source of silicate dust, HD 100764, possessed only a continuum-like spectrum at 10  $\mu\text{m}$ .

The quality of the observations from the 1991 February run led to some new procedures for the reduction of long-slit spectroscopic data. By fitting a suitable spatial profile to a spectroscopic image at each wavelength, a plot of the apparent angular extent of an object as a function of wavelength can be obtained. Such a plot is known as a spatio-gram. By comparing spatio-grams of  $\alpha$  Orionis and HD 44179 (the Red Rectangle) with those of a point source standard, Grasdalen, Sloan, and LeVan (1992, hereafter Appendix D) showed that GLADYS had resolved dust emission in the vicinity of both these objects.

A more powerful reduction tool for long-slit spectroscopic images is maximum entropy reconstruction. Modifying existing reconstruction techniques for spectroscopic data and applying them to observations of  $\alpha$  Ori and HD 44179 formed the basis of Dr. Sloan's Ph.D. dissertation (Sloan 1992). Preliminary results were presented by Sloan, Grasdalen, and LeVan (1991). Individual chapters from this dissertation have been published in the literature (Appendix D; Sloan, Grasdalen, and LeVan 1993a, 1993b, Appendices G and H respectively), or are in preparation for publication (Sloan and Grasdalen 1993, Appendix I).

Additional observing runs that followed have proven less successful. The next run, 1991 April 20-23, was mostly clouded out, while data from the following run, 1991 June 3-8, indicated that the electronic co-adder had begun to fail once more. Attempts to repair the co-adder during the 1991 August 25-29 run did not succeed. A subsequent look at the data revealed that the co-adder failure was very similar to that before the repairs made in the fall of 1990. As a result, GLADYS was retired from service until the problem could be eliminated once and for all.

## 6. THE NEW ELECTRONICS

In the spring of 1992, the decision was made at the Geophysics Directorate of the Phillips Laboratory (the former Air Force Geophysics Lab) to replace the existing co-adder with electronics produced by Wallace Instruments. The replacement is extensive; not only are the co-adder electronics new, but the analog-digital conversion circuitry and the clocking circuitry as well. In short, everything outside the dewar has been replaced.

During the summer of 1992, Dr. LeVan worked with Peter Tandy and Bruce Pirger to integrate the new electronics with the array multiplexer and a new data acquisition system running on a 386 machine. Dr. LeVan has left the Geophysics Directorate of Phillips Lab, and Pirger's summer appointment has ended, but Dr. Sloan has worked with Mr. Tandy, as well as Dr. Gary Grasdalen and James Weger from WIRO to continue the integration of the new system with GLADYS.

Initial tests have proven very successful. The new system noise is estimated at a noise equivalent flux density of  $10 \text{ Jy Hz}^{-1/2}$ , better than the old system by roughly a factor of 10, but still not background-limited. There are no indications of co-adder errors similar to those seen in the previous system. Plans are to take the new system back to Wyoming for observations beginning in the late winter of 1993. With the experience gained developing data acquisition techniques and data reduction procedures with GLADYS in its earlier configurations, the future of GLADYS looks promising.

When first ready for observational use, GLADYS represented a unique instrument; it was the only long-slit spectrometer designed for astronomical observations at  $10 \mu\text{m}$ . While there are now other long-slit  $10 \mu\text{m}$  spectrometers in use, GLADYS is still a potent instrument. There is great deal of astronomy still to be done with it.

## References

1. Grasdalén, G.L., Sloan, G.C., and LeVan, P.D. (1992) Spatial Structure in the 10 Micron Spectrum of HD 44179 (the Red Rectangle), *ApJ*, **384**, L25. (Appendix D)
2. Landau, R., Grasdalén, G.L., and Sloan, G.C. (1992) Three-beam Chopping: an Efficient Infrared Observing Technique, *A&A*, **259**, 696.
3. LeVan, P.D., (1990) Capabilities of the AFGL Mosaic Array Spectrometer — Ten-micron Spectra of Bright Infrared Stars, *PASP*, **102**, 190. (Appendix B)
4. LeVan, P.D., (1991) 7.5 to 13.5  $\mu$ m Spectral Imaging with an Array Spectrometer, in *Proceedings of the 1991 North American Workshop on Infrared Astronomy*, ed. R.E. Stencel (Boulder, CO: University of Colorado), p. 23.
5. LeVan, P.D., and Sloan, G. (1987) Calibration and Data Reduction Techniques for the AFGL Astronomical Infrared Array Spectrometer, *SPIE*, **819**, 204.
6. LeVan, P.D., and Sloan, G. (1989) Ten-micron Observations of Bright Circumstellar Shells — Spectral Properties and a Search for Extended Emission, *PASP*, **101**, 1140. (Appendix A)
7. LeVan, P.D., Sloan, G., and Grasdalén, G.L., (1990) Confirmation of Silicate Feature Emission in the Carbon Star BM Geminorum, *BAAS*, **22**, 817.
8. LeVan, P.D., Sloan, G., and Grasdalén, G.L., (1991) Eight to 14  $\mu$ m Spectral Monitoring of Long Period Variable Stars with GLADYS, in *Astrophysics with Infrared Arrays*, ed. R. Elston, *ASP Conf. Ser.*, **14**, 130.
9. LeVan, P.D., Sloan, G.C., Little-Marenin, I.R., and Grasdalén, G.L. (1992) 8 -14 Micron Spectroscopy of Carbon Stars Associated with Silicate Dust, *ApJ*, **392**, 702. (Appendix F)
10. LeVan, P.D., and Tandy, P.C. (1987) Recent Astronomical Results Obtained with the AFGL Ten Micron Array Spectrometer, in *Infrared Astronomy with Arrays*, ed. C. Wynn-Williams and E.E. Becklin (Hilo, HI: University of Hawaii), p. 411
11. LeVan, P.D., and Tandy, P.C. (1990) Confirmation of Emission Features near 13  $\mu$ m in Spectra of RX Bootis and S Draconis, *BAAS*, **22**, 1266. (Appendix C)
12. LeVan, P.D., Tandy, P.C., and Hayward, T. (1988) AFGL Mosaic Array Spectrometer — Measurements of Circumstellar Shells, *BAAS*, **20**, 724.
13. LeVan, P.D., Tandy, P.C., and Sloan, G. (1988) AFGL Mosaic Array Spectrometer — Further Measurements of Circumstellar Shells, *BAAS*, **20**, 1104.

14. Sloan, G.C. (1992) *Spatially Resolved 10 Micron Spectra of Circumstellar Material around Evolved Stars*, Ph.D. Dissertation (Laramie, WY: University of Wyoming). (Chapter I: Appendix E)
15. Sloan, G.C., and Grasdalen, G.L. (1993) Maximum Entropy Reconstruction Techniques for Long-slit Spectroscopy, in preparation. (Appendix I)
16. Sloan, G.C., Grasdalen, G.L., and LeVan, P.D. (1991) *The Dust Shell around  $\alpha$  Orionis*, *BAAS*, **23**, 1386.
17. Sloan, G.C., Grasdalen, G.L., and LeVan, P.D. (1993a) *Spatially Resolved Spectra of Silicate Dust around  $\alpha$  Orionis*, *ApJ*, **404**, 328. (Appendix G)
18. Sloan, G.C., Grasdalen, G.L., and LeVan, P.D. (1993b) *Spatially Resolved Spectra of the Unidentified Infrared Features around HD 44179 (The Red Rectangle)*, *ApJ*, **409**, 412. (Appendix H)
19. Wells, D.C., Greisen, E.W., and Harten, R.H. (1981) *A&A Suppl*, **44**, 363.

## Chronological Bibliography of GLADYS Publications

1. LeVan, P.D., and Tandy, P.C. (1987) Recent Astronomical Results Obtained with the AFGL Ten Micron Array Spectrometer, in *Infrared Astronomy with Arrays*, ed. C. Wynn-Williams and E.E. Becklin (Hilo, HI: University of Hawaii), p.411.
2. LeVan, P.D., and Sloan, G. (1987) Calibration and Data Reduction Techniques for the AFGL Astronomical Infrared Array Spectrometer, *SPIE*, **819**, 204.
3. LeVan, P.D., Tandy, P.C., and Hayward, T. (1988) AFGL Mosaic Array Spectrometer — Measurements of Circumstellar Shells, *BAAS*, **20**, 724.
4. LeVan, P.D., Tandy, P.C., and Sloan, G. (1988) AFGL Mosaic Array Spectrometer — Further Measurements of Circumstellar Shells, *BAAS*, **20**, 1104.
5. LeVan, P.D., and Sloan, G. (1989) Ten-micron Observations of Bright Circumstellar Shells — Spectral Properties and a Search for Extended Emission, *PASP*, **101**, 1140.
6. LeVan, P.D. (1990) Capabilities of the AFGL Mosaic Array Spectrometer — Ten-micron Spectra of Bright Infrared Stars, *PASP*, **102**, 190.
7. LeVan, P.D., Sloan, G., and Grasdalen, G.L. (1990) Confirmation of Silicate Feature Emission in the Carbon Star BM Geminorum, *BAAS*, **22**, 817.
8. LeVan, P.D., and Tandy, P.C. (1990) Confirmation of Emission Features near 13  $\mu$ m in Spectra of RX Bootis and S Draconis, *BAAS*, **22**, 1266.
9. LeVan, P.D. (1991) 7.5 to 13.5  $\mu$ m Spectral Imaging with an Array Spectrometer, in *Proceedings of the 1991 North American Workshop on Infrared Astronomy*, ed. R.E. Stencel (Boulder, CO: University of Colorado), p. 23.
10. LeVan, P.D., Sloan, G., and Grasdalen, G.L. (1991) Eight to 14  $\mu$ m Spectral Monitoring of Long Period Variable Stars with GLADYS, in *Astrophysics with Infrared Arrays*, ed. R. Elston, *ASP Conf. Ser.*, **14**, 130.
11. Sloan, G.C., Grasdalen, G.L., and LeVan, P.D. (1991) The Dust Shell around  $\alpha$  Orionis, *BAAS*, **23**, 1386.
12. Grasdalen, G.L., Sloan, G.C., and LeVan, P.D. (1992) Spatial Structure in the 10 Micron Spectrum of HD 44179 (the Red Rectangle), *ApJ*, **384**, L25.
13. Sloan, G.C. (1992) *Spatially Resolved 10 Micron Spectra of Circumstellar Material around Evolved Stars*, Ph.D. Dissertation (Laramie, WY: University of Wyoming).
14. LeVan, P.D., Sloan, G.C., Little-Marenin, I.R., and Grasdalen, G.L. (1992) 8-14 Micron Spectroscopy of Carbon Stars Associated with Silicate Dust, *ApJ*, **392**, 702.

15. Landau, R., Grasdalen, G.L., and Sloan, G.C. (1992) Three-beam Chopping: an Efficient Infrared Observing Technique, *A&A*, 259, 696.
16. Sloan, G.C., Grasdalen, G.L., and LeVan, P.D. (1993a) Spatially Resolved Spectra of Silicate Dust around  $\alpha$  Orionis, *ApJ*, 404, 328.
17. Sloan, G.C., Grasdalen, G.L., and LeVan, P.D. (1993b) Spatially Resolved Spectra of the Unidentified Infrared Features around HD 44179 (The Red Rectangle), *ApJ*, 409, 412.
18. Sloan, G.C., and Grasdalen, G.L. (1993) Maximum Entropy Reconstruction Techniques for Long-slit Spectroscopy, in preparation.



## **Appendix A**

**Ten-Micron Observations of Bright Circumstellar Shells—Spectral Properties and a Search  
for Extended Emission**

## TEN-MICRON OBSERVATIONS OF BRIGHT CIRCUMSTELLAR SHELLS— SPECTRAL PROPERTIES AND A SEARCH FOR EXTENDED EMISSION\*

PAUL D. LEVAN

Air Force Geophysics Laboratory, Hanscom Air Force Base, Massachusetts 01731

AND

GREGORY SLOAN

Physics and Astronomy Department, University of Wyoming, Laramie, Wyoming 82071

Received 1989 March 13, revised 1989 August 22

### ABSTRACT

We have obtained 9–14  $\mu\text{m}$  spectra for several bright long-period variable stars, using novel instrumentation comprising a mosaic detector array and a prism slit spectrometer. Three of the stars are carbon rich and have SiC feature emission. The remaining five are oxygen rich; three exhibit pronounced silicate emission. We find agreement in the SiC equivalent widths for the three carbon stars observed here and during the 1983 flight of the IRAS low-resolution spectrometer. Two stars with silicate feature emission observed at both epochs, IRC +10420 and  $\mu$  Cep, show pronounced variation in the equivalent widths of these features. We observe continuum variations exceeding the photometric levels of uncertainty for either instrument for the carbon star V Cyg which correlate well with visible light curves. None of the circumstellar shells of these stars were fully resolved; only IRC +10420 may be partially resolved. We find that our observed upper limits on surface brightness of dust associated with molecular outflows from IRC +10216 are compatible with calculated lower limits, yielding no additional constraints on the depressed dust emission suggested by far-infrared detections of the outflow material.

**Key words:** infrared spectroscopy—circumstellar shells—infrared sources

### 1. Introduction

In this paper we examine the spectral and spatial properties of several bright post-main-sequence stars using the AFGL 10- $\mu\text{m}$  mosaic array spectrometer (hereafter called GLADYS). These include the carbon-rich stars IRC +10216 (CW Leonis), CIT 6 (IRC +30219 or RW Leonis Minoris), and V Cygni, as well as the oxygen-rich stars  $\alpha$  Bootis, RX Bootis, NML Cygni (V1489 Cygni), IRC +10420 (V1302 Aquilae), and  $\mu$  Cephei.

Many stars with large infrared excesses have been identified as long-period variables and are known to have continuum fluxes which vary on a time scale of years. Narrow-band photometry indicates that the flux contained in the 9.7- $\mu\text{m}$  silicate and the 11.5- $\mu\text{m}$  silicon carbide features varies in phase with the continuum (Forrest, Gillett, and Stein 1975).

Unfortunately, little is known about the relative variation of feature and continuum fluxes at higher spectral resolution. In order to examine possible variations between a separate observational epoch and our own, we compare our spectra with those taken by the Low-Resolu-

tion Spectrometer (LRS) on IRAS and published in the Atlas of Low Resolution IRAS Spectra (Olson and Raimond 1986, LRS Atlas hereafter).

Several of the brighter stars with pronounced circumstellar emission reported here are at the threshold of seeing-limited resolution. Stellar occultation measurements (Toombs *et al.* 1972) demonstrated that the bright carbon star IRC +10216 is extended on the scale of arc seconds at 10  $\mu\text{m}$ . Details of the structure of the assumed disk geometry for this object as a function of wavelength were in turn provided by the application of speckle imaging (McCarthy, Howell, and Low 1980; Mariotti *et al.* 1983; Dyck *et al.* 1984, 1987) and direct imaging (Bloemhof *et al.* 1988). The speckle results of Dyck *et al.* (1987) and Benson, Turner, and Dyck (1989) are consistent with a transition of the extended emission of IRC +10216 from oval-shaped to circular geometry between wavelengths of 5 and 10  $\mu\text{m}$ , supporting earlier results based on Fourier plane imaging (Sutton *et al.* 1979). Examples of oxygen-rich circumstellar envelopes resolved by speckle interferometry include IRC +10420 and NML Cyg (Fix and Cobb 1988). We examine the spatial nature of these stars with our mosaic array in an attempt to constrain the

\*Contribution 115 of the Wyoming Infrared Observatory.

nature and geometry of the mass loss from these stars.

## 2. Observations and Data Reduction

### 2.1 Observations

We observed the program objects listed in Table 1 with GLADYS at the 2.3-m telescope at the Wyoming Infrared Observatory. The spectrometer consists of a  $58 \times 62$  Si:Ga detector array hybridized with a direct-readout multiplexer. The NaCl prism disperses radiation from 9 to  $14 \mu\text{m}$  along the 62-pixel axis, while the slit lies along the 58-pixel axis. The array is scanned continuously at a frequency of 185 Hz. The output is digitized to 12-bit accuracy and electronically coadded over a 2-sec interval. The secondary mirror was chopped at a frequency of roughly 3 Hz and an amplitude of 25 arc seconds along the north-south slit axis, resulting in seven plus and minus chop differences for each 2-sec frame. We define an exposure in Table 1 as a total of 80 output frames, taken in groups of 20 while nodding between two positions in the sky. This scheme corrects variations in the sky emission to first order.

With the exception of IRC +10216 all stars were centered near one-quarter of the slit length from the top of the array. We centered IRC +10216 at four different slit positions separated by  $2''$  increments to evaluate the flat-field properties of the array.

### 2.2 Reduction of Spectral Data

Although each row exposed to the image of a star has its associated spectrum, we do not examine each separately. The strongest spectra off the central row have a signal-to-noise ratio two times weaker than the peak spectrum (as quantified by the spatial scans shown in Fig. 4). We choose to sum the rows into one spectrum for each exposure. These summed spectra are displayed for each source in Figure 1 and represent the best exposure taken from all those listed in Table 1. These reductions and displays were accomplished using IRAF<sup>1</sup>.

The error bars displayed in Figure 1 show the uncertainties in the mean of the 80 frames which make up each exposure, but they do not represent the uncertainty of the correction for atmospheric absorption or instrumental response. These are quantified by the deviations of the measured points from the assumed blackbody distribution superposed on the spectrum of  $\alpha$  Boo (Fig. 1a). The remaining stars observed on the same night as  $\alpha$  Boo (RX Boo, IRC +10420, and V Cyg) are corrected for atmospheric absorption and instrumental response to an accuracy approaching that of  $\alpha$  Boo.

Our error bars also do not relate to absolute flux levels. The slit spectrometer does not allow absolute spectropho-

TABLE 1  
Observing Log

Star	Date (UT)	Exposures <sup>a</sup>	Notes
IRC +10216	12 Mar 1988	4	b, c
CIT 6	12 Mar 1988	3	c
$\alpha$ Boo	12 Mar 1988	5	c
$\alpha$ Boo	4 Jun 1988	5	d
RX Boo	4 Jun 1988	4	d
IRC +10420	4 Jun 1988	4	d
V Cyg	4 Jun 1988	4	d
RX Boo	5 Jun 1988	4	b, e
NML Cyg	5 Jun 1988	3	e
$\mu$ Cep	5 Jun 1988	3	e

#### Notes:

<sup>a</sup>Exposures are defined as two beamswitch pairs (i.e. 80 frame transfers or 400 chop pairs).

<sup>b</sup>Only one beamswitch pair (40 frames) per exposure.

<sup>c</sup>12 Mar 1988 exposures have 31 of 62 spectral elements and full background digitization (12 bits).

<sup>d</sup>4 Jun 1988 exposures have all 62 spectral elements and 11 bit background digitization.

<sup>e</sup>5 Jun 1988 exposures have all 62 spectral elements and full background digitization.

tometry because the point-spread-function (PSF) width varies with the seeing and can be truncated by the narrow slit. We estimate the uncertainty of our absolute levels, based on the repeatability of flux levels from exposure to exposure, to be better than 25% for the present observations.

### 2.3 Reduction of Spatial Data

We analyze the spatial nature of the stars by examining angular scans at seven or ten specific wavelength elements on the array, spaced evenly between 10 and  $11.4 \mu\text{m}$ . We used ten elements for observations made in June but were limited to seven elements for the March observations because of a breakdown in one of the two wavelength-interlaced output channels (see Table 1). This resulted in coarser spectral sampling for IRC +10216 and CIT 6. We fit a Gaussian profile to each of these spatial cuts, obtaining values for the Gaussian  $\sigma$ , a peak amplitude, and a peak center  $x_0$ . We then normalized each of these spatial cuts and averaged them together to form a composite profile. Each cut is 21 pixels across, but we chose to average the five outer pixels at the northern and southern extremes to obtain a higher signal-to-noise ratio for these endpoints. The resulting spatial scans are  $13.75$  across.

Two of the three Gaussian parameters are correlated with  $\lambda$ :  $\sigma$  and  $x_0$ . The relation between  $x_0$  and  $\lambda$  is discussed in LeVan (1990); it results from a rotational misalignment between the array and the prism dispersion axis. The monotonic increase of the Gaussian  $\sigma$  with increasing  $\lambda$  is characterized by a 0.1 exponent power-law dependence on wavelength, much too shallow to be due

<sup>1</sup>IRAF is distributed by National Optical Astronomy Observatories, which is operated by the Association of Universities for Research in Astronomy, Inc., under contract with the National Science Foundation.

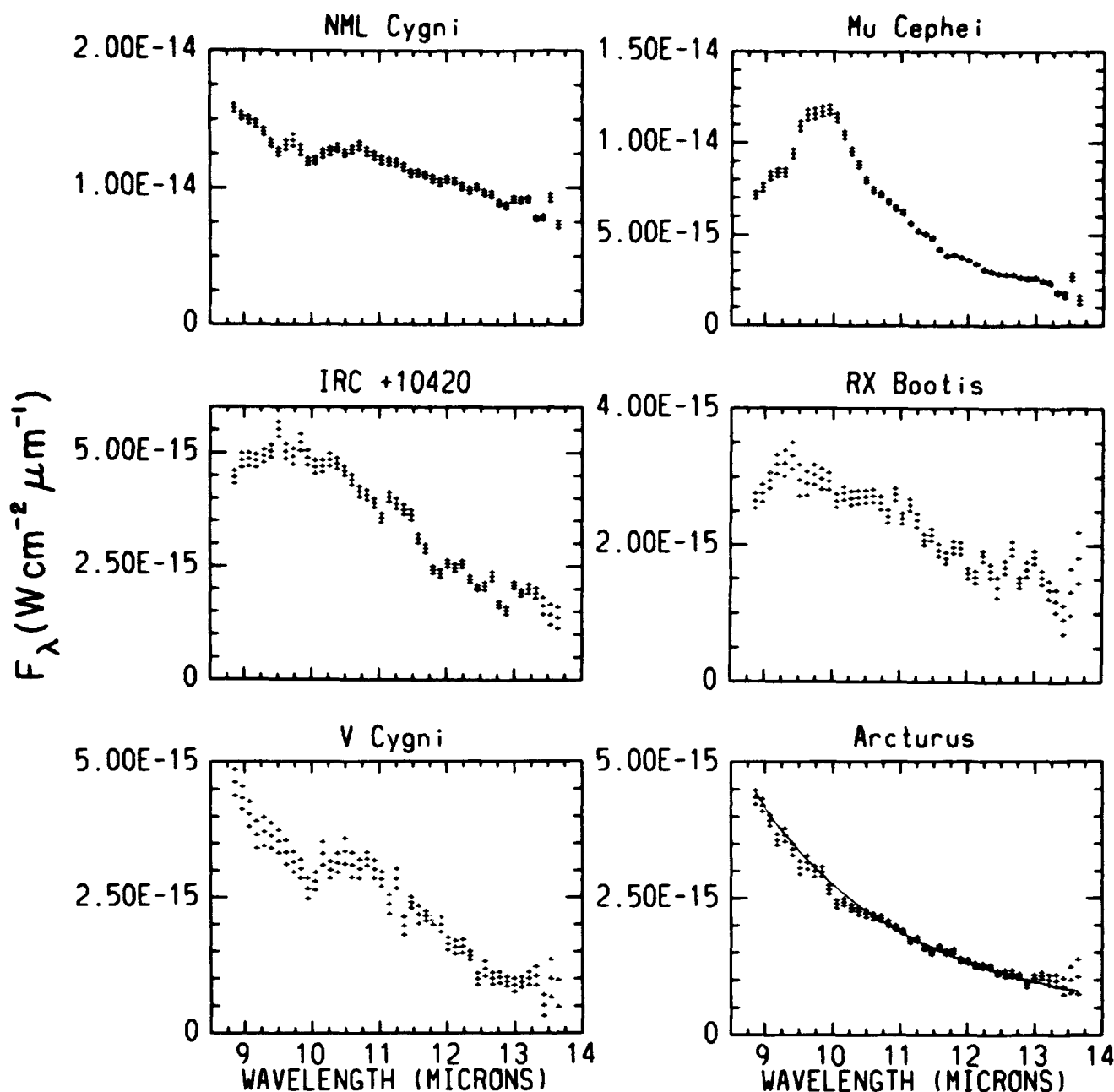


FIG. 1a—Mosaic spectrometer (GLADYS) spectra summed over the angular extent of the instrumental response. A blackbody fit to the photospheric continuum of  $\alpha$  Boo is shown to establish the accuracy of the correction for atmospheric absorption.

only to diffraction. Diffraction from the telescope primary mirror and from the collimated spectrometer beam each have an approximate 0.4 arc second Gaussian  $\sigma$  near  $10 \mu\text{m}$ .

### 3. Results

#### 3.1 Spectral Properties

The LRS Atlas provides spectra at an epoch approximately five years earlier than the GLADYS spectra discussed here. We use the LRS data as a basis of comparison for long-period variability by directly comparing equivalent

widths for the silicon carbide and silicate emission features, as this measure is independent of absolute photometric levels. Further, this measure provides insight into the *relative* variation of feature and continuum fluxes and has been neglected in previous observational work.

Also, the large number of spectra published in the LRS Atlas have provoked an interest in the nature and shape of the  $9.7 \mu\text{m}$  silicate and  $11.5 \mu\text{m}$  silicon carbide features, as quantified by their central wavelength and width. We used a method similar to that of Little-Marenin (1986) to

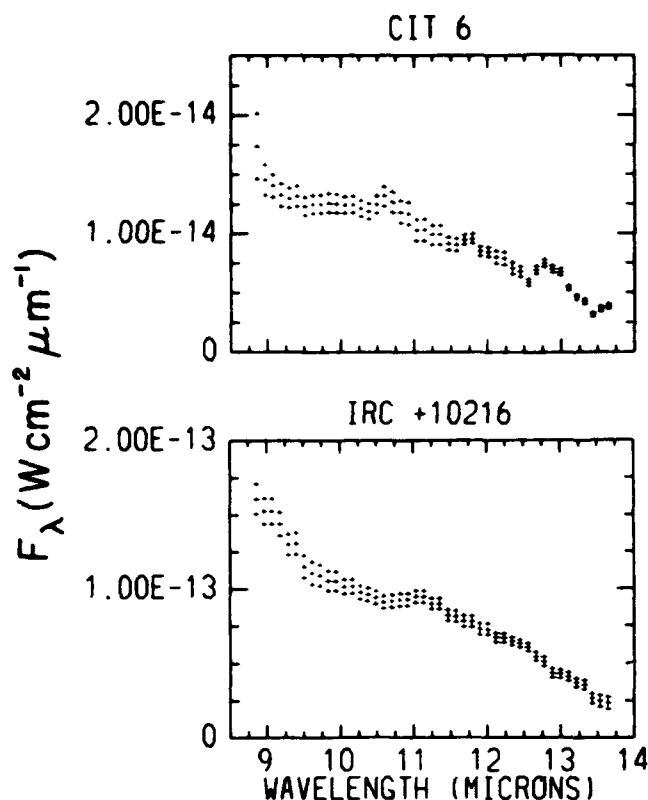


FIG. 1b—As for Figure 1a but for stars observed in March 1988. Only one of the two wavelength-interlaced output channels was then in operation. The missing wavelength elements were interpolated resulting in identical spectral sampling at reduced spectral resolution.

extract the features from both the LRS and GLADYS spectra. We first fit the continuum with the blackbody spectrum that matches the short- and long-wavelength portions of our spectra and then extract the features by subtracting out the continuum fit.

Figures 2 and 3 contain the resulting spectra for GLADYS and those found in the LRS Atlas, respectively, showing both the adopted continuum fit and extracted features. The LRS Atlas omits two of the objects observed, RX Boo and NML Cyg.

Table 2 gives our determinations of the equivalent widths ( $W_\lambda$ ) of the silicate and SiC features for both the GLADYS and LRS data. Because of the simplicity of the model we have applied to extract these features, the equivalent widths quoted should be used only for comparing the GLADYS and LRS spectra here. We have applied a correction of never more than 10% to the silicate feature flux to allow for the extension of this feature beyond the short-wavelength limit of our spectrometer.

The uncertainties in the values of equivalent width listed in Table 2 result from contributions of both the standard deviations of the observed data and the uncertainties in the prescribed continuum. For the silicate stars, the 9- $\mu$ m continuum level is set to give a ratio of

TABLE 2  
Spectral Feature Properties

Star	$F_\lambda$ ( $\times 10^{-15}$ W cm $^{-2}$ $\mu$ m $^{-1}$ )	$W_\lambda$ ( $\mu$ m)	$\lambda_c$ ( $\mu$ m)
IRC +10216	52	$1.1 \pm 0.2$	11.5
LRS	61	$1.2 \pm 0.2$	11.6
CIT 6	8.8	$0.5 \pm 0.2$	11.0
LRS	7.0	$0.3 \pm 0.2$	11.3
IRC +10420	2.7	$2.3 \pm 0.2$	10.2
LRS	1.7	$3.2 \pm 0.2$	10.2
V Cyg	1.75	$0.9 \pm 0.2$	11.1
LRS	1.05	$0.9 \pm 0.2$	11.2
$\mu$ Cep	4.2	$3.0 \pm 0.2$	10.0
LRS	2.9	$2.0 \pm 0.2$	10.0
RX Boo	2.2	$0.8 \pm 0.2$	10.1
LRS	...	...	...

feature and continuum flux at that specific wavelength as close as possible to the LRS continuum fit. This aspect of our fitting feature causes us to underestimate any actual variation in the equivalent width. In Table 2 we also give values for the central feature wavelength  $\lambda_c$ ; this value separates equal areas under the feature profile and is usually shifted to wavelengths longer than the peak emission wavelength. The continuum fluxes listed in Table 2 are for this wavelength.

For the oxygen-rich stars IRC +10420 and  $\mu$  Cep, we find the peak emission is shortward of 10  $\mu$ m in both the GLADYS and LRS spectra, as can be seen from the spectra in Figures 2 and 3 of the GLADYS and LRS extracted silicate features for both stars. This fact is consistent with Little-Marenin's determination of a central wavelength of 9.8  $\mu$ m for a large sample of LRS spectra. The LRS spectra also show signs of optical thickness in both these stars and possibly self-absorption in IRC +10420, whose LRS spectrum even exhibits very pronounced silicate emission near 18  $\mu$ m.

The spectral features of the SiC stars are weaker than those of the silicate stars and, as a result, their properties are more sensitive to the continuum fitting procedure. For IRC +10216 we find the SiC feature to have a peak wavelength of 11.3  $\mu$ m (compared with the value of 11.6  $\mu$ m found by Little-Marenin). Both our and Little-Marenin's extractions of the SiC feature in IRC +10216 result in a peak flux shifted to longer wavelengths due to the inadequacy of a blackbody continuum fit.

Data from the LRS and GLADYS epochs are insufficient to determine either the amplitude or period of the infrared variability, so we use visible data from the American Association of Variable Star Observers (AAVSO; Mattei 1988, 1989) and the Variable Star Catalogue (Kholopov *et al.* 1985, VSC hereafter), where available, to estimate

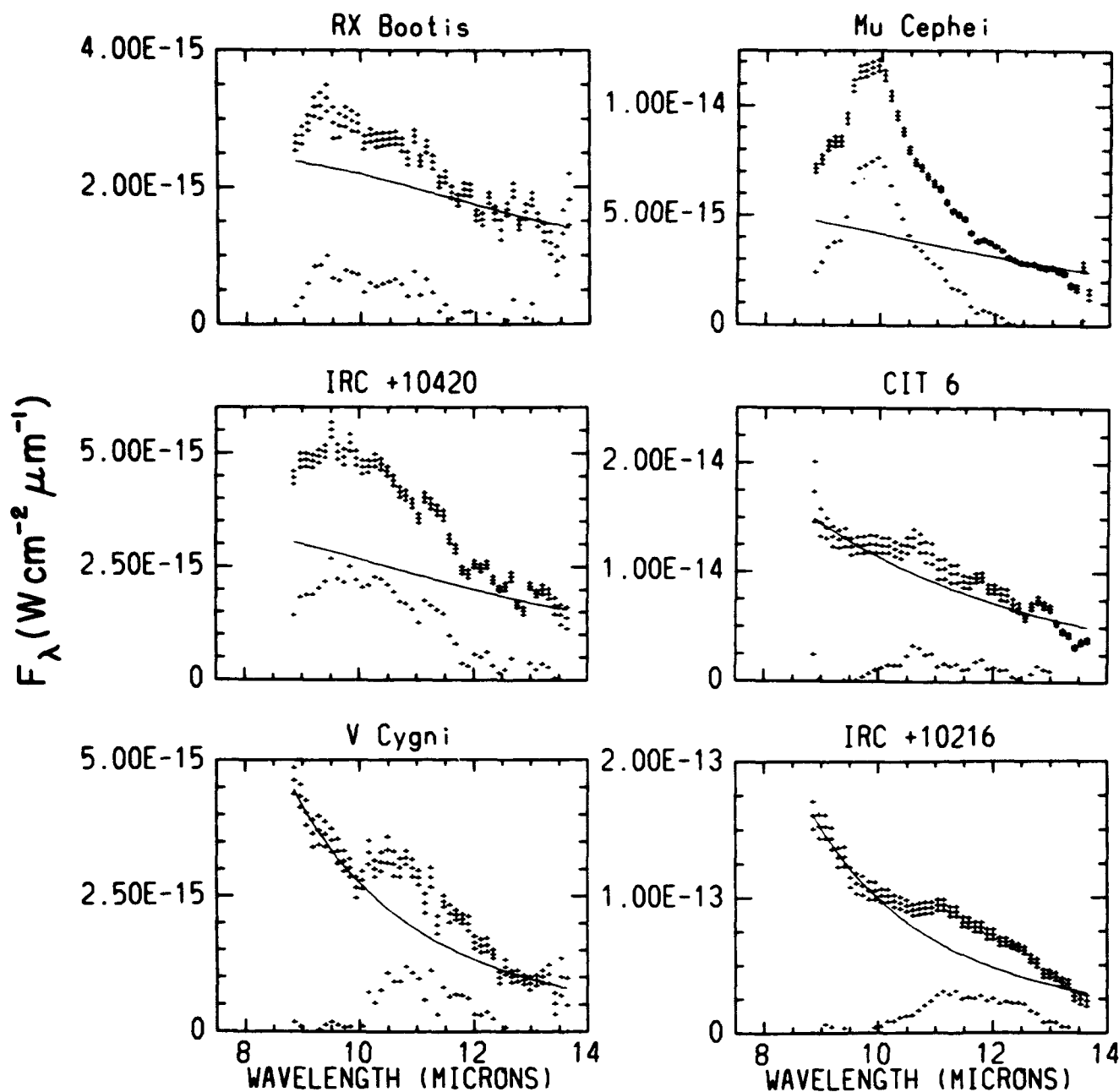


FIG. 2—Results of the fitting of the continuum and extraction of the feature emission fluxes for the six stars observed with pronounced feature emission. The silicate feature flux relative to the shortest wavelength continuum point has been estimated using methods described in the text for RX Bootis, Mu Cephei, and IRC +10420.

the phase on the infrared light curve.

V Cyg exhibits pronounced continuum variability over the two epochs that exceeds the level of uncertainty in absolute flux for either instrument. This change agrees with unpublished AAVSO data: V Cyg reached a minimum near June 1983, the midpoint of the IRAS mission, whereas the GLADYS spectrum of V Cyg was taken four months after minimum and two months before maximum.

Of the remaining two carbon stars, IRC +10216 and CIT 6, the continuum levels at both epochs are in remark-

able agreement, an observation initially surprising if one considers the approximate one-magnitude variation seen in 10- $\mu$ m narrow-band monitoring (Nye and Merrill 1980). However, the periods for these stars given in VSC are 630 days for IRC +10216 (CW Leo) and 640 days for CIT 6 (RW LMi). We therefore expect a variation in the relative phase of less than 5% between the IRAS and GLADYS epochs for both objects. We note also that Jones and Rodriguez-Espinosa (1984) observed a minimum in the 10- $\mu$ m light curve of IRC +10216 near January 1983,

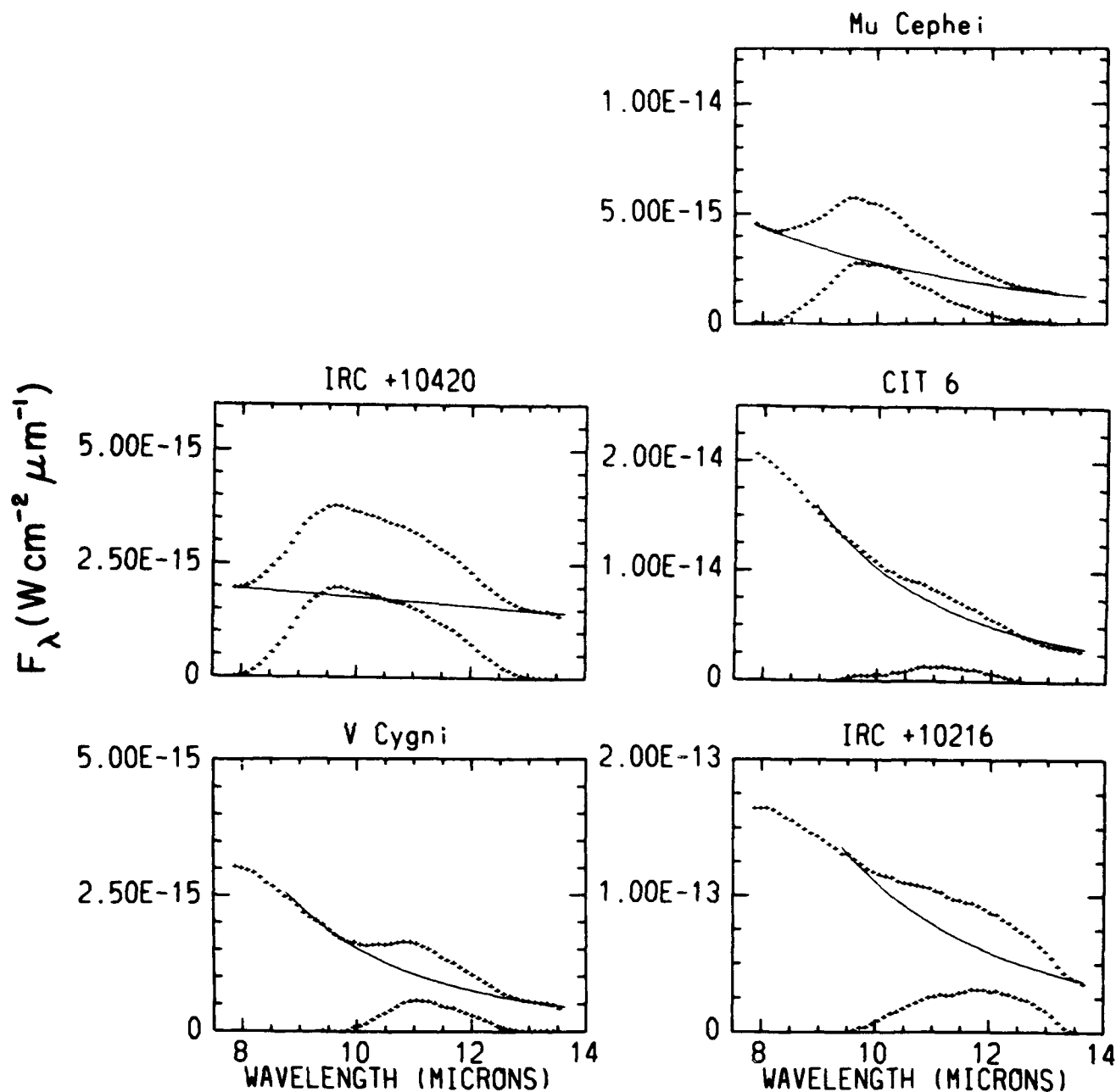


FIG. 3—Spectra from the LRS Atlas shown (where available) for the stars in Figure 2. The blackbody fit to the continuum and extracted feature fluxes are also shown. The inadequacy of the blackbody fit may easily be seen for two of the three SiC stars: IRC +10216 and CIT 6.

and Nye and Merrill found the two objects to be virtually in phase from 1973–74.

GLADYS and the LRS both observed two oxygen-rich stars with silicate features,  $\mu$  Cep and IRC +10420. According to unpublished AAVSO light curves, the LRS observed  $\mu$  Cep before maximum and GLADYS observed it after maximum. The period of  $\mu$  Cep is 730 days (VSC). The 20% difference about the mean in the infrared continuum levels at the two epochs is within the expected photometric accuracy for both instruments. IRC +10420

shows more appreciable differences between the two epochs, 45% variation about the mean in the continuum levels. Little variability is indicated by the unpublished AAVSO light curves, and the Nye and Merrill monitoring in 1973 and 1974 indicates the ratio of maximum to minimum light is roughly two in the infrared.

We address last the feature equivalent-width variations between the IRAS and GLADYS epochs. Two of the three carbon stars, IRC +10216 and V Cyg, show agreement between the two epochs well within the levels of

uncertainty, whereas differences in the equivalent widths of CIT 6 are at the level of uncertainty. However, two oxygen-rich stars, IRC +10420 and  $\mu$  Cep, show differences at statistically meaningful levels, increasing in the first case between the two epochs and decreasing in the second. We conclude that relative variations of continuum and feature fluxes may occur for at least some oxygen-rich, long-period variables.

### 3.2 Spatial Properties: Outflow Brightness Limits

Direct imaging of post-main-sequence stars has been demonstrated at the telescope diffraction limit (e.g., Bloemhof, Townes, and Vanderwyck 1984; Bloemhof *et al.* 1988). The angular resolution of our exposures is limited by atmospheric seeing over the 2-sec exposure time and diffraction within the spectrometer which adds in quadrature an amount equal to that of the telescope (LeVan 1990).

In the case of IRC +10420 the average of four exposures is characterized by a Gaussian  $\sigma$  roughly 10% larger than the sample average. We cannot rule out seeing variations, but this result may suggest a source size on the order of several tenths of an arc second in FWHM, in quantitative agreement with 10- $\mu$ m speckle interferometry values of 0.4 for the FWHM of IRC +10420 (Fix and Cobb 1988).

We now limit the discussion of spatial profiles to the wings. Our instrument is in principle sensitive to the large ranges of brightness expected for a bright source

surrounded by diminishing thermal radiation from dust at larger angular separations. Also, since all spatial (and spectral) measurements are obtained simultaneously, the relative signal strengths are affected less by transients.

Table 3 lists the scan endpoint fluxes in percent (averaged over the outer five pixels in the spatial cuts, between 5" and 9") for each exposure. The uncertainties for IRC +10216 and CIT 6 are larger than one would expect for their apparent magnitudes because of the smaller number of wavelength elements included in the scan. A close examination of Table 3 reveals significant variation from exposure to exposure for a given object, *yet reasonably good agreement for both scan endpoints of a given exposure*. Some of the endpoint values are as high as 1% of the peak flux, probably a result of scattered radiation in the instrument. The variations among the exposures and the scan width variations discussed above both probably result from the effects of changing seeing conditions on the PSF.

Recent detections of thermal radiation at far-infrared wavelengths (Fazio *et al.* 1980; Lester, Harvey, and Joy 1986, or LHJ hereafter) and scattered radiation (Tamura *et al.* 1988) from the envelope associated with molecular gas outflow (Olofsson *et al.* 1982) from IRC +10216 suggest searching for extended low-level radiation in the 10- $\mu$ m region. We may derive observational upper limits on the surface brightness of the halo of IRC +10216 at 7" from the peak using the scan endpoint data presented in Table 3, and at 3.5" from the peak using unlisted data that

TABLE 3  
10.5  $\mu$ m Scan Endpoint Fluxes (Percentage of Peak)

Star	Position	Exposure Number			
		(1)	(2)	(3)	(4)
$\alpha$ Boo	7" N	$-0.03 \pm 0.37$	$1.48 \pm 0.23$	$-0.64 \pm 0.38$	$0.68 \pm 0.29$
	7" S	$-0.57 \pm 0.41$	$0.92 \pm 0.30$	$-0.74 \pm 0.37$	$0.70 \pm 0.22$
RX Boo	7" N	$0.33 \pm 0.34$	$-0.27 \pm 0.41$	$0.77 \pm 0.48$	$0.29 \pm 0.28$
	7" S	$0.46 \pm 0.24$	$-0.74 \pm 0.42$	$0.81 \pm 0.38$	$0.39 \pm 0.28$
$\mu$ Cep	7" N	$0.32 \pm 0.04$	$0.24 \pm 0.06$	$0.21 \pm 0.09$	...
	7" S	$0.19 \pm 0.06$	$0.22 \pm 0.08$	$0.25 \pm 0.10$	...
V Cyg	7" N	$1.32 \pm 0.28$	$-0.08 \pm 0.20$	$0.46 \pm 0.31$	$0.31 \pm 0.22$
	7" S	$1.56 \pm 0.23$	$0.46 \pm 0.21$	$-0.30 \pm 0.23$	$0.39 \pm 0.17$
NML Cyg	7" N	$0.62 \pm 0.13$	$0.18 \pm 0.04$	$0.46 \pm 0.03$	...
	7" S	$0.31 \pm 0.16$	$0.24 \pm 0.05$	$0.44 \pm 0.05$	...
IRC +10216	7" N	$0.59 \pm 0.11$	$0.59 \pm 0.08$	$0.57 \pm 0.08$	$0.45 \pm 0.09$
	7" S	$0.29 \pm 0.05$	$0.57 \pm 0.07$	$0.28 \pm 0.03$	$0.46 \pm 0.10$
IRC +10420	7" N	$-0.01 \pm 0.09$	$0.65 \pm 0.13$	$-0.12 \pm 0.11$	$-0.11 \pm 0.08$
	7" S	$0.38 \pm 0.08$	$0.65 \pm 0.13$	$0.12 \pm 0.10$	$-0.26 \pm 0.08$
CIT 6	7" N	$1.41 \pm 0.95$	$0.03 \pm 0.37$	$0.52 \pm 0.35$	...
	7" S	$1.57 \pm 0.72$	$0.36 \pm 0.17$	$0.13 \pm 0.15$	...



also correspond to the spatial profiles shown in Figure 4. These limits may then be compared with values of surface brightness expected on the basis of molecular outflow

densities.

The spectral flux for IRC + 10216 at wavelengths between 10 and 11  $\mu\text{m}$  (see Fig. 1b), to which the percent-

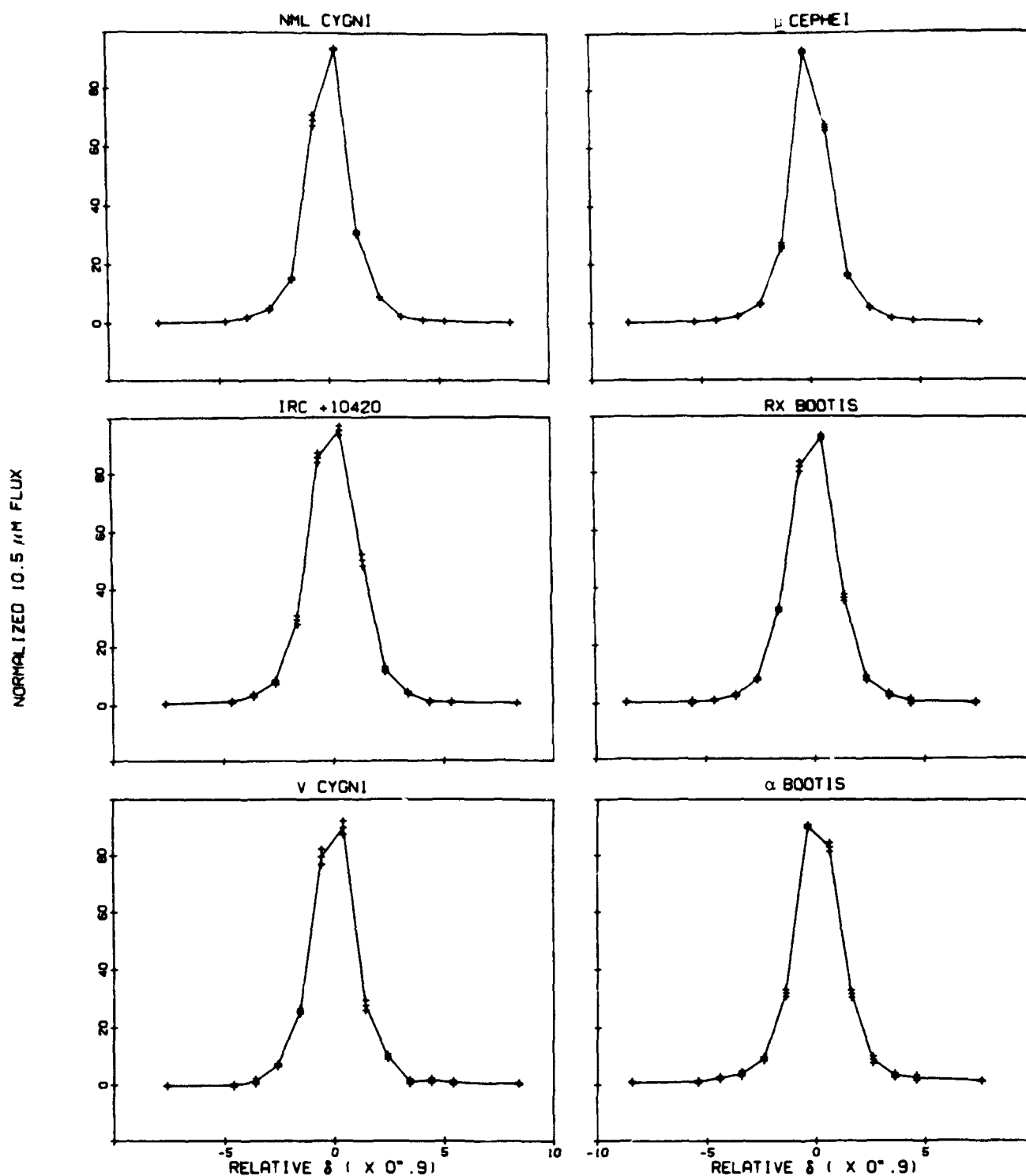


FIG. 4a—Normalized angular scans that were synthesized from ten wavelength elements between 10 and 11.5  $\mu\text{m}$  in the manner described in the text. The two scan endpoint values have been further averaged over five pixels within 2 arc sec of each endpoint. The values and uncertainties for these endpoints are listed in Table 3.

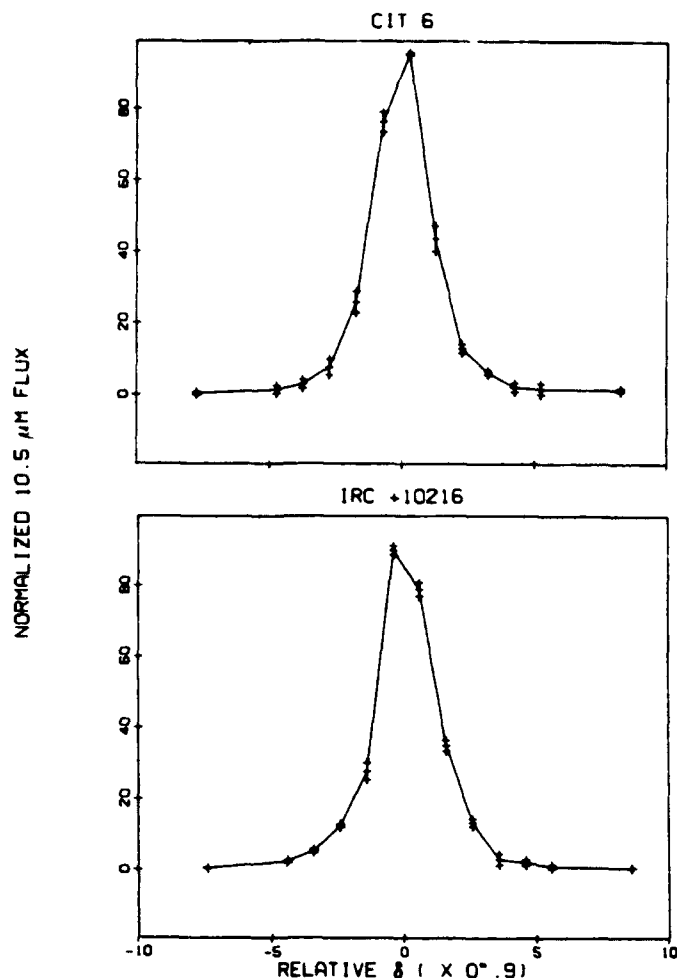


FIG. 4b—As for Figure 4a, but using only seven coarsely spaced wavelength elements between 10 and 12.1  $\mu\text{m}$  available for the single operational channel in March 1988.

ages in Table 3 refer, is  $9 \times 10^{-14} \text{ W cm}^{-2} \mu\text{m}^{-1}$ , or  $3 \times 10^4$  Jys. The surface brightnesses at the 3".5 and 7" positions are calculated from their percentages of the peak flux and from the spatial FWHM; these are listed in Table 4. The values of surface brightness must be considered true upper limits since instrumental effects clearly dominate at 3".5 and are also present at 7". Estimating a lower limit on the instrumental contribution at these positions of 75% and 50%, respectively, as assessed by the scans of CIT 6 on the same night, results in the final upper limits also listed in Table 4.

Expected values of absolute surface brightness based on the impact parameter model of Scoville and Kwan (1976) and observed molecular column densities were determined for the IRC +10216 envelope by LHJ at a wavelength of 50  $\mu\text{m}$  and an angular distance of 15" from the peak. We adopt the calculated value of LHJ and scale it to our wavelength and impact angles. The model equations of Scoville and Kwan lead to the form of the scaling equation presented below under the assumption that, for

TABLE 4  
IRC +10216 Outflow Brightness Limits

Pos (")	$S_\nu$ (Jy/arcsec <sup>2</sup> )		
	Observed <sup>a</sup>	Adopted Upper Limit <sup>b</sup>	Theoretical Lower Limit
3.5	520	130	82
7.0	54	27	4

Notes:

<sup>a</sup>Includes instrumental contribution.

<sup>b</sup>Based on lower limits of instrumental contribution estimated as 75% at 3".5 and 50% at 7".

sufficiently large impact parameters, the temperatures of all points along the line of sight are sufficiently low to permit the Wien form of the Planck function at both 10 and 50  $\mu\text{m}$ . To justify this assumption we note that for IRC +10216 detailed values of temperature are found in the literature; one of the larger values is 375 K at the assumed 1" inner envelope boundary (Toombs *et al.* 1972). A temperature decreasing with radius to the power of  $-0.5$  to  $-0.4$  results for the assumed models. Thus, the Wien approximation is seen to be valid for impact parameters up to 1" for 10- $\mu\text{m}$  radiation and to within 5" for 50  $\mu\text{m}$ . With these approximations and a transform of the standard distance variable of integration using trigonometric substitution, we obtain

$$r_\nu \equiv \frac{S_{\nu_1, p_1}}{S_{\nu_2, p_2}}$$

$$= \frac{Q_{\nu_1} \left( \frac{\nu_1}{\nu_2} \right)^3 \frac{p_2}{p_1} \int_0^{\pi/2} \exp\left(-\frac{h\nu_1}{kT_1}\right) (p_1 \sec x)^{0.4} dx}{\int_0^{\pi/2} \exp\left(-\frac{h\nu_2}{kT_1}\right) (p_2 \sec x)^{0.4} dx}, \quad (1)$$

where  $\nu_1$  and  $\nu_2$  are frequencies corresponding to wavelengths of 10.5 and 50  $\mu\text{m}$ , respectively,  $p_1$  and  $p_2$  are the angular impact parameters in the notation of Scoville and Kwan, and  $Q_\nu$  is the dust emissivity at frequency  $\nu$ . Here, the temperature distribution  $T = T_1 \theta^{-0.4}$  is adopted, where  $T_1$  is the temperature at 1" from the central source ( $T_1 = 310$  K, Martin and Rogers 1987). The form of equation (1) also depends on the inverse-square-law density with increasing radius that results from the assumption of steady mass-loss rates over the "crossing time" for a spherically symmetric envelope.

Evaluating the integrals numerically for  $p = 3".5$  and taking as a conservative lower limit three for the ratio  $Q_{10}/Q_{50}$ , we obtain the result  $r_\nu = 17$ . This value, combined with the 50- $\mu\text{m}$ , 15" surface brightness of 4.8 Jy arc sec<sup>-2</sup> derived by LHJ from the measured molecular

column densities and typical dust parameters, gives a lower limit of  $82 \text{ Jy arc sec}^{-2}$  for the surface brightness at  $10 \mu\text{m}$  and  $3.5''$ . For impact parameter  $p = 7''$  the ratio is equal to 0.75 and the lower-limit surface brightness is  $4 \text{ Jy arc sec}^{-2}$ . These results are listed in Table 4. The relative values of surface brightness at the two wavelengths and three impact parameters presented above agree well with the model of Martin and Rogers (1987). The absolute values are a factor of 4 higher, in close agreement with the factor of 3 density enhancement suggested by Martin and Rogers to bring their model into agreement with observation. It can be seen that the test is more sensitive for the  $3.5''$  angle and that the observed and predicted limits are in barely satisfactory agreement. The suggested inconsistency supports the conclusions of LHJ that predicted values are too large, due possibly to anomalously low values of dust emissivity and/or density in the IRC +10216 halo relative to the observed molecular densities. In order to subject the predicted limits to a harsher test, lower values for the observed upper limits must be obtained through more careful removal of the instrumental contribution at the  $3.5''$  impact angle made possible with longer integrations on the reference point source.

Since IRC +10216 lies at the near end of the range of distances estimated for the stars with pronounced circumstellar emission observed here (see Knapp *et al.* (1982 and references therein) and Zuckerman, Dyck, and Claussen (1986) for a more recent distance estimate to IRC +10216), the spatial scans of Figure 4 for the remaining stars correspond to larger radii as a consequence of their greater distance, and the densities and temperatures of the outflow material would in general be lower. Therefore, deviations from point-source scans due to halo radiation would be more difficult to assess.

#### 4. Conclusions

In an effort to address the question of relative variation of continuum and feature fluxes in long-period variable stars, we have compared the  $8\text{--}14 \mu\text{m}$  spectra of five such stars obtained by the LRS aboard IRAS in 1983 and observed by GLADYS in 1988. Three of the five stars possess carbon-rich atmospheres and exhibit SiC feature emission; the equivalent widths in all three of these objects show no appreciable difference between the two observing epochs. By contrast, the two stars with oxygen-rich atmospheres and pronounced silicate feature emission exhibit variation in equivalent widths at significant levels. We conclude that relative variation of continuum and emission feature fluxes may occur for at least some oxygen-rich, long-period variables, although the general nonphotometric nature of both instruments frustrates efforts to assess the continuum variability. In the case of the silicon carbide emission star V Cyg, we do find pronounced continuum variations that exceed the relatively high absolute-flux uncertainties; this level of variation

agrees with visible light-curve data from AAVSO.

Attempts to resolve the circumstellar shells were only marginally successful due to limitations imposed by diffraction and seeing. We find that upper limits on the surface brightness of the outflow material for the molecular outflow source IRC +10216 compare favorably with calculated lower limits and provide no additional constraints on depressed dust emission drawn in the literature on the basis of far-infrared detections of the outflows.

We should note that we are continuing to monitor the  $10\text{-}\mu\text{m}$  spectra of the objects discussed above, with improvements to the observing configuration discussed here. First, we have implemented a new data-acquisition system for GLADYS at the Wyoming Infrared Observatory that has already proven to be more efficient during a recent observing run. Second, we plan to install a new detector array in the spectrometer; this array is similar to the one discussed in this paper, but projected to be five times more sensitive.

We are grateful to Peter Tandy for his continually available engineering assistance during the two observing runs described here and several earlier engineering runs. Tom Hayward and James Benson provided key support during earlier runs; this support and their insights are gratefully acknowledged, as are the useful discussions with G. L. Grasdalen. The staff of the Wyoming Infrared Observatory supported these observing runs most efficiently. This research was supported by the Air Force Office of Scientific Research, which also provided summer 1987 support for G. S. at AFGL.

*Note added in press:* Volk and Cohen (1989) have obtained a spectrum of RX Boo from the LRS database. The LRS spectrum qualitatively agrees with ours; the smaller-scale structure seen in it lies at our noise level.

#### REFERENCES

- Benson, J. A., Turner, N. H., and Dyck, H. M. 1989, *A. J.*, **97**, 1763.
- Bloemhof, E. E., Danchi, W. C., Townes, C. H., and McLaren, R. A. 1988, *Ap. J.*, **333**, 300.
- Bloemhof, E. E., Townes, C. H., and Vanderwyck, A. H. B. 1984, *Ap. J. (Letters)*, **276**, L21.
- Dyck, H. M., Zuckerman, B., Howell, R. R., and Beckwith S. 1987, *Pub. A.S.P.*, **99**, 99.
- Dyck, H. M., Zuckerman, B., Leinert, Ch., and Beckwith, S. 1984, *Ap. J.*, **287**, 801.
- Fazio, G. G., McBreen, B., Stier, M. T., and Wright, E. L. 1980, *Ap. J. (Letters)*, **237**, L39.
- Fix, J. D., and Cobb, M. L. 1988, *Ap. J.*, **329**, 290.
- Forrest, W. J., Gillett, F. C., and Stein, W. A. 1975, *Ap. J.*, **195**, 423.
- Jones, B., and Rodriguez-Espinosa, J. M. 1984, *AFGL-TR-84-0114*, NTIS ADA156189.
- Kholopov, P. N., *et al.* 1985, *General Catalogue of Variable Stars* (Moscow: Nauka) (VSC).
- Knapp, G. R., Phillips, T. G., Leighton, R. B., Lo, K. Y., Wannier, P. G., Wootten, H. A., and Huggins, P. J. 1982, *Ap. J.*, **252**, 616.
- Lester, D. F., Harvey, P. M., and Joy, M. 1986, *Ap. J.*, **304**, 623 (LHJ).
- LeVan, P. D. 1990, *Pub. A.S.P.*, **102**, February.

- Little-Marenin, I. R. 1986, *Ap. J. (Letters)*, **307**, L15.
- Mariotti, J. M., Chelli, A., Foy, R., Léna, P., Sibille, F., Tchountonov, G. 1983, *Astr. Ap.*, **120**, 237.
- Martin, P. G., and Rogers, C. 1987, *Ap. J.*, **322**, 374.
- Mattei, J. A. 1988, *AAVSO Bull.*, No. 51.
- . 1989, private communication.
- McCarthy, D. W., Howell, R. R., and Low, F. J. 1980, *Ap. J. (Letters)*, **235**, L27.
- Nye, E. P., and Merrill, K. M. 1980, *AFGL-TR-80-0050*, NTIS ADA084098.
- Olnon, F. M., and Raimond, E. 1986, *Astr. Ap. Suppl.*, **65**, 607.
- Olofsson, H., Johansson, L. E. B., Hjalmarson, A., and Nguyen-Q.-Rieu 1982, *Astr. Ap.*, **107**, 128.
- Scoville, N. Z., and Kwan, J. 1976, *Ap. J.*, **206**, 718.
- Sutton, E. C., Betz, A. L., Storey, J. W. V., and Spears, D. L. 1979, *Ap. J. (Letters)*, **230**, L105.
- Tamura, M., Hasegawa, T., Ukita, N., Gatley, I., McLean, I. S., Burton, M. G., Rayner, J. T., and McCaughrean, M. J. 1988, *Ap. J. (Letters)*, **326**, L17.
- Toombs, R. I., Becklin, E. E., Frogel, J. A., Law, S. K., Porter, F. C., and Westphal, J. A. 1972, *Ap. J. (Letters)*, **173**, L71.
- Volk, K., and Cohen, M. 1989, preprint.
- Zuckerman, B., Dyck, H. M., and Claussen, M. J. 1986, *Ap. J.*, **304**, 401.

**Appendix B**  
**Capabilities of the AFGL Mosaic Array Spectrometer—Ten-Micron Spectra of Bright Infrared Stars**

## CAPABILITIES OF THE AFGL MOSAIC ARRAY SPECTROMETER—TEN-MICRON SPECTRA OF BRIGHT INFRARED STARS

PAUL D. LEVAN

Geophysics Laboratory (Air Force Systems Command), Hanscom Air Force Base, Massachusetts 01731-5000

Received 1989 July 25, revised 1989 November 13

### ABSTRACT

A 9- to 14- $\mu\text{m}$  slit spectrometer employing a novel mosaic array of  $58 \times 62$  detectors is described. The spectrometer has been used on the University of Wyoming 2.3-m telescope with a 0".9 per pixel (reimaged) plate scale to obtain spectra of long-period variable stars. We characterize the instrumental spectral resolution and spatial point-spread function using spectra and spatial profiles extracted from spectral images of the variable stars. In order to evaluate the effectiveness of our data-acquisition and reduction procedures, our spectra are compared with examples found in the Atlas of IRAS Low Resolution Spectra. The comparisons are made for single representatives of each of three diverse object classes—oxygen-rich stars with strong silicate feature emission, carbon-rich stars with silicon carbide emission, and late-type stars exhibiting photospheric continuum radiation. We conclude that: (1) The IRAS and array spectrometer spectra are in qualitative agreement if account is taken of the extension of the silicate feature flux to wavelengths shortward of the 9- $\mu\text{m}$  cut-on wavelength of our instrument. (2) The spectral resolution of our spectrometer is as expected for the slit width employed. (3) The width of the spatial point-spread function is nearly as good as the design goal. (4) The formal uncertainties of our data points are high even when the relatively low responsivity of the mosaic array is considered and are suggestive of system noise limited performance.

**Key words:** instrumentation—array detectors—IR spectroscopy

### 1. Introduction

Recent examples of the use of mosaic infrared arrays in ground-based astronomical cameras in the ten-micron region are readily found in the literature (Arens *et al.* 1984; Bloemof, Townes, and Vanderwyck 1984; Tresch-Fienberg *et al.* 1987; Gezari *et al.* 1988). However, such arrays also lend themselves nicely to long-slit spectroscopic applications for which radiation is dispersed along one of the array axes. Array slit spectrometers have a substantial advantage over single-detector wavelength scanning spectrometers since all wavelength elements are measured simultaneously. Hence, the shape of the spectrum is unaffected by variations in atmospheric transmission. Using a two-dimensional array in our spectrometer also permits the acquisition of long-slit spectra of extended sources.

The design of the prism spectrometer discussed here is similar in its choice of dispersing element to a discrete bolometer array spectrometer built by Gehrz, Hackwell, and Smith (1976); our design is discussed in some detail in workshop proceedings (LeVan and Tandy 1987, hereafter Paper I; LeVan 1989). Here we briefly review the design, discuss upgrades to the spectrometer, and describe the results of recent observing runs. After reviewing the

instrument and telescope tests, we next discuss the spectra obtained for our program stars. Next, observed noise characteristics are compared with those expected for a mosaic array operated under background-limited conditions. Finally, the spatial point-spread function is determined from monochromatic profiles of the program star exposures.

### 2. The Spectrometer

#### 2.1 Mosaic Array Clocking

The detector array is a Santa Barbara Research Center (SBRC) 58 by 62 pixel Si:Ga photoconductor array "Indium bump bonded" to a CRC-228 Direct Read Out (DRO) multiplexer, whose properties are listed in Table 1. A circuit diagram for one of the 1798 pixel unit cells is shown in Figure 1. The DRO has two signal output lines. Each line is driven by an on-chip MOSFET source follower circuit, and a single array address code transfers the signal simultaneously from each of two adjacent pixels. Because of the spectral resolution of the spectrometer and the high background photon rates in the thermal infrared, pixels are clocked continuously at 333 kHz, giving a 3- $\mu\text{sec}$  pixel "window" during which  $\delta$ -Reset Sampling (DRS) may be performed. Source follower bias voltages and load resistance values were optimized to allow for

TABLE 1

Mosaic Array Attributes

Pixel format.....	58x62
Pixel spacing.....	75 $\mu\text{m}$
Photoconductor material..	Si:Ga
Multiplexer read mode....	Random access; direct output
Multiplex ratio.....	1798 pixels / output channel
Well capacity.....	$3 \times 10^6 \text{ e}^-$
Responsivity <sup>a</sup> .....	< 0.4 A/W
Uniformity.....	< 5 % rms

<sup>a</sup>Read-out noise is below LSB of 12 bit full-well conversion

<sup>b</sup>Manufacturer goal of high pixel response uniformity was obtained at the expense of lowered responsivity (private communication with manufacturer, Santa Barbara Research Corporation).

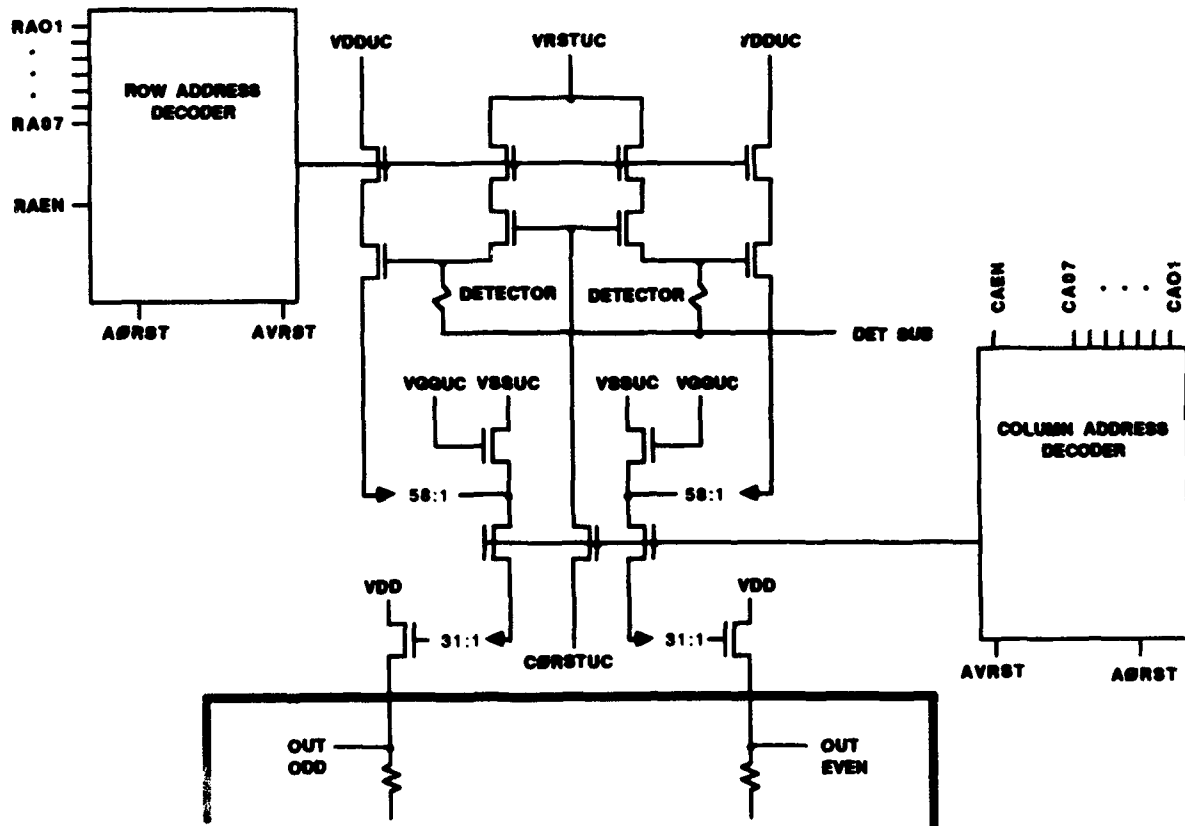


FIG. 1—Circuit drawing of one of 1798 total pixel unit cells (UC) shown with the address electronics and two source followers. Acronyms refer to bias and clock voltages supplied externally via the chip carrier: RA-n and CA-n refer to row and column address clocks. VDD, VGG, and VSS are the usual MOSFET terminology for drain, gate, and source bias voltage. AØRST denotes the address reset clock voltage that is required prior to a new address selection, and CØRST is the signal charge reset clock voltage. Load resistors for biasing the two source followers that are shown below the shaded border are supplied by the user at an off-chip location.

settling of signals during the clamp and sample of DRS. The integration time per pixel, equal to the clock period

multiplied by the number of pixels per output line (1798), is 5.4 msec. Further details on the laboratory cryogenic

(10 K) testing of the array are contained in Paper I.

## 2.2 The Coaddition Electronics

Electronics for real-time coadditions of digitized array frames is based on Arithmetic Logic Units (ALUs) and was designed at the Air Force Geophysics Laboratory (AFGL). The ALU design was selected over a microprocessor-based design to allow for higher frame coaddition rates (see also Paper I). The coaddition electronics provides two separate RAM blocks of 3596 20-bit memory sites to allow for the standard IR astronomy technique of secondary mirror chopping of the source and blank sky. Coaddition suppression after each chop during the settle time of the secondary mirror prevents corruption of the summed frames. The register contents corresponding to the two telescope chop positions are differenced by the ALUs and transferred to a minicomputer for storage on hard disk before overflow of the 20-bit RAM block (fewer than 256 array frames).

## 2.3 Electronics Testing

Early laboratory testing disclosed significant clocking noise on the common analog and digital electronics grounds at the level of several bits of our 12-bit A to D converter and higher than the shot noise of a full pixel well. This resulted in our redesigning the analog electronics boards with considerable attention to isolation of the digital, bias voltage, and signal grounds. The two A to D converters were also upgraded to improved 16-bit devices with front-end sample and hold and a 2.7- $\mu$ sec conversion time (Analogic Corp., Wakefield, MA). The upgraded circuitry is used in an equivalent 12-bit mode.

A problem that affected initial observing runs was electronic "spiking" of a significant percentage of the pixels before transfer of the summed frames to the computer. (Software corrections for spiking were discussed in LeVan and Sloan (1987).) Because of their predominance on only one of the two output channels, the origin of the spikes was determined to be the digital electronics. It was further determined by repeating the transfer of data differences between registers corresponding to the two telescope chop positions that the spiking occurred during data acquisition. Subsequent changes in the relative timing of the A to D converter data latching pulses sent to the two "chop" registers significantly reduced the spiking in the affected channel.

## 2.4 Prism Spectrometer Optics

The optics design summarized in Table 2 is based on a NaCl prism. A prism was selected as the dispersing element for operation over a broad wavelength range (9 to 14  $\mu$ m) over which a grating efficiency would vary substantially. Our design has no cryogenically cooled moving parts. However, a simple cold blocking shutter is recommended for future designs to facilitate testing. In constructing the optics (Sensors Systems Group, Waltham,

MA) care was taken to stress relieve the mirrors at the three substrate attachment points. This design was found to have good alignment stability between room temperature and 10 K. A picture of the optical assembly is shown in Figure 2. A detailed, scaled schematic of the ray trace is given in Paper I.

## 3. Data Acquisition

Setup at the observing site for infrared observations involves a range of procedures too numerous to mention; we concentrate below on those aspects of the setup specific to our array spectrometer.

### 3.1 Observing Setup: Electronics

The relative phases of a 333 kHz master clock and three subsidiary clocks are adjusted within the 3- $\mu$ sec "pixel window", by displaying the pixel signals resulting from  $\delta$ -reset sampling on an oscilloscope. The pixel signal reset clock pulse is delayed relative to the pixel address pulse to allow for settling of the signal level. The clamp pulse (which restores the signal to the zero voltage level) is delayed to just prior to pixel reset. The sample pulse initiates both sample and hold and the A to D conversion, as discussed in Section 2.3. The relative timing of the sample clock is delayed to the end of the pixel "window" (just prior to the new pixel address). The reset pixel signal settles in the form of a linear ramp to a pedestal value; the procedure outlined here allows a time interval sufficiently long to accommodate increased background or bright source signals that require proportionally longer settle times. Our electronics also generates a telescope secondary mirror chop waveform, ensuring synchronization with the array clocking. We tune the amplitude (27") and offset of the chop signal square wave using the signal from the mirror position transducer. A check is made for cancellation of the background signal in the positive and negative chop registers.

TABLE 2

Prism Spectrometer Attributes and Spectral Dispersion

Pixel	x (mm)	$\lambda$ ( $\mu$ m)
1	0.04	9.9
15	1.10	10.7
30	2.24	12.3
45	3.38	13.7
60	4.52	14.5

Prism material.....	NaCl
F <sub>collimator</sub> .....	270 mm
F <sub>camera</sub> .....	75 mm
Lyot stop diameter..	10 mm
Slit dimensions.....	0.9x16 mm
	3.3x58 pixels



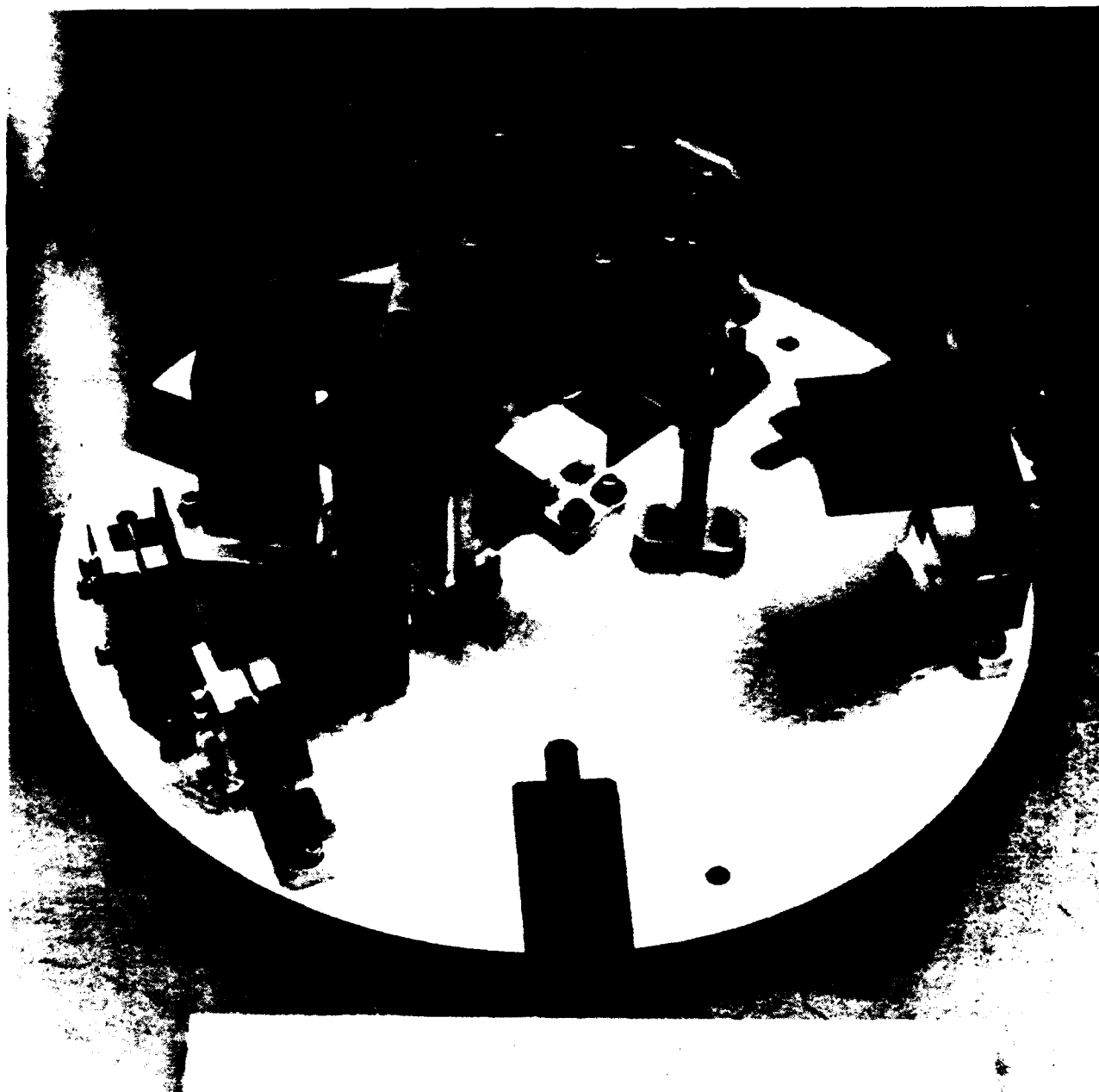


FIG. 2—The spectrometer optics, shown inverted relative to its attitude as mounted in the dewar. The material used for construction is Al; the mirror surfaces are coated with Ni. Gaps visible in the mirror assemblies provide stress relief by decoupling the mirror surfaces from the substrate mounting points. The NaCl prism is held in place with spring steel. The assembly was built to our design by Sensors System Group of Waltham, MA.

### 3.2 Observing Setup: Optical Alignment

Optical alignment consists of ensuring that the dewar field of view is centered on the telescope secondary mirror. This is accomplished using the signal of a selected pixel resulting from a warm radiation source positioned at the telescope secondary mirror. By displaying this signal on an oscilloscope it may be maximized by tilting a reflecting mirror. The widespread alternative method of adjustment of the reflecting mirror for minimum background signal *without the warm radiation source* was attempted

without success. This may be due to scattering internal to the spectrometer of an appreciable component of background signal from outside of the reflecting mirror solid angle.

### 3.3 Background Subtraction

Subtraction of the sky and telescope background from the source frames is effectuated by chopping the secondary mirror of the telescope at 3 Hz. The chop direction is along the north/south axis as is the orientation of the

spectrometer slit. The chop amplitude is one-half the 54" slit length. After seven pairs of source and blank sky chops, data collection is suspended while the differences of the frames coadded into the two chop registers are transferred to computer. This sequence is repeated 20 times for a fixed telescope position. The telescope is then noddled. Care was taken in adjusting the chop and nod amplitudes since any mismatch between them results in a spatial smearing of the source on combination of the positive and negative source frames. Nodding the telescope removes first-order spatial variation of the background. The 20 frame transfers per telescope nod position are transported off the mountain for subsequent processing.

### 3.4 Optical Calibration: Positional

The array plate scale and wavelength calibrations relate to array pixel spacing and optics magnification and dispersion listed in Table 2. The array plate scale was verified by moving a point source by fixed telescope pointing increments. The 0".9 per pixel slope of the fit to the point-source spatial peaks and telescope pointing offsets is consistent with the telescope plate scale ( $3".27 \text{ mm}^{-1}$ ), the pixel spacing, and the spectrometer magnification.

### 3.5 Optical Calibration: Spectral

Polystyrene film was inserted into the telescope beam at the dewar window with a background source in view. The polystyrene spectrum shown in the lower panel of Figure 3 was generated as the ratio of background source spectra with and without polystyrene in the beam; also shown is a reference spectrum synthesized from data supplied with the polystyrene which also included wavelengths for the principal features (Beckman Instruments, Inc., Irvine, CA). Four weak and a single strong absorption feature labeled 11, 12, 13, 13', and 13'' are visible on the reference spectrum and have wavelengths listed in Table 3. The Image Reduction and Analysis Facility (IRAF)<sup>1</sup> was used to fit the absorption wavelengths in pixel coordinates and to interpolate the original flux samples onto a linear wavelength grid of  $0.109\text{-}\mu\text{m}$  spacing. This procedure was applied to all spectra discussed subsequently. Excerpted values of the wavelength calibration are listed in Table 2 where 45 pixels are seen to be in the useful range of atmospheric transmission. Calculated pixel wavelengths based on values of  $dn/d\lambda$  for NaCl and the spectrometer design are published elsewhere (LeVan and Sloan 1987). The calculated wavelengths are in good relative agreement with the polystyrene calibration discussed here.

The spectral resolution illustrated by the polystyrene spectra is for a relatively large slit width (3" at the present

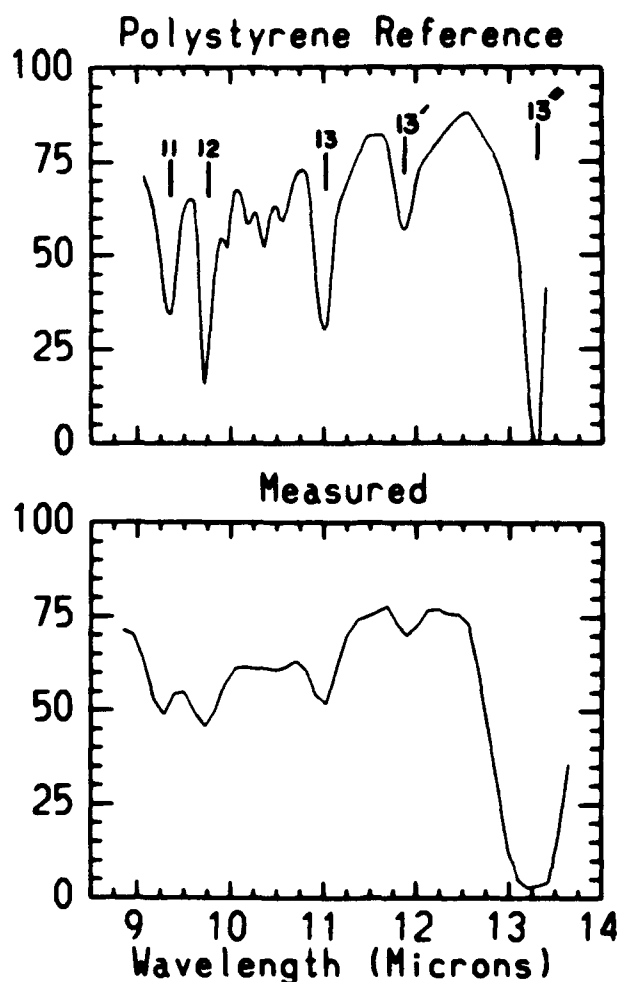


FIG. 3—Spectra of polystyrene calibration film resulting from an exposure of Mars as a background source. Instrumental response and atmospheric transmission variations with wavelength are eliminated in the ratio of spectra with and without polystyrene in the telescope beam (bottom panel). The reference spectrum (top panel) is synthesized from data supplied by the manufacturer of the polystyrene sample. Absorption feature identifications correspond to those of Table 3. The spectral resolution is not optimal since the background source (Mars) was imaged onto a 3"-wide slit and a slit width as small as 1" may be used under the appropriate conditions of atmospheric seeing. The spectral flux values have been interpolated onto a linear wavelength grid using the IRAF Onedspec package.

TABLE 3  
Polystyrene Absorption Wavelengths

Reference	$\lambda (\mu\text{m})$
11	9.35
12	9.73
13	11.03
13'	11.91
13''	13.28

<sup>1</sup>IRAF is distributed by National Optical Astronomy Observatories, which is operated by the Association of Universities for Research in Astronomy, Inc., under contract to the National Science Foundation.

telescope plate scale) installed prior to cryogenically cooling the spectrometer. However, slit widths as small as 1" may be used under good seeing conditions. Since the spectral resolution using the 3" slit is an approximate factor of 3 worse than the design goal, one may expect higher resolutions for smaller slit widths.

It is also of interest to note that the polystyrene spectra obtained in June 1988 using Mars as a background source are spatially extended over approximately 10", simulating a spectrally structured extended source. These spectra exhibit a shift to shorter wavelengths to the north and indicate a rotational misalignment between the slit edges and spectrometer axes as defined by the prism orientation. This misalignment poses no difficulty for point sources and may be easily corrected in extended source observations by using the flux-conserving rotational operations in the IRAF.

### 3.6 Flux Calibration

Observations of bright, variable infrared stars were made at various positions along the spectrometer slit. The relative signals for spectral pixels at a fixed slit position result in correction coefficients for atmospheric and instrumental transmission variations with wavelength, for the "mean" detector responsivity variation with wavelength, and for pixel-to-pixel variations in responsivity. The stellar flux-based calibration is obtained with longer integrations on nonvariable standard stars (e.g.,  $\alpha$  Bootis,  $\alpha$  Tauri, and  $\beta$  Geminorum) at a single position in the slit that overlaps any of the aforementioned positions. Sky-emission measurements were taken at zenith and at larger zenith angles with the telescope chopper off in order to flat field pixels parallel to the slit length. The sky signals are composed of a constant offset term (the telescope background and electronics offsets) and a term proportional to air mass. The difference of the signals at the two air masses is thus proportional to detector responsivity. Relative responses result for monochromatic pixels parallel to the long slit edge. The relative responses of all pixels in the array were set by combining the spectral and spatial calibrations. In practice, the responsivity variation for pixels in the present array is very low (less than 5% rms) which is due in part to the low overall array responsivity (see Table 1).

## 4. Data Reduction

### 4.1 Output Frame Coaddition

Data frames transferred from the coaddition electronics have been coadded electronically over a 2-sec interval (corresponding to 5 or 7 secondary mirror chop cycles). We define an exposure as 80 such frames, in groups of 20 corresponding to a fixed telescope nod position. Exposures are processed by pair-wise differencing of frames corresponding to the positive and the negative nod positions. The running sum of pair-wise-differenced frames

has the residual due to the sky and telescope backgrounds removed (as opposed to the case of coadding the frames in the sequence they were collected). Spikes are eliminated during the coadding, and the number of acceptable values for each pixel is used in the calculation of the average. The sum of the squares of pixel signals is used for the calculation of the standard deviation of the mean. The standard deviations of the mean are the formal uncertainties for subsequent analysis.

### 4.2 Atmospheric Correction Coefficients

An average spectral correction for mean atmospheric and instrumental spectral variations was applied to all pixels in columns perpendicular to the slit long axis. Next, these pixels were multiplied by their unique flat-field coefficients that account for differences from the average spectral correction. Finally, columns of spectral pixels were multiplied by their inverse relative responses as determined by the sky emission flats.

### 4.3 Rotational Misalignment Correction

A 1° misalignment of the prism axes relative to the mosaic array edges results in systematic changes in the slopes of spectral rows of pixels about the peak spectral row. The effects of the rotational misalignment are also evident by shifts of peak spatial emission with wavelength in the amount of 0.012 spatial pixel per spectral pixel. We correct for the misalignment by removing the slope residuals using a model that assumed a Gaussian form for the point-spread function. The functional form for the Gaussian exponent in our model included the usual spatial dependence along with a coupling term between the spatial and spectral axes. The coupling term was determined in a least-squares fashion as the value given above. The Gaussian fit removed both the slope bifurcation and the shift of spatial peak with wavelength.

## 5. Observational Results

### 5.1 Observed Stars

For the purposes of the present paper we limit our discussion to a set of three stars taken from the larger observing list of LeVan and Sloan (1989). The three stars are representative of three distinct classes: oxygen-rich stars with strong silicate emission (IRC + 10420), carbon stars with silicon carbide emission (V Cygni), and late-type stars having presumed photospheric radiation for which a blackbody spectral distribution is adopted (Arcturus). These three stars were observed on 1988 June 4 UT with at least four exposures (as defined in Section 4.1) each. The absolute flux levels of the spectra were set using the 11- $\mu$ m flux shown in Figure 4 for Arcturus. The uncertainty in the absolute levels given by repeated exposures is estimated at 25%. We plot the sum of spectra over the spatial point-spread function in Figure 4. Spectra have been regridded on a linear wavelength scale using IRAF, as described in Section 3.5.

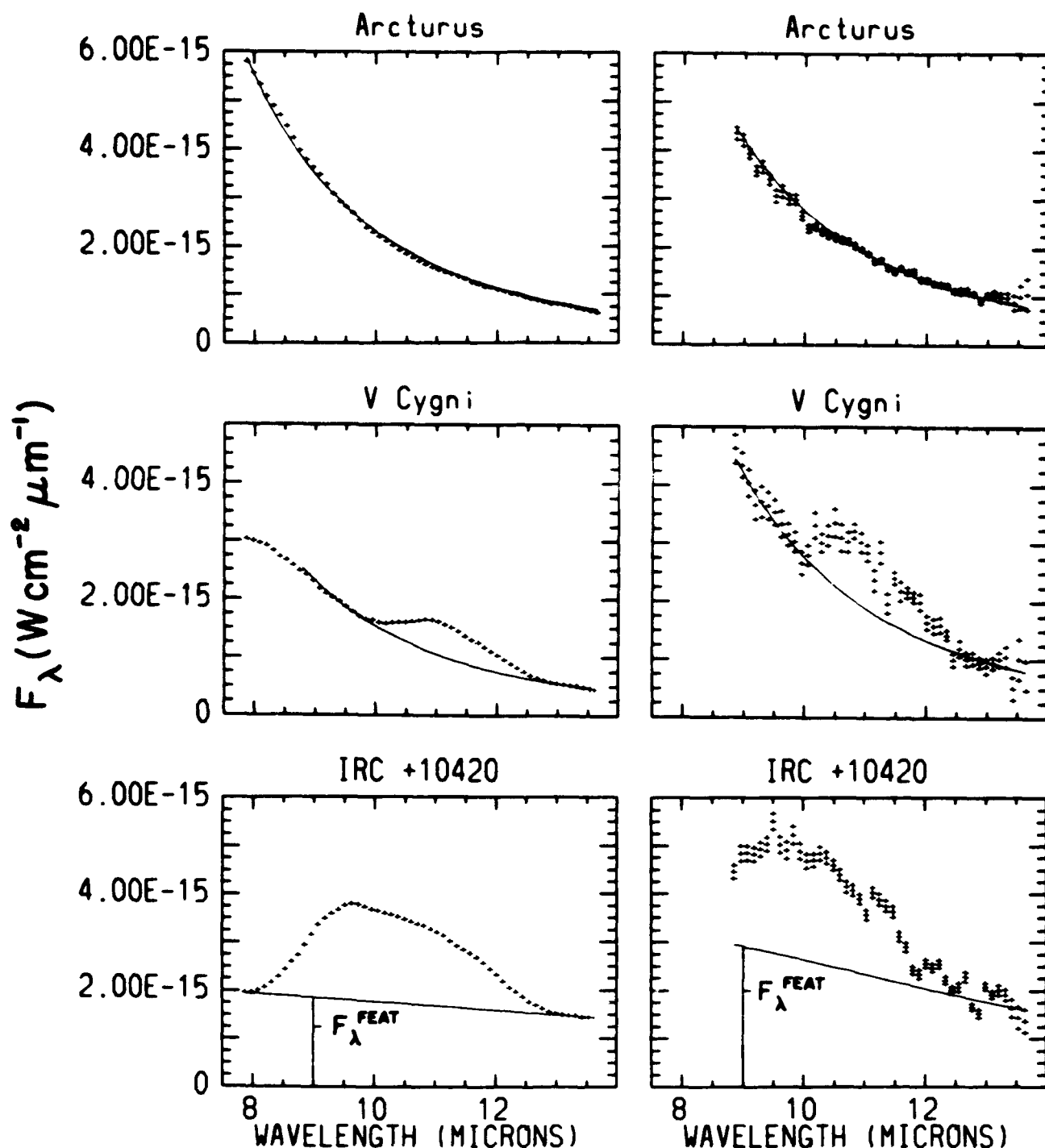


FIG. 4—Spectra for the three classes of infrared stars observed. Shown are spectra obtained by IRAS (left) and included in the Atlas of IRAS Low Resolution Spectra (Olson and Raimond 1986) and those obtained with the mosaic array spectrometer (right). The array spectra result from a single mosaic array exposure of two-minutes duration. Peak and subsidiary spectra have been summed over the spatial point-spread function. Blackbody fits to the continua are shown, in the case of Arcturus to aid in evaluating the accuracy of the correction for atmospheric absorption and in the two remaining stars for the comparison of emission feature equivalent widths measured by the two instruments. The blackbody fit for IRC +10420 is based on the ratio of LRS feature and continuum fluxes at the short-wavelength cut-on of the spectrometer, as indicated graphically. Our spectral fluxes have been interpolated onto a linear wavelength grid using the IRAF Onedspec package.

## 5.2 Spectra: Comparison with IRAS Low-Resolution Spectra

In order to evaluate the effectiveness of our data-acqui-

sition and reduction techniques, we compare our spectra with those obtained with the IRAS Low-Resolution Spec-

trometer (LRS) and contained in the Atlas of IRAS Low-Resolution Spectra (Olson and Raymond 1986, LRS Atlas hereafter). The LRS Atlas includes entries for all three of the stars considered here. First, we note the agreement for the two instruments in the blackbody fit to the continuum of Arcturus. In the cases for the emission feature stars, blackbody fits to the continuum are made for the purpose of comparing the LRS and array spectrometer spectra and are not to be taken as representative of temperatures of either dust grains or the underlying star. Based on the LRS spectrum of the silicate emission star IRC +10420, we see that the continuum blueward of the silicate feature is not sampled by our spectrometer. This is because the wavelength coverage of our instrument is shifted longward to a 9- $\mu$ m cut-on wavelength as a result of translational misalignment of the optics assembly relative to the mosaic array. At the scale of about 0.1  $\mu$ m in wavelength per pixel, the observed 1- $\mu$ m wavelength shift corresponds to about 0.7 mm of translation. For silicate feature spectra observed with the array spectrometer the blackbody fits to the continua must be chosen such that the short wavelength ratio of feature and continuum levels is equal to that of the LRS spectra at 9  $\mu$ m. In order to facilitate this procedure we list in Table 4 wavelengths corresponding to a geometric progression of ratios of silicate feature to continuum fluxes obtained from the blackbody fits to the LRS spectra of IRC +10420 and  $\mu$  Cephei. We note that this feature in the former star, with its larger equivalent width, is also more extended to the shorter wavelengths. The results in Table 4 indicate that for IRC +10420 the silicate feature strength relative to the continuum at 9  $\mu$ m is approximately 0.75. This ratio is indicated graphically for IRC +10420 in the bottom panels of Figure 4. The correction to the overall feature flux due to feature emission shortward of 9  $\mu$ m is less than 10% for IRC +10420 and involves a correspondingly small uncertainty. A larger source of uncertainty in the equivalent-width determination results from the placement of the short-wavelength intercept, e.g., a somewhat underestimated continuum level will significantly overestimate the equivalent width. The uncertainty of the reported value of silicate feature equivalent width which combines both corrections is 10%. For  $\mu$  Cep the value of the feature to continuum ratio at 9  $\mu$ m is closer to 0.4. The

estimation of silicate feature equivalent width for most other stars involves smaller ratios of 9  $\mu$ m feature to continuum flux than that for IRC +10420 and smaller uncertainties.

For stars exhibiting SiC feature emission (e.g., V Cyg), the spectral coverage of the array spectrometer embraces the continuum both short and longward of the feature. The shapes of the spectra of V Cyg for the two instruments are in satisfactory agreement. The shift in the absolute flux levels exceeds the level of photometric uncertainty and may be attributed to long-period variability (LeVan and Sloan 1989).

A visual comparison between the LRS and array spectrometer spectra indicates the presence of more small-scale structure in the array spectra. This structure reflects the limitations of our correction for atmospheric attenuation and is best quantified by the deviations between the LRS and array spectrometer spectra of Arcturus. The relative smoothness of the LRS spectra results from the absence of residuals from atmospheric correction and the higher sensitivities possible with a cryogenically cooled telescope operated under the lower background levels outside the Earth's atmosphere (Beichman *et al.* 1985).

The standard deviations of the mean of the array spectrometer spectra are large given the 2-minute integration time and the brightnesses of the program stars. Part of the reason for the low signal-to-noise ratio is traceable to the overall low responsivity of the mosaic array (see Table 1), which accounts for perhaps a factor of 5 of the total factor of 200 degradation of our spectrometer relative to the expected sensitivity. Therefore, additional noise sources in our system must account for the majority of the degradation and these are presently under investigation.

### 5.3 Spatial Profiles

The spectral images obtained for the three stars discussed above are useful in the determination of the point-spread function (PSF) of our spectrometer. The experimentally determined PSF can be compared with that expected from the spectrometer design. The profiles displayed in Figure 5 result from summing normalized, monochromatic profiles extracted from single exposures at ten equally spaced wavelengths between 10 and 11.5  $\mu$ m. The two outermost points have been averaged further over 5 pixels within 2" of each point. The three profiles shown appear equivalent within the uncertainties and may be characterized by a Gaussian with a  $\sigma$  value of 0.8. In comparing with our expected value of  $\sigma$ , we use the brightness distribution for diffraction at a circular aperture displayed graphically in Born and Wolf (1964). We note the very good agreement of a Gaussian fit to the primary maximum of the normalized brightness profile down to 5% of peak level, beyond which the first minimum falls sharply below the Gaussian fit. From the Gaussian fit to the calculated diffraction profile at a wave-

TABLE 4

Wavelengths for Fixed Low Resolution Spectra  
Feature to Continuum Ratios

Star	Feature Equivalent Width ( $\mu$ m)	$\lambda$ ( $\mu$ m) 0.5% 10% 20% 40% 80%				
		5%	10%	20%	40%	80%
IRC +10420	3.2	8.14	8.25	8.39	8.63	9.05
$\mu$ Cep	2.0	8.34	8.44	8.66	8.97	9.42

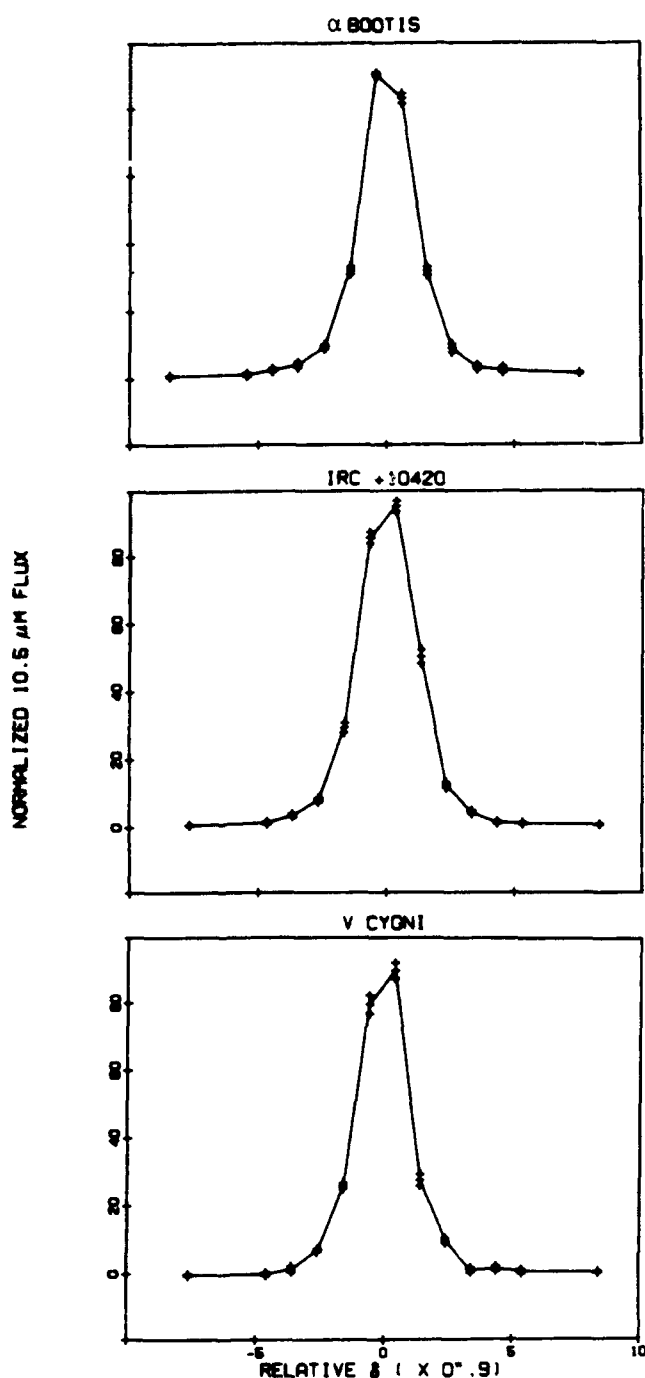


FIG. 5—Angular profiles obtained at positions along the slit using the same mosaic array exposures as for the spectra shown in Figure 4. These profiles are the sum of ten normalized, monochromatic profiles obtained at discrete wavelengths between 10 to 11.5  $\mu$ m. The two endpoints have been further averaged over 5 pixels within 2'' of each endpoint.

length of 11  $\mu$ m, we find telescope diffraction contributes a Gaussian  $\sigma$  value of 0''.39. The spectrometer contribution to the PSF derives from diffraction of the 1-cm-diameter collimated beam at the Lyot stop, and contributes a 33- $\mu$ m blur (Gaussian  $\sigma$ ) on the mosaic array, which

corresponds for the array plate scale to 0''.38 on the sky. In order to reproduce the observed Gaussian  $\sigma$  value of 0''.8, a combination of seeing effects and scattering within the spectrometer in amounts not exceeding 0''.4 (Gaussian  $\sigma$ ) is required.

## 6. Conclusions

The evaluation of a slit spectrometer using a mosaic array in the ten-micron region has shown promising results. Spectra were obtained whose qualitative attributes are comparable to those scanned by the IRAS satellite and published in the Atlas of IRAS Low-Resolution Spectra (Olson and Raimond 1986). The comparison is made for three complementary object classes—oxygen-rich stars with strong silicate feature emission, carbon stars with SiC feature emission, and late-type nonvariable stars with photospheric radiation—and permits the following conclusions: (1) Overall shapes of the IRAS and array spectrometer spectra agree if account is taken of the extension of the silicate feature flux to wavelengths shortward of the 9- $\mu$ m cut-on wavelength of our instrument. (2) The spectral resolution of our spectrometer matches values expected for the relatively large slit width employed. (3) The width of the spatial point-spread function is close to the design goal but, nevertheless, consistent with either scattering within the spectrometer or a 1'' FWHM seeing disk. (4) The noise values of our data points are high even when the relatively low responsivity of the mosaic array is accounted for and are suggestive of non-background-limited performance.

We acknowledge the staff of the Wyoming IR Observatory (WIRO) for providing observational time on the 2.3-m telescope and substantial interface support for the spectrometer described here. WIRO graduate students J. Benson, K. Klett, T. Hayward, and G. Sloan all contributed on various observing runs. Peter Tandy of the Geophysics Laboratory was the electronics engineer responsible for many of the electronics subsystems. Dr. Richard Puetter is gratefully acknowledged for having provided comments leading to the clarification of the original manuscript. This research was supported during its observational phase by the Air Force Office of Scientific Research.

## REFERENCES

- Arens, J. F., Lamb, G. M., Peck, M. C., Moseley, H., Hoffmann, W. F., Tresch-Fienberg, R., and Fazio, G. G. 1984, *Ap. J.*, **279**, 685.
- Beichman, C. A., Neugebauer, G., Habing, H. J., Clegg, P. E., and Chester, T. J., eds. 1985, *IRAS Catalogs and Atlases—Explanatory Supplement* (Washington, DC: U.S. Government Printing Office).
- Bloemof, E. E., Townes, C. H., and Vanderwyck, A. H. B. 1984, *Ap. J. (Letters)*, **276**, 121.
- Born, M., and Wolf, E. 1964, *Principles of Optics* (New York: Mac-Millan).
- Gehr, R. D., Hackwell, J. A., and Smith, J. 1976, *Pub. A.S.P.*, **88**, 971.
- Gezari, D. Y., Foltz, W. C., Woods, L. A., and Woolridge, J. B. 1988, *Proc. SPIE*, **973**, 287.

- LeVan, P. D. 1989, in *Proc. of the Third IR Detector Technology Workshop*, ed. C. R. McCreight, NASA Technical Memo, No. 102209, p. 259.
- LeVan, P. D., and Sloan, G. 1987, *Proc. SPIE*, 819, 204.
- . 1989, *Pub. A.S.P.*, 101, 1140.
- LeVan, P. D., and Tandy, P. C. 1987, *Infrared Astronomy with Arrays*, ed. C. Wynn-Williams and E. E. Becklin (Hilo, HI: University of Hawaii), p. 411 (Paper 1).
- Olson, F. M., and Raimond, E. 1966, *Astr. Ap. Suppl.*, 65, 607 (LRS Atlas).
- Tresch-Fienberg, R., Fazio, G. G., Gezari, D. Y., Hoffmann, W. F., Lamb, G. M., Shu, P. K., and McCreight, C. R. 1987, *Ap. J.*, 312, 542.





**Appendix C**  
Confirmation of Emission Features near 13  $\mu\text{m}$  in Spectra of RX Bootis and S  
Draconis

Confirmation of Emission Features near 13  $\mu$ m in  
Spectra of RX Bootis and S Draconis

P.D. LeVan and P. Tandy (AFGL)

Using Gladys, a long slit 8-14  $\mu$ m spectrometer that employs a 58x62 pixel Si:Ga detector array, we are obtaining spectroscopy with the WIRO telescope of stars whose IRAS Low Resolution Spectra (LRS) show an emission feature near 13  $\mu$ m. We present a preliminary spectrum for one such star, and also for RX Boo, for which the comparison spectrum was extracted from the LRS database and provided to us by Martin Cohen. The spectra suggest peak feature emission shortward of 13  $\mu$ m for RX Boo and longward of 13  $\mu$ m for S Dra.

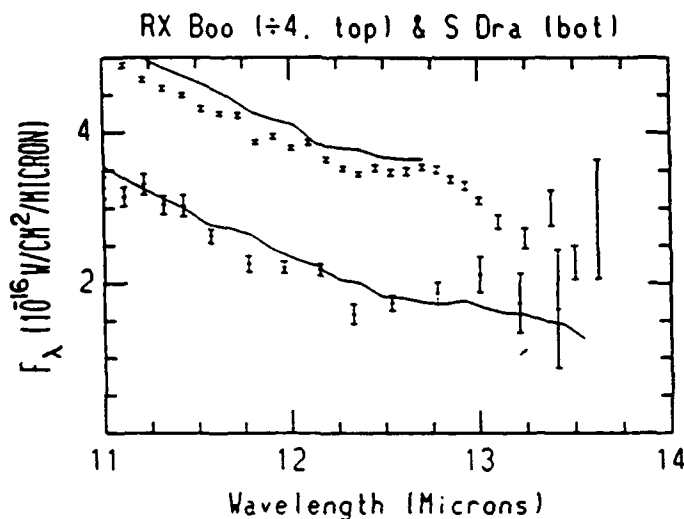


Figure. Spectra obtained with Gladys (shown with error bars) of RX Boo (in 1990 Mar) and S Dra (in 1990 July) compared with IRAS spectra (solid lines). The absolute LRS fluxes for S Dra were scaled upward by the factor 1.07.

**Appendix D**  
**Spatial Structure in the 10 Micron Spectrum of HD 44179 (The Red Rectangle)**

## SPATIAL STRUCTURE IN THE 10 MICRON SPECTRUM OF HD 44179 (THE RED RECTANGLE)<sup>1</sup>

G. L. GRASDALEN

G-Star Enterprises, 286 S. Pennsylvania, Denver, CO 80209

G. C. SLOAN

Department of Physics and Astronomy, University of Wyoming, Laramie, WY 82071

AND

P. D. LEVAN

Phillips Laboratory, Hanscom AFB, MA 01731

Received 1991 August 26; accepted 1991 October 10

### ABSTRACT

We present long-slit 10  $\mu\text{m}$  spectra of HD 44179. The object is resolved in the unidentified infrared features at 7.7, 8.6, and 11.3  $\mu\text{m}$ . Another feature at 12.8  $\mu\text{m}$ , which may be related to the unidentified infrared features or may be [Ne II], is similarly resolved. The source of the smooth underlying continuum is only marginally resolved by the present observations and analysis. These results demonstrate the power of long-slit spectra in revealing spatial structures via their spectral signature.

*Subject headings:* infrared: stars — stars: individual (HD 44179)

### 1. INTRODUCTION

Cohen et al. (1975) first associated the infrared source GL 915, discovered in the AFGL sky survey (Walker & Price 1975), with the bipolar nebula surrounding HD 44179. Due to its striking rectangular shape on the red Palomar Sky Survey plates, they named the object the Red Rectangle. The central star, HD 44179, has a spectral type of B9-A0 IIIe. The Na D and Ca II K lines are in emission, as well as a broad feature centered at 0.69  $\mu\text{m}$ . The optical nebulosity covers  $\sim 40''$ .

Zuckerman et al. (1976) postulated that HD 44179 is an evolved star, perhaps a proto-planetary nebula, based on its many similarities with the suspected proto-planetary nebulae GL 2688 (the Cygnus Egg; Ney et al. 1975; Crampton, Crowley, & Humphreys 1975) and GL 618 (the Westbrook Nebula; Westbrook et al. 1975). These similarities include the bipolar structure of the visible reflection nebulae and the strong thermal emission from the central regions at mid-infrared wavelengths. None of these objects are associated with any signs of star formation. Additional support for their evolved status comes from the carbon-rich nature of the heated dust and the high galactic latitude of these sources. All exhibit CO emission typical in outflows from evolved stars (Bachiller et al. 1988). The case for the proto-planetary nebula stage is strongest for GL 618, which has a variety of forbidden emission lines along with Balmer emission in its visible spectrum (Westbrook et al. 1975), indicating that UV radiation from the stellar core is beginning to ionize the surrounding material.

HD 44179 is unique among these objects in that its infrared spectrum contains the entire family of unidentified infrared (UIR) emission features at 3.3, 6.2, 7.7, 8.6, and 11.3  $\mu\text{m}$  (Russell, Soifer, & Willner 1978). A variety of materials have been invoked to explain these features, but none are completely adequate (see Sellgren 1990 for a recent review). These materials include polycyclic aromatic hydrocarbons (e.g., Léger & d'Hendecourt 1987), amorphous carbon material (Duley & Williams 1981), quenched carbonaceous composites

(Sakata et al. 1987) and hydrogenated amorphous carbon (Blanco, Bussoletti, & Colangeli 1988). These features have drawn much attention to HD 44179, primarily at 3.3  $\mu\text{m}$  (e.g., Tokunaga & Young 1980; Geballe et al. 1985; Tokunaga et al. 1988; Geballe et al. 1989).

Speckle interferometric methods have resolved the central thermal emission of HD 44179 into two sources at near-infrared wavelengths, a compact source 0".2 across and an extended source 1".0 N/S by 0".4 E/W (Dyck et al. 1984; Dainty et al. 1985; Leinert & Haas 1989). In a study of the UIR features, Geballe et al. (1989) detected 3.3  $\mu\text{m}$  UIR emission 5" north of HD 44179, indicating that the region producing this emission is very extended.

It is likely that the UIR features at longer wavelengths are also extended, so we chose to examine the spatial nature of the spectrum of HD 44179 at 10  $\mu\text{m}$  with a slit spectrometer. We have also observed  $\alpha$  Ori to serve as a check on our results, since the spatial extent of its emission at 10  $\mu\text{m}$  is fairly well understood (Dyck & Benson 1991).

### 2. OBSERVATIONS AND DATA REDUCTION

The data were obtained with the Geophysics Laboratory Array Detector Spectrometer (GLADYS) mounted on the University of Wyoming Infrared Observatory's (WIRO) 2.3 m telescope. GLADYS disperses radiation from 7 to 14  $\mu\text{m}$  onto a Si:Ga detector array with a NaCl prism; it is described in more detail by LeVan (1990). GLADYS was controlled by the WIRO computer system, which also collected the data and displayed it during the observations. In all spectra, the entrance slit was kept in a north/south orientation. The secondary mirror was chopped at a frequency of 1.5 Hz with a throw of 23" N/S.

Until recently the instrument was plagued by digital difficulties which resulted in repeatable but flawed data. These difficulties were finally overcome in late 1990, and GLADYS performed splendidly during the 1991 February run.

Since the original description of GLADYS a more sensitive array has been installed in the dewar. In the current configuration the same 10 columns of the chip are read 3 times during

<sup>1</sup> Wyoming Infrared Observatory Contribution, No. 133.

a cycle that formerly sampled 29 columns of the array. This procedure avoids the possibility of filling the wells with the larger currents produced by the more sensitive chip, but it also limits the extent of the slit to 9" on the sky. The new array was installed with the short-wavelength cutoff at 7  $\mu\text{m}$ .

A further innovation has been the implementation of three-beam chopping (Landau, Grasdalen, & Sloan 1992). This technique does not require repositioning the telescope during an integration, so it is far more appropriate for the present experiments, which require the highest possible spatial stability.

Flat fields for the array are obtained by saturating polystyrene foam with liquid nitrogen and then staring at it with GLADYS while it warms to ambient temperatures. As it warms, the flux on each pixel of the array increases. By taking the difference between the frames obtained at the highest and lowest flux levels we obtain very satisfactory flat fields. These flat fields have been verified by further staring observations of the night sky at different zenith distances and chopped observations of Jupiter.

After division by the flat field the data are spline-interpolated to remove the slight misalignments between the slit and dispersion axes and the chip axes. The slit and dispersion axes are physically independent; rotating the images will only remove one of these misalignments. This procedure carries a significant risk of degrading the data, but the effects we report in this *Letter* are well above any threshold for concern.

The last step in the basic data reduction is to correct for spectral transmission of the atmosphere and instrument. This is accomplished by obtaining observations of photometric, point source standard stars. Since columns in the interpolated data array now correspond to a single wavelength, the calibration merely consists of obtaining a spectrum by summing the observed intensities along each column. The flat-fielded images are then divided by spectra of  $\alpha$  Tau. Contour maps of the reduced data for  $\alpha$  Tau,  $\alpha$  Ori, and HD 44179 are shown in the left-hand panels of Figure 1.

### 3. ANALYSIS

Inspection of the contour maps displayed in Figure 1 leads one to suspect that  $\alpha$  Ori and HD 44179 show spatial structure in their spectra. To examine this possibility quantitatively, we fitted the spatial profile in each column (i.e., at each wavelength) with the following function:

$$I = I_n \left\{ \exp \left[ \frac{-(x_n - x)^2}{\sigma_n^2} \right] + 0.25 \exp (-0.65 |x_n - x|) \right\},$$

where  $I_n$  controls the central intensity in column  $n$ ,  $x_n$  is the interpolated central spatial position in column  $n$ , and  $\sigma_n$  is the spatial width for column  $n$ . Although we arrived at this form of the profile by empirically fitting the spatial profile we have found that the second term represents reasonably closely the wings of the diffraction profile predicted for the 2.3 m telescope over the 10  $\mu\text{m}$  window. Therefore this term in the profile function *does not* (to first order) scale with the spatial extent of the object.

We have tested this technique by applying it to the observations of  $\alpha$  Ori and  $\alpha$  Tau. In the right-hand panels of Figure 1 we have plotted the parameter  $\sigma$  obtained by fitting equation (1) to each column of the data. We refer to these plots as spatiograms.

First we discuss the behavior of  $\sigma$  with wavelength for  $\alpha$  Tau.

The gradual increase in  $\sigma$  beyond 10  $\mu\text{m}$  is expected on the basis of the increasing size of the diffraction pattern. The behavior shortward of 10  $\mu\text{m}$  is more difficult to analyze. Here the point spread function is most severely undersampled, so that our reduction techniques are less reliable. Further, the ozone absorption feature appears to play a major role in controlling the width and position of the spectrum, because of the changes in refractive index around this strong absorption feature. Similar comments apply to the region shortward of 8  $\mu\text{m}$ , a region of very strong atmospheric absorption.

The behavior of  $\sigma$  with wavelength for  $\alpha$  Ori is dramatically different. The excess width in the  $\alpha$  Ori spectrum clearly follows the infrared excess for this object, rising abruptly near 9  $\mu\text{m}$ , peaking at  $\sim 9.7 \mu\text{m}$  and falling gradually toward longer wavelengths. This is precisely the behavior that is expected based on the analysis of Dyck & Benson (1991). The present observations go somewhat further in that they clearly identify the spatial extent with the silicate feature. This expected result gives us considerable confidence in our method of analysis.

The HD 44179 data were taken from a 1 hour integration on 1991 February 10, divided into four groups, analyzed separately, and the results combined to form a mean and an estimate of the standard deviation. There are four peaks present in the spatiogram of HD 44179 that are not present in  $\alpha$  Tau. The three largest are centered at 7.7, 8.6, and 11.3  $\mu\text{m}$ , the classic UIR features in the 10  $\mu\text{m}$  region. The weakest and apparently narrowest peak occurs at 12.8  $\mu\text{m}$ . This feature may be related to the UIR feature at 11.3  $\mu\text{m}$  (Cohen, Tielens, & Allamandola 1985; Witteborn et al. 1989). From our observations, however, we cannot rule out the possibility that [Ne II] is responsible for the feature. There is marginal evidence that the underlying continuum in HD 44179 is also resolved. The observations of  $\alpha$  Tau were obtained immediately before and after the observations of HD 44179. The fact that the spatiogram for HD 44179 follows very closely the results for  $\alpha$  Tau in the regions outside of the spectral features means that the size of the central source is not a strong function of wavelength.

In Figure 2 we present the spectrophotometric data derived from our long-slit spectra of HD 44179. We have simply summed along each column to obtain the total flux from the source at each wavelength. The absolute flux levels were obtained by multiplying the reduced data by  $\alpha$  Tau's assumed spectrum, a 3800 K Planck blackbody function with a flux of  $18.5 \times 10^{-12} \text{ W m}^{-2} \mu\text{m}^{-1}$  at 10.00  $\mu\text{m}$ . Because of the narrow (2") slit used, our data are not truly photometric. From the comparison of spectra obtained of several photometric standards we assign an uncertainty of 15% to the overall level of the spectrum of HD 44179. In Figure 2 we have also plotted the *IRAS* LRS spectrum of HD 44179. Our data lie well below the LRS spectrum. What is particularly striking is the much lower contrast for the spectral features in our data. This is exactly the result we would expect; much of the emission from the spatially resolved features lies outside our slit.

### 4. DISCUSSION

The results in the previous section clearly demonstrate that at least two regions are producing the 10  $\mu\text{m}$  radiation from HD 44179. One region produces a nearly featureless continuum and is represented by the central source, which we may have marginally resolved. This region corresponds to the  $1''.0 \times 0''.4$  source and the compact  $0''.2$  source within it (Dyck et al. 1984; Dainty et al. 1985; Leinert & Haas 1989). The second region is much more extended than the central source and

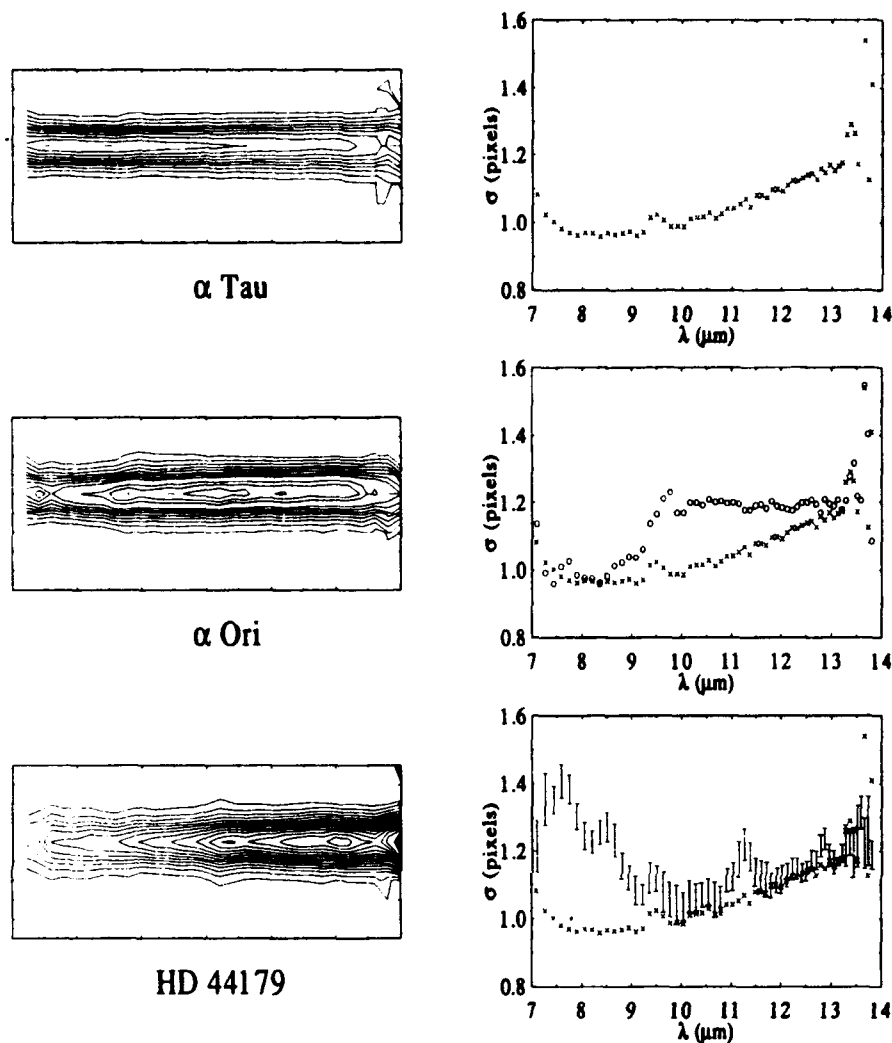


FIG. 1.—Spatial data for (from top to bottom)  $\alpha$  Tau,  $\alpha$  Ori, and HD 44179. On the left are contour plots of the reduced GLADYS images. Each tick on the vertical scale of the contour plot is 1 pixel ( $0''.9$ ); each tick on the horizontal axis is 5 pixels. Wavelength runs from  $7\ \mu\text{m}$  on the left to  $14\ \mu\text{m}$  on the right. The spatial extent (vertical axis) of the plots is  $9''$ . Spatiograms of these data are presented on the right. The spatiogram for  $\alpha$  Tau is repeated in the lower panels for reference. Each pixel is  $0''.88$  across. The increase in  $\sigma$  near  $9.5\ \mu\text{m}$  is due to the telluric ozone absorption feature.

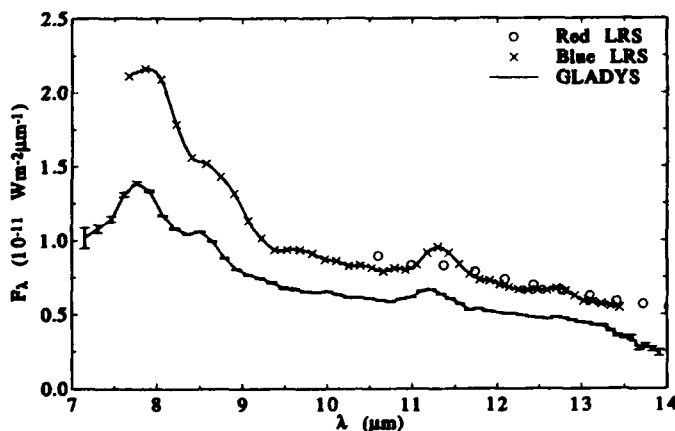


FIG. 2. The GLADYS spectrum of HD 44179, integrated across the slit. For comparison we have included the LRS spectrum.

produces the UIR features and the  $12.8\ \mu\text{m}$  feature. The full extent and exact nature of the extended emission cannot be obtained from the present analysis. The varying contrast between the central source and the extended emission will cause the numerical value of  $\sigma$  to vary from feature to feature even if the extended emission is distributed in precisely the same manner in each spectral feature. Our data do require that the emission features are extended by at least  $1''$ . This conclusion is supported by the detection of  $3.3\ \mu\text{m}$  UIR emission  $5''$  away from the  $10\ \mu\text{m}$  source by Geballe et al. (1989).

The central issue in the physical interpretation of our results is what causes the differences in emitted spectra between the two regions. Are they due to differences in the grains, such as their size distribution or chemical composition, or due to differences in the physical conditions in the two zones, such as density or radiation field? The most economical hypothesis at this time is that the grains are the same in both regions, but the fluorescent emission from the smaller grains is swamped in the

inner portions of the nebula by equilibrium emission from the larger grains.

We are presently analyzing similar observations of GL 618 and GL 2688 and will present a more quantitative discussion of all our data in a future paper.

As a technical aside we note that the  $12.8\ \mu\text{m}$  feature is not evident in the spectrum of HD 44179 (Fig. 2), whereas its presence is clearly indicated by the spatiogram (Fig. 1). The two-

dimensional character of a slit spectrometer is exploited here through a combination of spectral and spatial analysis.

We thank T. W. Edwards for helping to prepare GLADYS for the 1991 February observing run. We are also grateful to H. M. Dyck and R. Canterna for their engaging discussions. Astronomy at WIRO is supported by the State of Wyoming and the Air Force Office of Scientific Research.

#### REFERENCES

- Bachiller, R., Gómez-González, J., Bujarrabal, V., & Martin-Pintado, J. 1988, *A&A*, 196, L5
- Blanco, A., Bussoletti, E., & Colangeli, L. 1988, *ApJ*, 334, 875
- Cohen, M., et al. 1975, *ApJ*, 196, 179
- Cohen, M., Tielens, A. G. G. M., & Allamandola, L. J. 1985, *ApJ*, 299, L93
- Crampton, D., Crowley, A. P., & Humphreys, R. M. 1975, *ApJ*, 198, L135
- Dainty, J. C., Pipher, J. L., Lacasse, M. G., & Ridgway, S. T. 1985, *ApJ*, 293, 530
- Duley, W. W., & Williams, D. A. 1981, *MNRAS*, 196, 269
- Dyck, H. M., & Benson, J. A. 1991, A Study of the Angular Diameters of Dust Shells around Red Giants, AFOSR-TR-88-0057
- Dyck, H. M., Zuckerman, B., Leinert, Ch., & Beckwith, S. 1984, *ApJ*, 287, 801
- Geballe, T. R., Lacy, J. H., Persson, S. E., McGregor, P. J., & Soifer, B. T. 1985, *ApJ*, 292, 500
- Geballe, T. R., Tielens, A. G. G. M., Allamandola, L. J., Moorhouse, A., & Brand, P. W. J. L. 1989, *ApJ*, 341, 278
- Landau, R., Grasdalen, G., & Sloan, G. C. 1992, *A&A*, in press
- Léger, A., & d'Hendecourt, L. 1987, in *Polycyclic Aromatic Hydrocarbons and Astrophysics*, ed. A. Léger, L. d'Hendecourt, & N. Boccarda (Dordrecht: Reidel)
- Leinert, Ch., & Haas, M. 1989, *A&A*, 221, 110
- LeVan, P. D. 1990, *PASP*, 102, 190
- Ney, E. P., Merrill, K. M., Becklin, E. E., Neugebauer, G., & Wynn-Williams, C. G. 1975, *ApJ*, 198, L129
- Russell, R. W., Soifer, B. T., & Willner, S. P. 1978, *ApJ*, 220, 568
- Sakata, A., Wada, S., Onaka, T., & Tokunaga, A. T. 1987, *ApJ*, 320, L63
- Sellgren, K. 1990 in *Dusty Objects in the Universe*, ed. E. Bussoletti & A. A. Vittone (Dordrecht: Kluwer)
- Tokunaga, A. T., Nagata, T., Sellgren, K., Smith, R. G., Onaka, T., Nakada, Y., Sakata, A., & Wada, S. 1988, *ApJ*, 328, 709
- Tokunaga, A. T., & Young, E. T. 1980, *ApJ*, 237, L93
- Walker, R., & Price, S. D. 1975, *AFCRL Infrared Sky Survey*, AFCRL-TR-75-0373
- Westbrook, W. E., Becklin, E. E., Merrill, K. M., Neugebauer, G., Schmidt, M., Willner, S. P., & Wynn-Williams, C. G. 1975, *ApJ*, 202, 407
- Witteborn, F. C., Sandford, S. A., Bregman, J. D., Allamandola, L. J., Cohen, M., Wooden, D. H., & Graps, A. L. 1989, *ApJ*, 341, 270
- Zuckerman, B., Gilra, D. P., Turner, B. E., Morris, M., & Palmer, P. 1976, *ApJ*, 205, L15





**Appendix E**  
**Introduction to Spatially Resolved 10 Micron Spectra of Circumstellar**  
**Material around Evolved Stars**

## 1.1. Focus of this Dissertation

In the past, studies of the circumstellar dust emission from evolved stars have focused on either their spectroscopic or morphological properties. Long-slit spectroscopy provides the opportunity to examine the spatial and spectroscopic behavior of the emission from these objects simultaneously. Infrared emission from circumstellar material is often dominated by strong dust emission features, such as the silicate feature at  $9.7\ \mu\text{m}$  or the unidentified infrared (UIR) emission features. Determining the location of the emitting region and any variations in the spectroscopic character of these features with position would provide clues about the origin, nature, and evolution of circumstellar dust.

This dissertation focuses on observations of circumstellar material in two bright infrared sources,  $\alpha$  Orionis and HD 44179. The infrared spectrum of  $\alpha$  Ori contains a strong silicate emission feature, while HD 44179 exhibits the UIR features. Both are known to be extended on the scale of an arcsec or more. For this reason, it has been essential to develop new data analysis techniques for long-slit infrared spectroscopy in order to obtain the maximum possible spatial resolution from the data. This dissertation describes these new techniques, and the results of their application to observations of  $\alpha$  Ori and HD 44179.

Observations were made with the Geophysics Laboratory array detector spectrometer (GLADYS), an instrument uniquely suited to spatial studies of circumstellar dust emission. GLADYS covers the entire 10  $\mu\text{m}$  window from 7 to 14  $\mu\text{m}$  at a spectral resolution of 50-100 ( $\lambda/\Delta\lambda$ ). It is the only low-resolution long-slit spectrometer operating at 10  $\mu\text{m}$ . Its low spectral resolution is ideally suited to the broad dust features seen in the 10  $\mu\text{m}$  window. Its spatial resolution provides the opportunity of observing spatial variations in the spectral properties of these features.

I have chosen to write this dissertation not as a continuous narrative, but in chapters which will be published separately in the astronomical literature. The exception is this chapter, which provides a thorough description of GLADYS and our observing and reduction methods. It will not be published separately. Chapter 2 has already been published in *Astrophysical Journal (Letters)* (Grasdalen, Sloan, and LeVan 1992). It describes a technique of determining the spatial extent of an object as a function of wavelength and presents preliminary results of this technique for our observations of  $\alpha$  Ori and HD 44179. Chapter 3 describes the maximum entropy reconstruction technique developed specifically for long-slit spectroscopic images. Chapters 4 and 5 present results of maximum entropy reconstructions of  $\alpha$  Ori and HD 44179, respectively.

## 1.2. GLADYS

The Air Force Geophysics Laboratory 10  $\mu\text{m}$  array detector spectrometer (GLADYS) was designed to operate as a long-slit spectrometer over wavelengths from 7 to 14  $\mu\text{m}$ , specifically for use at the 2.3 m telescope at WIRO. Much of the following description is from LeVan and Tandy (1987) and LeVan (1990).

The optics in GLADYS collimate the  $f/27$  beam from the telescope at Cassegrain focus, pass it through a NaCl prism, and disperse it onto an array of Si:Ga detectors (Figures 1.1 and 1.2). The beam enters the dewar through a ZnSe window, which has a transmission of roughly 0.9. The coated NaCl prism has a transmission of 0.92. In all, there are seven Al mirrors coated with Ni, each with a reflectance of 0.95, giving the optics an overall transmission of 0.55. The collimator mirror has a focal length of 270 mm, the camera mirror, 75 mm; they re-image the  $f/27$  beam to  $f/7.5$  on the array. The effective resolution ( $\lambda/\Delta\lambda$ ) runs from 50 at 7  $\mu\text{m}$  to 100 at 14  $\mu\text{m}$ .

GLADYS uses a 58x62 Santa Barbara Research Corporation Si:Ga photoconductor array. It is bump-bonded to a CRC-228 Direct Read Out (DRO) multiplexor. The detectors are spaced 75  $\mu\text{m}$  apart, corresponding to

0.88 arcsec per pixel along the slit. The well-depth of each detector is only  $3 \times 10^6$  electrons, shallow enough to saturate the pixels if read too slowly.

To prevent pixel saturation, we read the array with an electronic co-adder which samples the pixels at a rate of 333 kHz. Every 3  $\mu$ sec, the co-adder directly addresses a pair of pixels on the array. A pair of analog-to-digital converter (ADC) circuits, labelled odd and even, then clamp and sample voltages across capacitors which collect electrons from the arrays and convert these to 12-bit numbers. The pixels are then reset, and the next odd-even pair is addressed. To read the entire array (3596 pixels, read as 1798 pairs) at this rate takes 5.4 msec. When operating, the co-adder samples and resets pixels continuously.

The co-adder drives the frequency at which the secondary mirror is chopped. By storing data from the source chop beam and reference beam ("plus" and "minus" positions, respectively) in separate memory locations and outputting the difference, the co-adder can remove the background flux from the signal in real time. At 10  $\mu$ m, the background can be thousands of times the signal from the astronomical source. While the co-adder memory can handle 20-bit numbers, the output lines are only 16-bit.

In 1989 December, we replaced the original array with a second one with approximately five times the sensitivity. To prevent the pixels on the more sensitive array from saturating, we modified the scheme used by the co-adder to address and read the pixels. The previous scheme involved reading 29 rows from the top half of the array and 29 from the bottom in one scan. We now read only 10 rows from the top and bottom, but they are read three times in each scan cycle, resulting in a read rate three times as fast. The 10 rows on the top and bottom halves are not contiguous; we usually only save data from the 10 bottom rows. The co-adder stores the three reads each cycle in separate memory addresses as a  $30 \times 62$  matrix. While this scheme cuts the exposure time for an individual pixel from 5.4 to 1.8 msec, it also reduces the spatial extent of the array from 58 to 10 rows (8.8 arcsec).

The co-adder has a number of degrees of freedom. The *chop count* sets the number of chops per integration. Usually, this number is kept at eight; for bright sources, it must be set at lower values to prevent the 16-bit output bus from overflowing. By setting the *frame number*, the number of times the array is read per chop can be controlled. Effectively, this sets the chop frequency, since the co-adder reads the array at a constant rate of 333 Hz. The *chop delay* allows the operator to ignore a certain number of frames read from the array while the secondary mirror is settling into position. The operator can also choose between *co-add* or *single-frame* mode. When the co-

adder is in *single-frame* mode, it will only output the last frame read from the array instead of co-adding all the frames read during an integration. Another switch allows a choice between *direct-output* or *chop-difference* output. Depending on the setting, the co-adder will either output the difference between plus and minus memories, or just output the values in plus memory. Finally, the co-adder can be set to output the 16 least significant bits (LSB) in its 20-bit memory or the 16 most significant bits (MSB). This setting is particularly handy when the co-adder is not in chop-difference mode, as the numbers involved can get quite large.

Typically, the co-adder is set to chop at 1.5 Hz, with chop count set to 8 chops per integration and the chop delay set so that the array is read 58 times in each chop position. When observing an astronomical source, the co-adder should be set to chop-difference, co-add mode, outputting the 16 LSBs.

### 1.3. Data Acquisition Software

All observations were made with a Masscomp 5500 computer controlling both the 2.3 m telescope at WIRO and the electronic co-adder for GLADYS, using data acquisition software which I developed specifically to drive GLADYS from the Masscomp. Prior to the development of this software, a Digital Equipment Corporation PDP-11 had been used to control

GLADYS. That configuration was only developmental, and it had a number of shortcomings; the most significant was the lack of any real-time display, which made it extremely difficult to locate an object in the beam, to peak up on it, or to focus. A second problem with the old configuration was that it did no software co-adding. As a result, each individual frame read from the co-adder was stored to hard disk, requiring tremendous amounts of storage space.

I developed the data acquisition software with these two problems in mind. When the co-adder has completed a single integration, one frame of data is collected by addressing the co-adder one memory location at a time. The software can save up to 40 frames as one image. After each frame is obtained, the software updates the mean and uncertainty of the mean of each pixel. The software determines the uncertainty of the mean to partially offset the loss of statistical information involved in averaging 40 frames of data into one image. As data are obtained, a color display allows the operator to see the results in real time.

An additional improvement is a median filter routine designed to remove spikes in the data. When median filtering, the software keeps track of the values read for each pixel in each frame. The filter can be set to remove any number of extreme values in the distribution for each pixel.



Data images are stored as 2×30×62 FITS files on the Masscomp hard disk. FITS is the Flexible Image Transport System, a standard format for storing astronomical data (Wells, Greisen, and Harten 1981). The three-dimensional format is necessary since both the mean and uncertainty of each pixel are stored in each image. The two arrays stored in a single image are known as the signal and noise bands, respectively. A typical image, consisting of 40 frames at a chop count of 8 chops per frame with a chop frequency of 1.5 Hz, comprises 55,680 individual array reads in each of the plus and minus chop positions. Such an image takes 3 minutes of integration time, and occupies 31.7 kilobytes of disk space.

#### **1.4. Observing Methods**

The sky emission at wavelengths of 10  $\mu\text{m}$  can vary substantially from one position and time to the next. The traditional means of correcting for these variations is to chop with the star in the plus beam (telescope position A) and then nod the telescope so the star moves to the minus beam (position B). By taking data with the telescope position following the sequence A-B-B-A, both spatial and temporal linear gradients in the sky emission can be removed. At WIRO, re-positioning the telescope can result in positional errors from one nod position to the next of a significant fraction of an arcsec.

Although these errors are much smaller than for many telescopes, they are a serious problem if high spatial resolution is desired.

We have chosen instead to implement the 3-beam chop method of Landau, Grasdalen, and Sloan (1992). In this scheme, the minus beam position alternates from one side of the star to the other, thus correcting for any variations in emission over much shorter time-scales than the chop-and-nod scheme. Some astronomers have criticized the 3-beam chop method because it does not completely remove the telescope background, as the chop-and-nod scheme does. However, if the emissivity of the telescope is linear, then it will cancel in the 3-beam chop method. Experiments by Landau, Grasdalen, and Sloan (1992) demonstrate that the variations in the emissivity of the 2.3 m telescope at WIRO as a function of secondary mirror position are very close to linear at 10  $\mu\text{m}$ . The non-linear terms have a larger contribution than the linear term only for chop throws of more than 80 arcsec, but our throw is typically only 20-25 arcsec. Because the telescope never moves, the positional problems inherent in the chop-and-nod scheme are not an issue. This improvement gives GLADYS its best possible spatial resolution. The 3-beam method offers an additional advantage: by alternating the position of the source in the plus and minus beams, the strong fixed pattern on the array can be canceled in real time, allowing the observer to use the real-time image display to hunt for and peak up on faint objects.

## 1.5. Data Processing

During each read cycle, the co-adder addresses the  $10 \times 62$  pixel active area of the array three times. The data acquisition software treats the output from the co-adder as 30 distinct rows. The first task when processing data is to convert the  $30 \times 62$  format to a  $10 \times 62$  format, by averaging the three sets of 10 rows together and re-calculating the uncertainty in the mean.

One of the difficulties with GLADYS is a timing difference between the odd and even array addresses. Sometimes these get switched, requiring a re-meshing scheme to return the pixels to their proper order. Spotting these meshing problems is easy, because the data assume a strongly corrugated nature when the meshing is incorrect.

We produce a flat-field array for GLADYS by integrating with foam cooled to liquid-nitrogen temperatures in the beam. We stare at the foam with the co-adder in single-frame, direct-output mode. By subtracting an image of cold foam from one of warm foam, we can remove the dark current and radiation from the ZnSe window from the data. The resulting difference contains the slopes of the response functions of each pixel on the array and can be used to flat-field our data images. We have found that the flat-field

characteristics of our array are very stable from one observing run to the next.

Our flat-field images are contaminated by strong spectral information, which depends on the temperature of the foam (in both the warm and dark images) and the transmission of the dewar optics. This problem is removed from the data when we calibrate spectra extracted from our images. We observe spectroscopic standards to correct our program data for atmospheric and instrumental transmission, which is a strong function of wavelength at 10  $\mu\text{m}$ . If we flat-field a spectroscopic standard in the same manner as a program source, when we divide our program spectrum by our standard spectrum, the spectral characteristics of our flat field cancel out along with the transmission of the atmosphere and instrument. If we know the nature of our standard spectrum, we can multiply this back in, producing a fully corrected and calibrated spectrum of our program source. Figure 1.3 illustrates the transmission of the atmosphere and instrument as determined from observations of  $\alpha$  Tau. We assumed that  $\alpha$  Tau can be represented in  $F_\nu$  units by a  $\lambda^{-2}$  Rayleigh-Jeans distribution.

## 1.6. Problems

When GLADYS was designed and built, no long-slit spectrometers were

operational at 10  $\mu\text{m}$ . GLADYS is a result of pioneering effort and represents a new class of astronomical instrument. It is not surprising that it suffers from a number of difficulties, some minor and some serious. Tracking these down and repairing them were a major effort.

First, the instrument is not background limited. If the instrument were truly dominated by photon noise, then the typical pixel-to-pixel noise should be about 1.6 analog-digital units (ADU). Instead, the noise is more on the order of 10 ADU; it appears to be dominated by what is probably read-noise. The limiting magnitude for GLADYS is roughly +2.0 at 10  $\mu\text{m}$ ; spectra as faint as +1.6 at 10  $\mu\text{m}$  have been published (LeVan et al. 1992).

The second problem is more severe. The co-adder at times has failed to properly co-add frames read from the array. The problem manifests itself as glitches in output data which are small enough to be difficult to detect at the observatory, but significant enough to seriously degrade the quality of the data. In 1990 October, when I observed Mars and Jupiter to diagnose the problem, I discovered its nature. Because Mars was so bright, I had to observe it in single-frame mode, while I observed Jupiter in co-add mode. After flat-fielding the respective sets of data, it was apparent that the Mars data were excellent, but the Jupiter data were plagued by glitches (Figure

1.4). In general, the co-adder glitching is only apparent in data which have been flat-fielded.

Further diagnostic work in 1990 November and December revealed that the co-adder was corrupting data from the array. I used a breadboard to input known signals into the plus and minus chop memories. Most frames from the co-adder consisted of correct values, but occasionally, a frame from the co-adder would contain values smaller than the expected result. The odd and even channels behaved differently when the co-adder failed, and the error was very roughly proportional to the input signals.

By replacing two boards in the co-adder electronics with updated versions, we eliminated the problem in 1990 December, but by 1991 June, a similar problem had apparently arisen. The observations examined in this dissertation were taken in 1991 February, when the co-adder was operating properly. I tested this by carefully examining new observations of Jupiter and spectra of bright sources for glitches in the data similar to those illustrated in Figure 1.4 and also by comparing flat-field data taken in single-frame and co-add mode.

A third problem with GLADYS is a slight misalignment of the optical axes. Optimally, the array would be aligned so that one axis, the

spectroscopic axis, would be perfectly aligned with the dispersion axis of the prism. The second axis on the array, the spatial axis, would be aligned with a line of constant wavelength. Unfortunately, the dispersion axis is slightly tilted to the spectroscopic axis of the array, shifting 0.8 pixels across the 62-pixel spectroscopic axis. Also, lines of constant wavelength are not orthogonal to the dispersion axis or either axis of the array. They shift 1.2 pixels across the 10-pixel spatial axis. We could eliminate only one of the two non-orthogonalities by performing a rotational transformation on our data. These misalignments are difficult to avoid and significantly complicate data reduction.

These problems emphasize the difficulty of producing a long-slit spectroscopic system at 10  $\mu\text{m}$ . While they have complicated the processes of acquiring and analyzing data, this dissertation illustrates the power of an instrument like GLADYS once these problems have been overcome.

## References

Grasdalen, G.L., Sloan, G.C., & LeVan, P.D., 1992, *ApJ* **384**, L25.

Landau, R., Grasdalen, G., & Sloan, G.C., 1992, *A&A*, in press.

LeVan, P.D., 1990, *PASP* **102**, 190.

LeVan, P.D., Sloan, G.C., Little-Marenin, I.R., & Grasdalen, G.L., 1992, *ApJ*, in press.

LeVan, P.D., & Tandy, P.C., 1987, in *Infrared Astronomy with Arrays*, ed. C.G. Wynn-Williams & E.E. Becklin (Honolulu: Univ. of Hawaii Institute for Astronomy), 411.

Wells, D.C., Greisen, E.W., & Harten, R.H., 1981, *A&A Suppl.* **44**, 363.



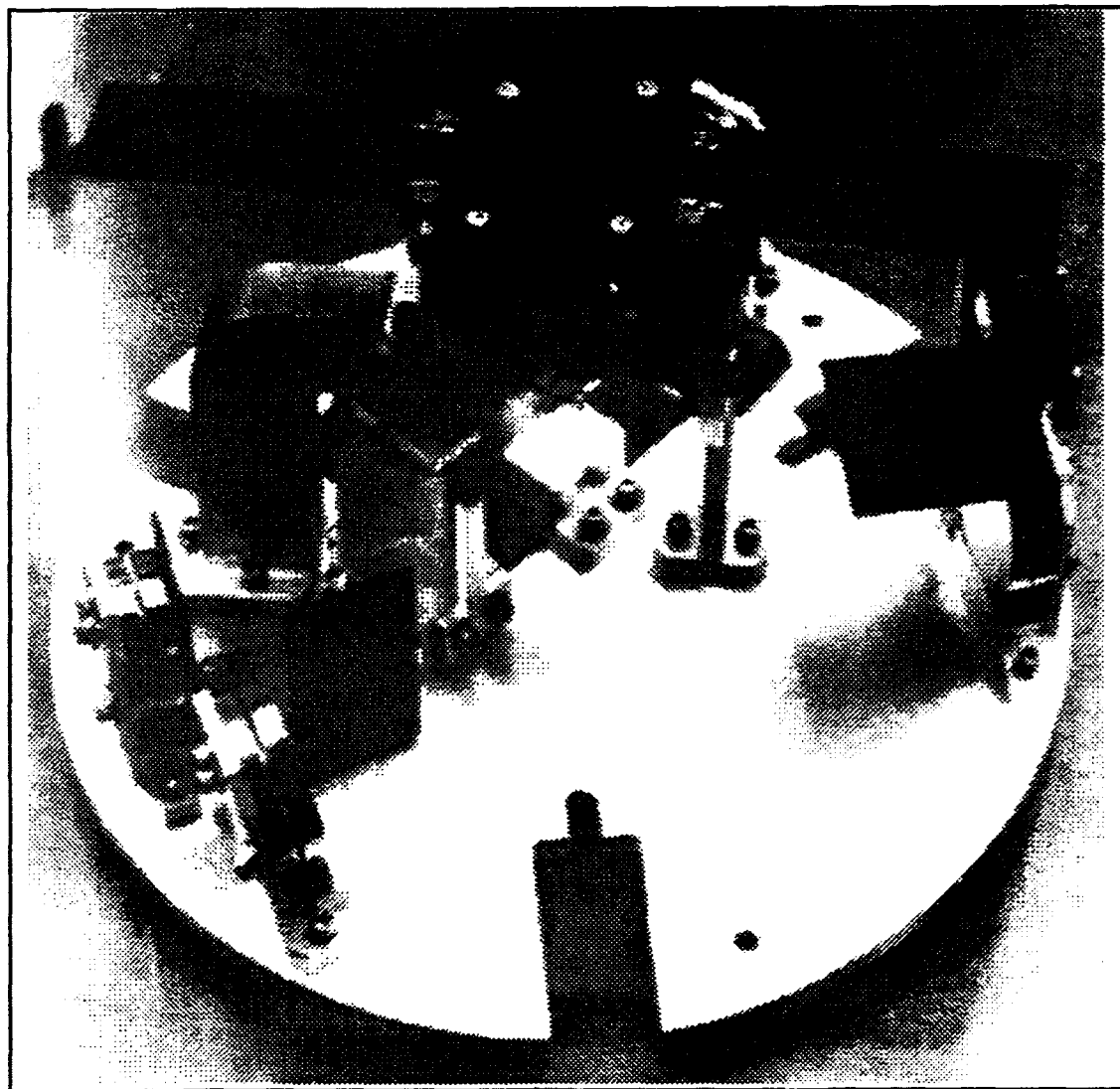


Figure 1.1. The spectrometer optical bench, showing the entrance slit, five of the seven mirrors, and the NaCl prism (just left of center). The array is located behind the slit in this figure.

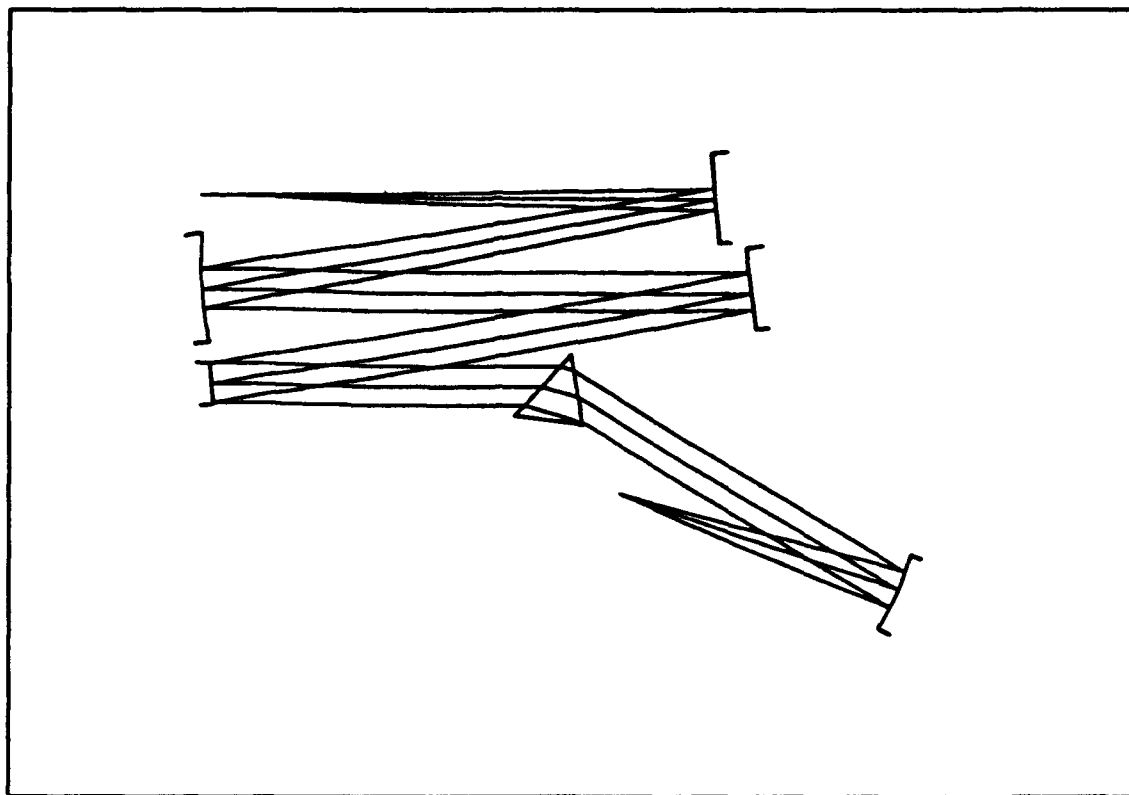


Figure 1.2. Ray trace at 11  $\mu\text{m}$  of the spectrometer optical bench. Two out-of-plane mirrors are not shown.

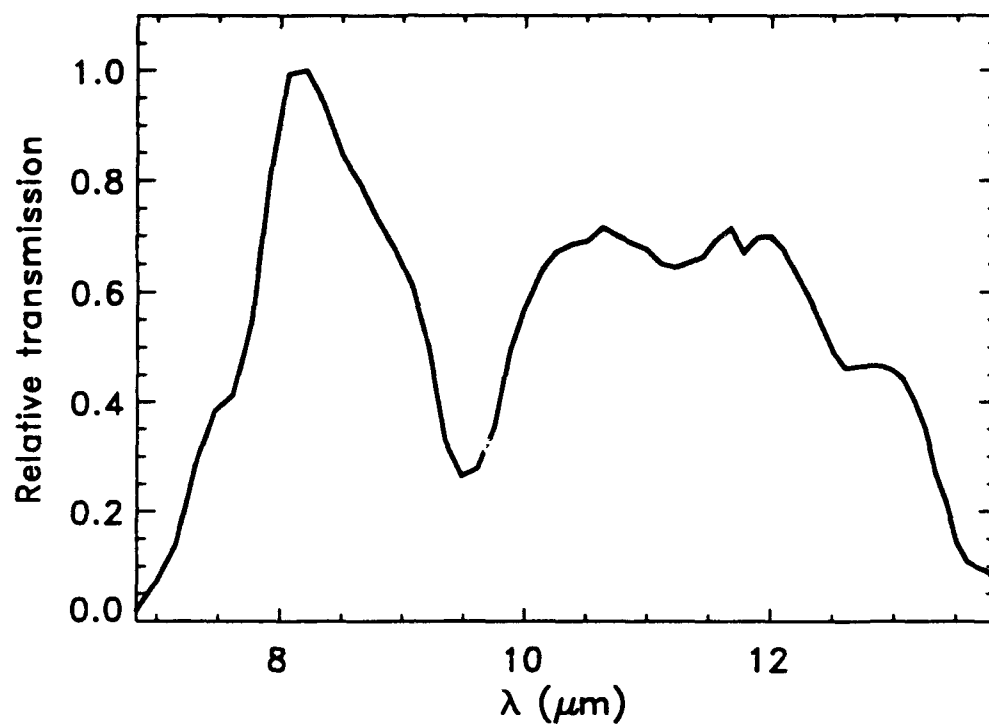


Figure 1.3. Atmospheric and instrumental transmission in the 10  $\mu\text{m}$  band as a function of wavelength, based on observations of  $\alpha$  Tau with GLADYS and the assumption that it can be modeled with a Rayleigh-Jeans distribution ( $F_{\nu} \propto \lambda^{-2}$ ).

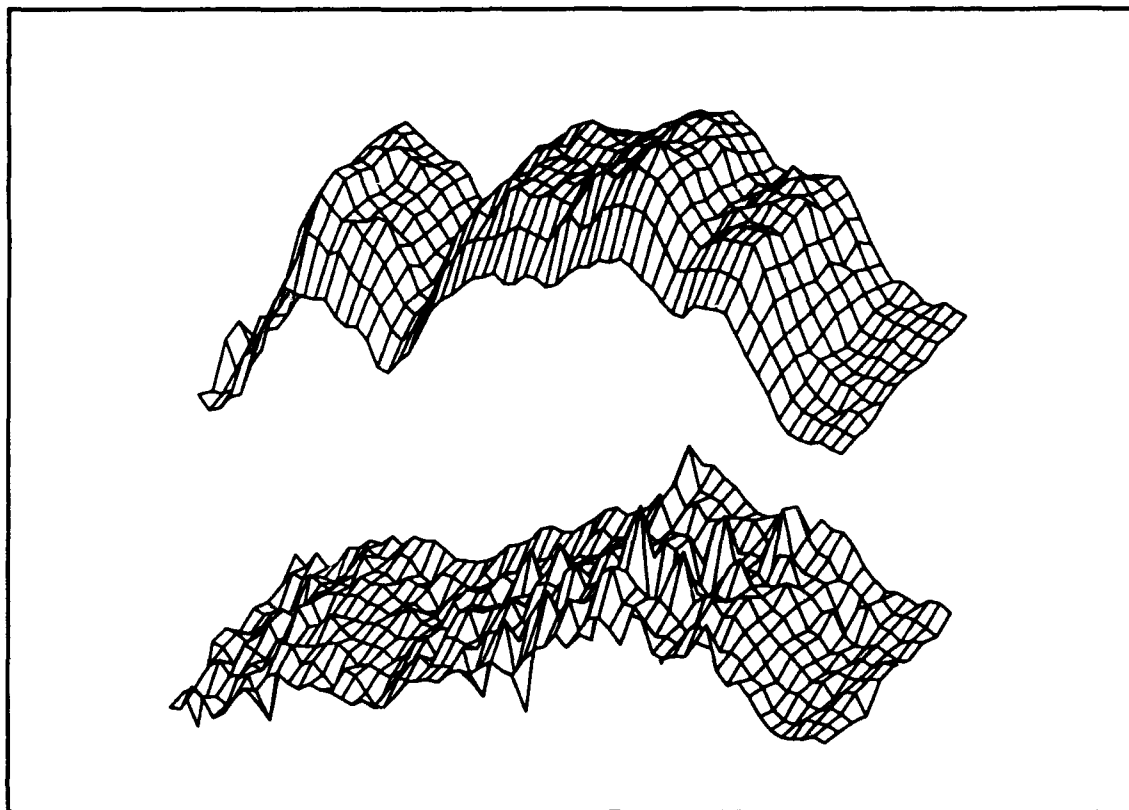


Figure 1.4. Surface plots of Mars (top) and Jupiter (bottom), illustrating the effects of co-adder glitching in 1990 October. Both images have been flat-fielded. Wavelength runs from 7  $\mu\text{m}$  on the left to 14  $\mu\text{m}$  on the right. The other direction is position along the slit. The Mars data were taken in single-frame mode and thus do not suffer from the co-adding errors that afflict the Jupiter data.

**Appendix F**  
**8—14 Micron Spectroscopy of Carbon Stars Associated with Silicate Dust**

## 8-14 MICRON SPECTROSCOPY OF CARBON STARS ASSOCIATED WITH SILICATE DUST<sup>1</sup>

PAUL D. LEVAN

Phillips Laboratory, Hanscom AFB, MA 01731

G. C. SLOAN

Physics and Astronomy Department, University of Wyoming, Laramie, WY 82071

IRENE R. LITTLE-MARENIN<sup>2</sup>

CASA, Campus Box 391, University of Colorado, Boulder, CO 80309-0391

AND

G. L. GRASDALEN

G-star Enterprises, 286 South Pennsylvania, Denver, CO 80209

Received 1991 November 21; accepted 1991 December 27

### ABSTRACT

We obtained 8-14  $\mu\text{m}$  spectra of two known and two proposed silicate carbon stars. Our data confirm the positional association of BM Gem and V778 Cyg with the *IRAS* Low Resolution Spectrometer silicate spectra. Moderate silicate emission has been discovered in the carbon star HD 189605. HD 100764, on the other hand, has no significant silicate emission.

*Subject headings:* circumstellar matter — dust, extinction — infrared: stars — stars: carbon

### 1. INTRODUCTION

One of the most unusual types of objects discovered as a result of *IRAS* is the class of silicate carbon stars. These stars were first recognized by Little-Marenin (1986) and Willems & de Jong (1986). Lloyd Evans (1990), in a careful study, found that a total of seven objects are classified optically as carbon stars and yet, inexplicably, have strong silicate features at 10 and 18  $\mu\text{m}$ .

Lloyd Evans (1990) and Lambert, Hinkle, & Smith (1990), following the suggestion of Willems & de Jong (1986), confirmed that all seven silicate carbon stars have a high  $^{13}\text{C}/^{12}\text{C}$  ratio relative to most carbon stars and are thus classified as J-type carbon stars. In addition, all have very red *IRAS* [12] – [25] colors. Strong silicate emission as seen by the *IRAS* Low Resolution Spectrometer (LRS), and low *IRAS* variability.

Radio observations demonstrate that the circumstellar gas is also oxygen-rich. Water masers have been detected in three of the silicate carbon stars and OH masers in two (Benson & Little-Marenin 1987; Nakada et al. 1987; Deguchi et al. 1988; Little-Marenin, Benson, & Dickinson 1988; Deguchi, Nakada, & Foster 1989; te Lintel Hekkert 1990).

Lloyd Evans (1990) suggested four additional candidates for the class, based primarily on their [12] – [25] colors. We observed two of the seven silicate carbon stars to verify their LRS spectra and two of the four candidates to determine if they were members of this class. Details for these stars are given in Table 1.

### 2. OBSERVATIONS

We obtained spectra of BM Gem, V778 Cyg, HD 189605 (CCS 2837), and HD 100764 (CCS 1886) with the Geophysics Laboratory Array Detector Spectrometer (GLADYS) mounted at the Cassegrain focus of the 2.3 m telescope of the

Wyoming Infrared Observatory (WIRO). GLADYS is a long-slit prism spectrometer which focuses radiation from 7 to 14  $\mu\text{m}$  onto a  $58 \times 62$  array of Si : Ga photoconductors.

Details of the spectrometer are discussed by LeVan (1990), but several modifications have been made. An improved radiation baffle was mounted inside the Dewar, and it dramatically reduced the extraneous background radiation on the array. We also installed a higher sensitivity array. In order to read the array fast enough to prevent saturation, we only read 10 of the 58 available rows, reducing the spatial extent of our data from  $52''$  to  $9''$ . Also, modifications to the electronic co-adder eliminated low-level digital glitching that affected observations made prior to 1991 February (LeVan 1991). The glitches had a significant impact on the data, and as a result, all observations made prior to 1991 February must be treated cautiously.

Observing details are given in Table 2. For most of the observations, we used three-beam chopping to remove the background flux and correct for any linear spatial and temporal gradients (Landau, Grasdalen, & Sloan 1991). We peaked on the infrared signal of BM Gem and V778 Cyg prior to integrating. The relative infrared faintness of HD 100764 and HD 189605 prevented us from peaking on the sources before integrating; we checked the alignment of the infrared and optical beams on nearby bright sources and then integrated with the telescope crosshairs centered on the optical star.

### 3. REDUCTION OF SPECTRA

We first corrected the body of data by dividing it by a two-dimensional flat field, which was generated by taking the difference between an image of foam at room temperature and foam cooled to liquid nitrogen temperature. The consistency of flat fields obtained in this manner gives us great confidence in the stability of the photometric response of the array over the lifetime of GLADYS.

One-dimensional spectra were obtained from the two-dimensional images using the optimal extraction method discussed by Marsh (1989) and references therein. A spatial point-spread function (PSF) derived from the spectra was used

<sup>1</sup> Contribution 134 of the Wyoming Infrared Observatory.

<sup>2</sup> Also Whitin Observatory, Wellesley College.

TABLE 1  
CHARACTERISTICS OF OBSERVED STARS

Star	IRAS Name	CCS	$\alpha$ (1950)	$\delta$ (1950)	Optical Spectral Type	LRS Type	$F_{12}$ (Jy)	[12] - [25] (mag)	Variability <sup>a</sup>
BM Gem .....	07179 + 2505	716	07 <sup>h</sup> 17 <sup>m</sup> 55 <sup>s</sup> .9	+25°05'37"	C5, 4J	29	34.9	0.93	0%
HD 100764 .....	11331 - 1418	1886	11 33 10.8	-14 19 00	C1, 1	—	7.8	1.85	0
HD 189605 .....	19583 - 0730	2387	19 58 23.2	-07 30 15	C5, 5	—	6.5	1.66	20
V778 Cyg .....	20350 + 5954	2919	20 35 03.6	+59 54 57	C4, 5J	29	29.9	1.00	30

<sup>a</sup> Probability of infrared variability from the IRAS Point Source Catalog.

for the extractions. The pixel signals were weighted by the inverse of the variances squared.

We divided the resulting spectra by observed spectra of standard stars. This procedure corrects for the variation with wavelength of the instrumental response and instrumental and atmospheric transparency. We then multiplied this ratio spectrum by an assumed model for the spectrum of the standard star. The models used were blackbodies at the effective temperatures of the stars, normalized to assumed values for their flux at 11  $\mu$ m. Corrections made at high air mass (for HD 100764 and HD 189605) were validated by the favorable comparison with the IRAS LRS results of our reduced spectra for R Crt and RR Aql, also taken at high air mass.

Based on comparisons of program stars observed on separate nights, we estimate the uncertainty in the absolute flux levels to be about 10% for stars observed under good seeing conditions. These uncertainties may exceed 15% for HD 100764 and HD 189605 since they were observed under poorer seeing conditions at higher air masses. Since our slit width is at best only twice the image diameter, this level of precision is excellent.

#### 4. ANALYSIS

##### 4.1. Positions

We found that the peak infrared flux for BM Gem lay within 1" of the optical carbon star. The possibility allowed by the IRAS positional uncertainty ellipse, that a star other than BM Gem might be the source of the silicate emission flux, now appears very unlikely. In the case of V778 Cyg, peak infrared emission was detected approximately 1" northwest of the optical image, corresponding to the maximum positional uncertainty due to flexure. Deguchi et al. (1988) determined that the position of a water maser source coincided with the photographic position of V778 Cyg to within 0".5.

##### 4.2. Spectral Characteristics

We compare our spectra of BM Gem and V778 Cyg

TABLE 2  
OBSERVATIONS

Star	Dates (UT)	Slit Width	Background Removal Method	$F_{10.0}$ (Jy)
BM Gem .....	1989 Dec 21	3"	Chop and nod	64 $\pm$ 9
	1991 Feb 6	2	Three-beam	43 $\pm$ 5
HD 100764 .....	1991 Feb 6, 7, 8	2	Three-beam	6 $\pm$ 2
HD 189605 .....	1990 Jul 10, 11	2	Three-beam	11 $\pm$ 2
V778 Cyg .....	1990 Jul 11	2	Three-beam	58 $\pm$ 8
	1990 Sep 2	2	Three-beam	52 $\pm$ 7
	1991 Feb 6, 10	2	Three-beam	48 $\pm$ 7

obtained in 1991 February with the IRAS LRS spectra in Figure 1. The LRS spectra were scaled by 0.78 and 1.2, respectively, to match our spectra. The feature shape and contrast have not changed significantly. The similarity of our spectra with the LRS results demonstrate that the sources of the silicate emission must be coincident with, or very close to, the optical carbon stars.

Figure 2 contains our spectra of HD 100764 and HD 189605. While these spectra are noisy, inspection leads us to suspect that HD 189605 contains a weak silicate emission feature, while HD 100764 does not. In addition, the underlying continua in the spectra of these two stars appear to be much redder than in V778 Cyg and BM Gem.

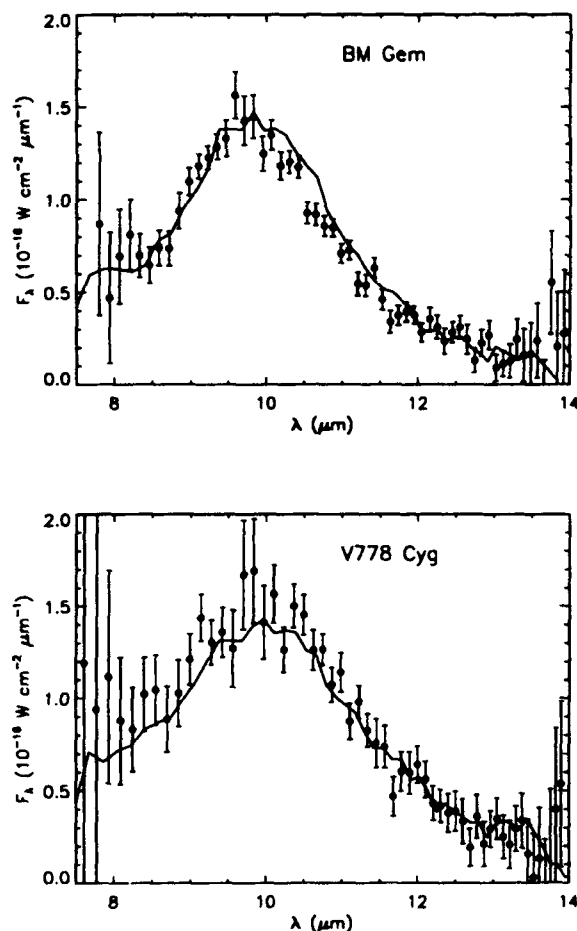


FIG. 1.—GLADYS (error bars) and LRS (solid line) spectra of the silicate carbon stars, BM Gem and V778 Cyg. We have multiplied the LRS spectrum of BM Gem by 0.78 and that of V778 Cyg by 1.2.

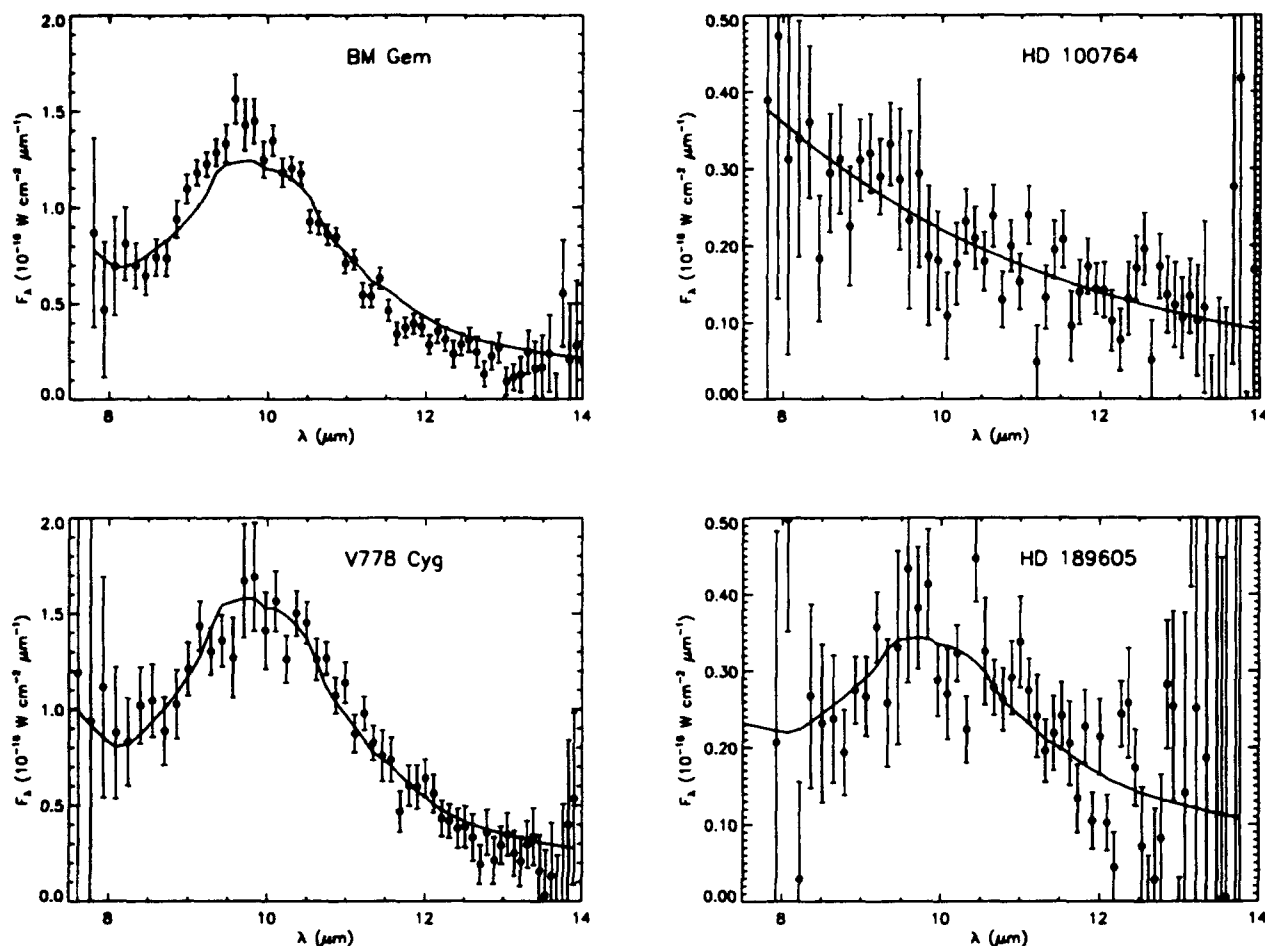


FIG. 2.—GLADYS spectra of our four program stars with the results of our model spectra superposed

To evaluate these possibilities quantitatively, we have fitted each spectrum with a model consisting of a silicate emission profile added to a blackbody continuum. The silicate profile was extracted from the LRS spectrum of  $\mu$  Cep by fitting a 3500 K blackbody to the 8  $\mu$ m continuum and subtracting it out. The silicate emission profile of Draine & Lee (1984) simply did not match our spectra, and the profile from a bright source, GL 811, selected from the LRS class with the strongest silicate feature to continuum contrast (class 29), was also unsatisfactory. The silicate profile derived from the spectrum of  $\mu$  Cep provided the best fit to our spectra.

We chose as the best model spectrum that which minimized the sum of the squares of the weighted residuals, or  $\chi^2$ . These are presented in Figure 2 as solid lines through the data. We fixed the total flux at 10  $\mu$ m and varied the inverse temperature and the silicate feature contrast (the ratio of silicate to blackbody flux at 10  $\mu$ m). The best values are given in Figure 3 as filled circles for each spectrum. The contours around the circles are lines of constant  $\chi^2$  chosen so that the actual values of the parameters have a 67% chance of lying within.

Our data and spectral models verify the *IRAS* LRS spectra for both BM Gem and V778 Cyg; their 10  $\mu$ m spectra are dominated by very strong silicate emission. We find the silicate contrasts to be 3.4 and 4.0, respectively. The relatively high fit temperatures indicate that the best model continua follow, or nearly follow, the Rayleigh-Jeans approximation in this wave-

length regime. We also note that the silicate feature extracted from  $\mu$  Cep fits the spectrum of V778 Cyg better than BM Gem. The systematic differences in the spectrum of BM Gem

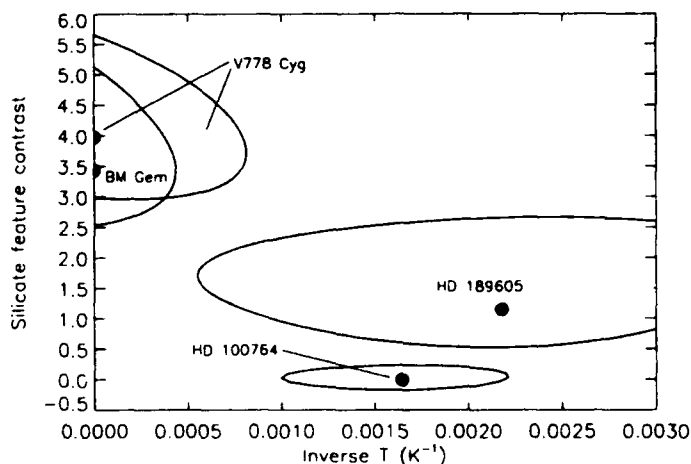


FIG. 3.—Comparison of parameters derived from our fitted models. The contours are lines of constant  $\chi^2$ . The levels have been chosen so that the contours enclose the area of 67% confidence. The filled circles mark the positions of minimum  $\chi^2$ .



indicate that it may possess a dust shell with a different temperature or composition.

The best model fit to HD 100764 includes no silicate emission; the upper limit to the silicate feature contrast is only 0.2. On the other hand, HD 189605 is associated with silicate emission as predicted by Lloyd Evans (1990). The contour for HD 189605 in Figure 3 encloses the largest area because we obtained its spectrum in 1990 July, before GLADYS had been repaired to eliminate the electronic glitching. While this spectrum is of a lower quality than the others, we believe the error ellipse accurately reflects the uncertainty of the model fit. The lower limit to its silicate contrast is 0.5. Both HD 100764 and HD 189605 have unusually low continuum temperatures of about 500 K, a result consistent with their red [12]–[25] colors.

### 5. DISCUSSION

HD 100764 was listed by Lloyd Evans (1990) as a possible source of silicate emission because of its red *IRAS* [12]–[25] color and its large  $^{13}\text{C}/^{12}\text{C}$  ratio (Dominy 1985). We have determined that it is not a silicate emitter. This result may be related to its unusual classification of C1,1; silicate carbon stars typically are classed from C4,4 to C5,5.

We have discovered that *HD 189605 is another silicate*

*carbon star*. This finding is significant because this star has some characteristics which distinguish it from the other members of this class. Only HD 189605 is not a J star. Lloyd Evans (1990) found no strong enhancement of  $^{13}\text{C}$ , although he did detect weak Ba II and Sr I lines, a characteristic sometimes associated with J stars. Another important difference is the spectrum at 10  $\mu\text{m}$ . The continuum is cooler and the silicate feature contrast lower than in other silicate carbon stars. The cool continuum in HD 189605 must arise in the shell and could be diluting the silicate emission. The continuum most likely is due to a component chemically different than the silicate grains, possibly graphite.

We would like to thank the staff of WIRO Observatory for making these observations possible; T. W. Edwards was especially helpful in diagnosing the electronics problems with GLADYS. We acknowledge Steve Little for a critical reading of the manuscript and Peter Tandy for engineering assistance during the observing runs. We found the LRS data base at the University of Colorado at Boulder extremely helpful in our reductions. Astronomy at the University of Wyoming is supported by the State of Wyoming and the US Air Force. This work is in part supported by NSF grant RII-90028960 under the VPW program (IR-ML).

### REFERENCES

- Benson, P. J., & Little-Marenin, I. R. 1987, *ApJ*, 316, L37  
 Deguchi, S., Kawabe, R., Ukita, N., Nakada, Y., Onaka, T., Izumiura, H., & Okamura, S. 1988, *ApJ*, 325, 795  
 Deguchi, S., Nakada, Y., & Foster, J. R. 1989, *MNRAS*, 239, 825  
 Dominy, J. F. 1985, *PASP* 97, 1104  
 Draine, B. T., & Lee, H. M., 1984, *ApJ*, 285, 89  
 Lambert, D. L., Hinkle, K. H., & Smith, V. V. 1990, *AJ*, 99, 1612  
 Landau, R., Grasdalén, G., & Sloan, G. C. 1992, *A&A*, in press  
 LeVan, P. D. 1990, *PASP*, 102, 190  
 LeVan, P. D. 1991, in *Proc. of the 1991 North American Workshop on Infrared Spectroscopy*, ed. R. Stencel (Laramie, Wyoming), 23  
 Little-Marenin, I. R. 1986, *ApJ*, 307, L15  
 Little-Marenin, I. R., Benson, P. J., & Dickinson, D. F. 1988, *ApJ*, 330, 828  
 Lloyd Evans, T. 1990, *MNRAS*, 243, 336  
 Marsh, T. 1989, *PASP* 101, 1032  
 Nakada, Y., Izumiura, H., Onaka, T., & Hashimoto, O. 1987, *ApJ*, 323, L77  
 te Lintel Kekkert, P. 1990, Ph.D. thesis, Univ. of Leiden  
 Willems, F. J., & de Jong, T. 1986, *ApJ*, 309, L39



## **Appendix G**

### **Spatially Resolved Spectra of Silicate Dust Around $\alpha$ Orionis**

## SPATIALLY RESOLVED SPECTRA OF SILICATE DUST AROUND $\alpha$ ORIONIS<sup>1</sup>

G. C. SLOAN<sup>2</sup>

Department of Physics and Astronomy, University of Wyoming, P.O. Box 3905, Laramie, WY 82071

G. L. GRASDALEN

G-star Enterprises, 286 South Pennsylvania, Denver, CO 80209

AND

PAUL D. LEVAN<sup>3</sup>

Phillips Laboratory, PL/GPOB, Hanscom AFB, MA 01731

Received 1992 April 13; accepted 1992 July 23

### ABSTRACT

We have observed  $\alpha$  Orionis with a 10  $\mu$ m long-slit spectrometer. By applying maximum entropy reconstruction techniques, we have spatially resolved the silicate emission from the circumstellar shell. The emissivity derived from our silicate spectrum compares favorably with published emissivity profiles describing circumstellar silicates. The lack of silicate emission in the direction of the central star suggests that the circumstellar dust may not be distributed in a spherical shell.

*Subject headings:* circumstellar matter — dust, extinction — infrared: stars — stars: individual ( $\alpha$  Orionis)

### 1. INTRODUCTION

The star  $\alpha$  Orionis has become the quintessential case of an evolved star with a circumstellar shell. Expanding material around  $\alpha$  Ori was first identified by Adams & MacCormack (1935), who detected blueshifted absorption cores in the H, K, D, and Al I and II lines in spectra of  $\alpha$  Ori. Deutsch (1956) clarified the situation when he described similar spectral properties in  $\alpha$  Her. In this system, he argued that the absorption lines seen in the spectra of both visual components arose in an extended circumstellar envelope. He identified several additional stars, including  $\alpha$  Ori, which also possessed circumstellar envelopes and attributed these to mass-loss from the central star. Early infrared observations provided clues to the nature of the material around  $\alpha$  Ori by revealing emission features from silicate dust at 10 and 20  $\mu$ m (Gillett, Low, & Stein 1968; Woolf & Ney 1969).

Since McCarthy, Low, & Howell (1977) first resolved the dust shell, further interferometric work has substantially improved our understanding of  $\alpha$  Ori and its shell. Bester et al. (1991) used heterodyne interferometry at 11  $\mu$ m to resolve the shell around  $\alpha$  Ori. They combined their data with earlier speckle observations by Sutton (1979) and Howell, McCarthy, & Low (1981), and modeled the resulting visibility curve with an optically thin ( $\tau = 0.042$ ) hollow dust shell with an inner radius of 0".9 ( $\sim 40R_*$ ). Dyck & Benson (1992) modeled their speckle observations from 8 to 13  $\mu$ m with a Gaussian with a full width at half maximum (FWHM) of 2".6. We compared the visibility curve of their model with that of Bester et al. and found that the two agree very closely.

Bester et al. (1991) argued that the large inner radius of the dust shell and its low dust temperature (280 K) make it unlikely that the inner edge of the shell corresponds to the condensation radius of the dust. Rather,  $\alpha$  Ori has ended its most recent mass loss phase. Dust is no longer condensing, and

the inner boundary of the shell is moving away from the star. In this scenario, the grains around  $\alpha$  Ori are still young. Assuming a distance of 200 pc and a constant velocity of 10 km s<sup>-1</sup> (Weymann 1962), the material presently located 0".9 from the central star would be about 85 yr old.

We chose to study  $\alpha$  Ori with an infrared slit spectrometer because of its high infrared brightness and because the recent interferometric results of Bester et al. (1991) and Dyck & Benson (1992) indicated that we could spatially resolve emission from its dust shell.

### 2. OBSERVATIONS

We observed  $\alpha$  Ori on 1991 February 6 with GLADYS, the Geophysics Laboratory 10  $\mu$ m array spectrometer (LeVan 1990), mounted on the 2.3 m telescope at the Wyoming Infrared Observatory (WIRO). After integrating on  $\alpha$  Ori, we immediately observed  $\alpha$  Tau to provide both a spectral and point source reference observed at nearly the same air mass, direction in the sky, and time.

For both objects, the slit and the chop throw were in the north/south direction. We chopped at a frequency of 1.5 Hz, using the three-beam chop described by Landau, Grasdalen, & Sloan (1992). For  $\alpha$  Ori, we took 10 images, each consisting of 40 chops, and for  $\alpha$  Tau, 20 images of 120 chops each. We allowed the objects to slowly drift along the slit, so that the position of the star in the slit would shift slightly from one image to the next. Further details of our observing procedure are described in Grasdalen, Sloan, & LeVan (1992, hereafter Paper I).

### 3. DATA REDUCTION AND ANALYSIS

We determined our wavelength calibration as described by LeVan (1990) and flat-fielded our data as described in Paper I. In Paper I, we presented a spatiogram (plot of width vs. wavelength) for our  $\alpha$  Ori data, which demonstrated that we had resolved emission from silicate dust around  $\alpha$  Ori.

We extracted a one-dimensional spectrum from each two-dimensional image of  $\alpha$  Ori and co-added the resulting spectra to produce the spectrum in Figure 1. We corrected for atmo-

<sup>1</sup> Contribution 136 of the Wyoming Infrared Observatory.

<sup>2</sup> Postal address: Phillips Laboratory, PL/GPOB, Hanscom AFB, MA 01731.

<sup>3</sup> Postal address: Phillips Laboratory, PL/VTRP, Kirtland AFB, NM 87117.

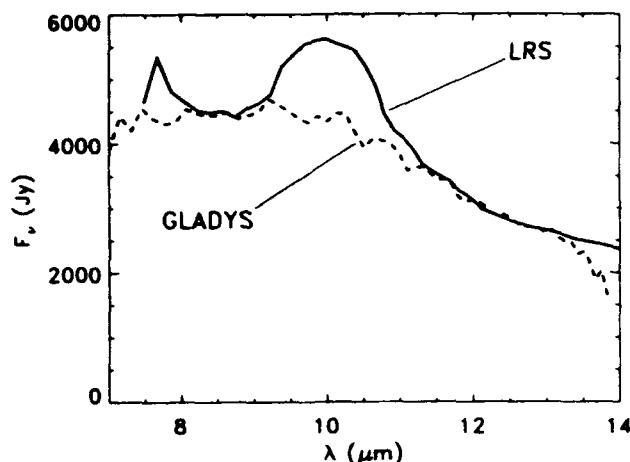


FIG. 1.—Spectra of  $\alpha$  Ori from the LRS and GLADYS. The LRS spectrum contains much more silicate emission than seen by GLADYS, indicating that the emitting region is larger than the  $2'' \times 9''$  slit in GLADYS. The higher noise in the GLADYS spectrum is primarily the result of an insufficient integration time of the spectral standard,  $\alpha$  Tau.

spheric and instrumental transmission and detector response by dividing by  $\alpha$  Tau and then multiplying by a  $\lambda^{-2}$  Rayleigh-Jeans distribution. Figure 1 illustrates the lack of silicate emission observed by GLADYS when compared to results from the *IRAS* Low Resolution Spectrometer (LRS). This difference strongly supports the notion that the shell around  $\alpha$  Ori is extended on the order of at least a few arcsec. Much of the silicate emission arises in a region outside the  $2'' \times 9''$  slit used by GLADYS.

In order to learn more about the nature of the extended emission, we applied maximum entropy techniques to our  $\alpha$  Ori data to remove the effects of atmospheric seeing as well as diffraction from the telescope and instrument. Maximum entropy reconstruction solves a number of difficulties with the reduction of long-slit spectroscopic data. Presently, GLADYS uses an array of Si:Ga detectors in a  $10 \times 62$  pixel configuration. The pixel size ( $0''.88$ ) is closely matched to the diffraction limit of the telescope ( $1''.0$ ), so each individual image is spatially undersampled. The dispersion axis of the NaCl prism is inclined slightly to the long array axis. In addition, lines of constant wavelength are not orthogonal to the dispersion axis or to either of the array axes. Geometric transformations to orthogonalize the data would reduce spatial and spectral resolution, since they require interpolation in our under-sampled array. Co-adding the individual data images would require a shift-and-add algorithm, which again would reduce the resolution.

Our reconstruction method is based on the MEMSYS algorithm of Gull & Skilling (1984, 1989). We chose to map the original 10 row data into 19 rows, each  $0''.44$  in extent. The key to implementing a maximum entropy algorithm is to adequately describe the behavior of the point spread function (PSF). The PSF is the result of the seeing disk from the atmosphere, the Airy disk from the telescope, and the diffraction pattern from the instrument, each of which is a function of wavelength, as well as the motion of the star within the slit.

To analytically describe the function  $\text{PSF}(\lambda)$  precisely would be impossible. A complete description of the full PSF in both the spatial and spectral directions would require observations of monochromatic point sources. We have chosen only to correct for the effects of the PSF in the spatial direction, deter-

mining a one-dimensional PSF at each wavelength instead of a full, two-dimensional PSF.

We found the best approach was to model the PSF at each wavelength with the sum of a Gaussian and an exponential, using our 20 images of  $\alpha$  Tau as a point source reference. A Gaussian alone is inadequate for MEMSYS, since it underestimates the wings of the PSF.

The first step in our procedure was to determine the position of  $\alpha$  Tau in the slit in each image. At each wavelength, we fit a Gaussian to the spatial cut to determine the fractional pixel position of the center of the PSF. As explained above, these positions fall on a line slightly inclined to the 62 pixel axis of the array. We used a least-squares method to determine the position of this line on our array, and thus the precise position of the star in our slit in each image.

Since  $\alpha$  Tau slowly drifted during our integration, we actually have 20 values across each pixel, one from each image. The net effect is that we have heavily oversampled the PSF spatially. We generated PSF profiles at each wavelength by plotting data from all 20 images, shifted by their respective offsets. We fit our Gaussian and exponential model to the data using a downhill simplex method (Press et al. 1988), minimizing the square of the differences between our model and the data. Figure 2 illustrates actual profiles and our models fit to them at two wavelengths. We produced a separate  $\text{PSF}(\lambda)$  surface for each  $\alpha$  Ori image, correcting for the relative positions of  $\alpha$  Ori in the slit.

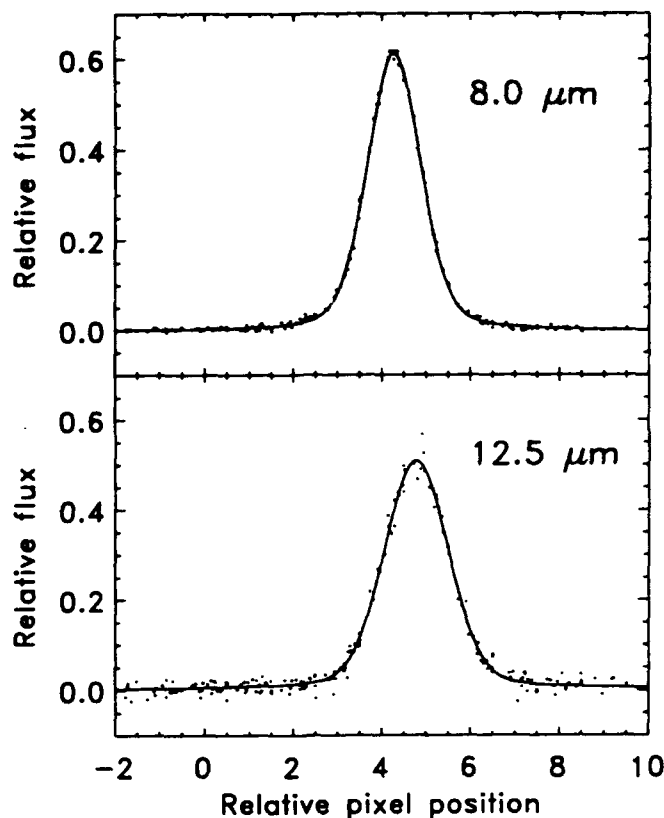


FIG. 2.—Point spread functions based on  $\alpha$  Tau data at wavelengths of 8.0 and 12.5  $\mu\text{m}$ . The dots represent the data from 20 individual  $\alpha$  Tau images, corrected for the position of the star in the slit. The solid lines are our best fit to the data, using a model profile which is the sum of the Gaussian and an exponential. The PSF is clearly broader at longer wavelengths.

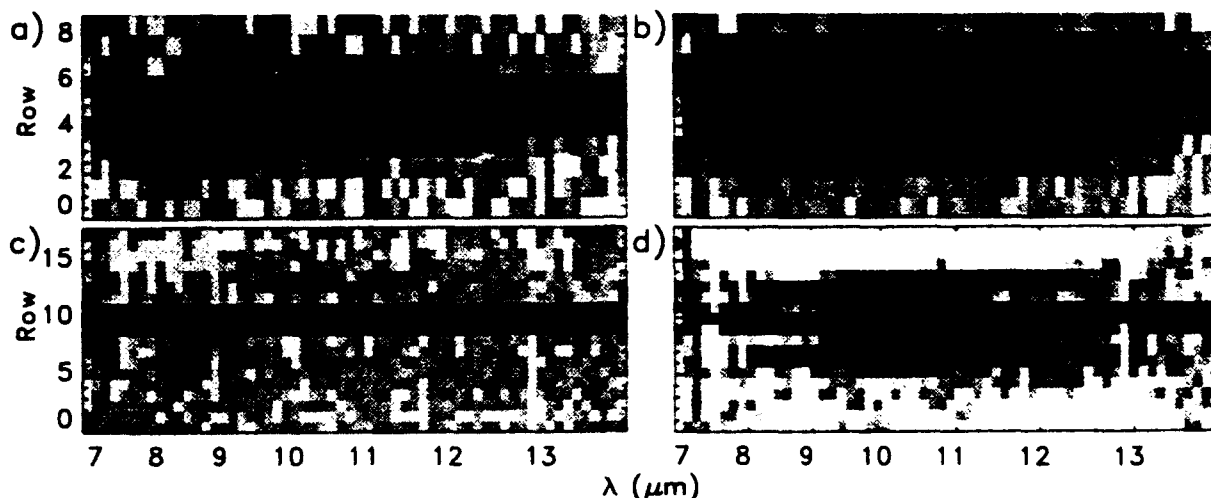


FIG. 3.—Results of MEMSYS maximum entropy reconstruction, illustrated with gray-scale images of the log of the flux. (a) A single  $\alpha$  Tau image before reconstruction. (b) The sum of 20 reconstructed  $\alpha$  Tau images. (c) A single  $\alpha$  Ori image prior to reconstruction. (d) The sum of the reconstructed  $\alpha$  Ori images. The reconstruction regridded the original 10 row data onto 19 rows and corrected for the angle between the dispersion axis and the array apparent in the upper panels. The reconstruction of  $\alpha$  Ori contains emission away from the star well above the noise. The reconstruction of  $\alpha$  Tau is nearly a point source.

We tested our MEMSYS algorithm by generating synthetic images of  $\alpha$  Tau with side-row spectra. We created two synthetic images, one with side-row spectra spaced one pixel ( $0''.9$ ) on either side of the central spectrum and reduced in strength by a factor of 10, and the other with side-row spectra spaced 2 pixels ( $1''.8$ ) away. MEMSYS had no difficulty with the  $2''$  spacing, resolving the side spectra nicely. The  $1''$  spacing posed more of a problem. The reconstructions were clearly broader than a point source, but most of the excess emission appeared only  $0''.5$  away from the central row. These results suggest that MEMSYS systematically shifts low surface brightness emission originating close to the central row even closer.

Figure 3 illustrates the results of our MEMSYS reconstructions of  $\alpha$  Tau and  $\alpha$  Ori. MEMSYS shifted the center of all  $\alpha$  Ori images to row 10, allowing us to co-add them directly; no shifting or interpolating was necessary. We reconstructed the  $\alpha$  Tau images to test our algorithm; it is gratifying that the

reconstruction of  $\alpha$  Tau is very close to that expected for a point source. The reconstruction of  $\alpha$  Ori contains emission away from the central star well above the noise level. *We have successfully resolved the dust shell of  $\alpha$  Ori!*

#### 4. RESULTS

The profile of the star and shell across our slit illustrated in Figure 4 shows that we have resolved the circumstellar emission from  $\alpha$  Ori. As a result, we do not have to make any assumptions about the nature of the stellar flux to isolate the spectral contribution from the shell; we have observed it directly.

We produced a spectrum in Figure 5 of the outer emission regions (rows 5–8 and 12–15 in our reconstruction) by summing over them, dividing by our spectrum of  $\alpha$  Tau, and multiplying by the assumed shape of the actual spectrum of  $\alpha$  Tau. (We discuss the nature of the actual spectrum of  $\alpha$  Tau below.) The resulting spectrum is reasonably smooth, demonstrating the quality of the MEMSYS reconstruction in these

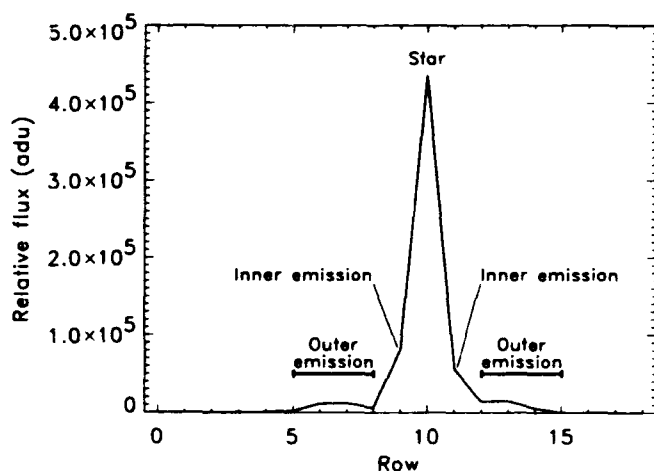


FIG. 4.—Profile of  $\alpha$  Ori across our slit, summed from 9 to  $12\ \mu\text{m}$ . Each row corresponds to  $0''.44$ . The central row (10) contains the stellar spectrum. The outer silicate emission region (rows 5–8 and 12–15) is underneath the solid bars in the figure. The rows adjacent to the central row (9 and 11) represent the inner silicate emission region.

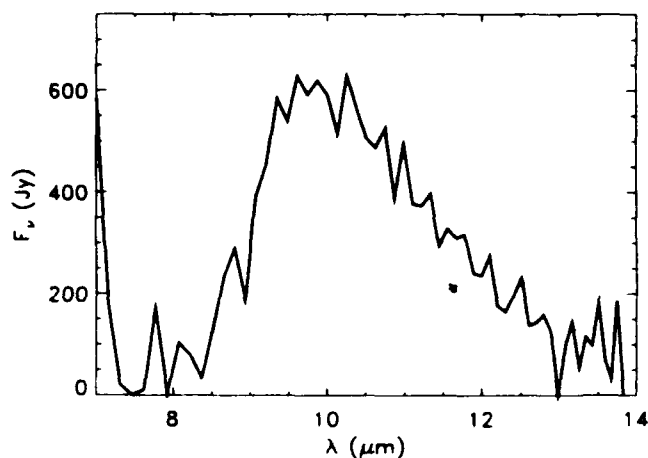


FIG. 5.—Spectrum from the outer emission region (rows 5–8 and 12–15). The spectrum contains only silicate emission.

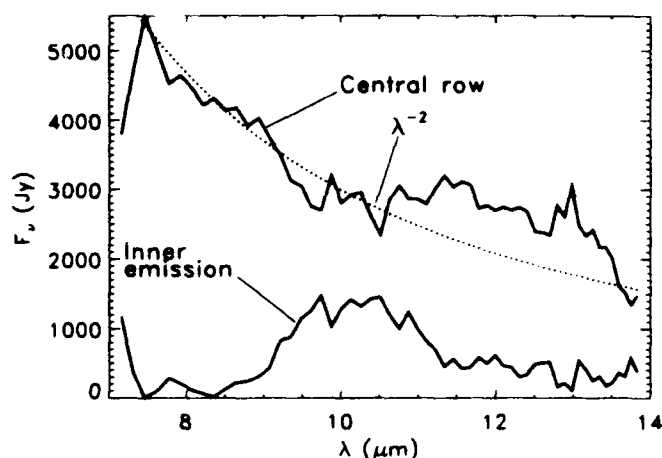


FIG. 6.—Spectra of the central row and the inner emission region of our reconstruction. Most of the noise in the spectra results from difficulties MEMSYS had disentangling the silicate and photospheric emission in this region. The dotted curve is a  $\lambda^{-2}$  Rayleigh-Jeans distribution.

rows. The spectrum is clearly silicate in nature; there is no contamination from the photosphere.

The inner region of silicate emission (rows 9 and 11) is more problematic, primarily because MEMSYS had to dig the silicate emission in these rows out from under the substantial flux from  $\alpha$  Ori. Nonetheless, the reconstructed spectrum from this region contains little or no photospheric emission (Fig. 6); it arises from silicate material close to  $\alpha$  Ori.

The central row contains no silicate emission at  $10 \mu\text{m}$  (Fig. 6). It is surprising that the emission from this row appears to be photospheric, given that silicate emission appears only  $0.5$  to either side. Using our tests with synthetic side-row spectra to interpret these results, we conclude that the inner region producing the silicate emission close to the star in our reconstructions is on the order of  $1''$  away from  $\alpha$  Ori.

At  $12 \mu\text{m}$ , the central spectrum has excess emission, which we attribute to silicates which have not been resolved from the photospheric spectrum. The poorer resolution results from the larger diffraction pattern and lower signal-to-noise ratio at these longer wavelengths. This emission probably arises from the same region producing the inner silicate emission.

## 5. DISCUSSION

Cohen et al. (1992) have raised the troubling issue that our understanding of photospheric emission from late-type giants in this wavelength regime is much less advanced than we had hoped. In particular, these stars appear to exhibit absorption from SiO in their spectra, including those stars long assumed to have featureless spectra at  $10 \mu\text{m}$  such as  $\alpha$  Tau and  $\alpha$  Boo. We decided to use their photometrically calibrated spectrum for  $\alpha$  Tau (Cohen, Walker, & Witteborn 1992) to calibrate the spectra in Figures 5–7. To calibrate the GLADYS spectrum in Figure 1, however, we used a Rayleigh-Jeans distribution, since we are comparing our data to the LRS data, which were calibrated in a similar manner. For our purposes, the only significant departure in the spectrum of  $\alpha$  Tau from a Rayleigh-Jeans distribution is the SiO absorption band around  $8 \mu\text{m}$ . This deviation has little effect on our silicate profiles, since silicate emission is minimal near  $8 \mu\text{m}$ . It does, however, affect the shape of the photospheric spectrum of  $\alpha$  Ori in Figure 6.

We are not aware of any M supergiants for which the photospheric spectrum is not veiled by silicate emission. Given our lack of understanding of what the spectrum from the photo-

sphere of  $\alpha$  Ori should look like, interpreting the nature of the central spectrum of our reconstructions is very difficult.

A comparison of the silicate emission in Figures 5 and 6 shows that the silicate emission feature from the outer region is broader and peaks at a shorter wavelength than the emission from the inner region. The difference in the width of the features would be eliminated if we included the excess emission around  $12 \mu\text{m}$  seen in the central row with the inner emission. It is tempting to relate the shift in peak wavelength to the evolutionary scenario for silicate grains proposed by Little-Marenin & Little (1990) and Stencel et al. (1990), but given the difficulties in reconstructing the inner rows, we cannot rule out the possibility that this shift is just an artifact of our reconstruction method.

To convert our silicate spectrum to an emissivity profile, we have divided by a blackbody of temperature  $280 \text{ K}$ . Bester et al. (1991) give a dust temperature at the inner shell boundary of  $280 \text{ K}$ . We also determined a dust temperature by fitting silicate profiles to the silicate features extracted from the  $\alpha$  Ori spectrum taken by the LRS. The temperature varied from  $280$  to  $290 \text{ K}$ , depending on the assumed profile.

In Figure 7, we compare the emissivity from the outer silicate emission region with the profiles of Draine & Lee (1984, hereafter DL; tabulated by Draine 1985) and Ossenkopf, Henning, & Mathis (1992, hereafter OHM). The DL profile is significantly broader than ours, but theirs is not a model of circumstellar silicates. Rather, they obtained their profile by matching the shape of the silicate feature seen in the Trapezium, which arises from interstellar silicate grains. The difference between the properties of interstellar and circumstellar silicates has been pointed out before (e.g., Nuth & Hecht 1990; Simpson 1991) and is discussed extensively by OHM. The general shape of the OHM profile matches ours well, although our profile is shifted slightly to the blue. Their profile is based primarily on feature profiles extracted from LRS spectra of evolved stars by Volk & Kwok (1988) and is more representative of circumstellar silicates. We have also compared our profile with the opacity curve given by Dyck & Benson (1992). Their profile is shifted to the red slightly, but has a very similar shape, much like the OHM profile.

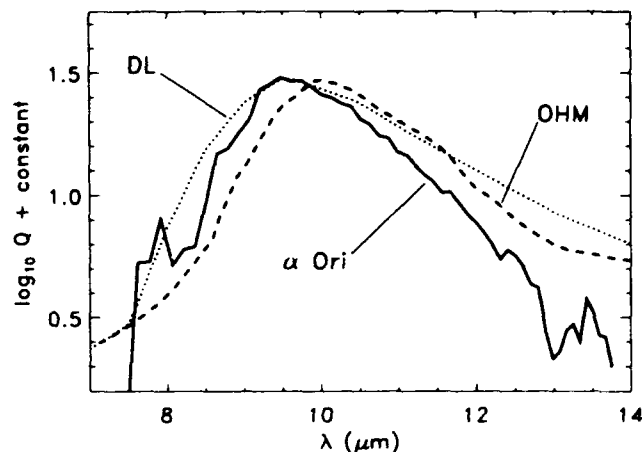


FIG. 7.—Comparison of emissivities of the silicate dust around  $\alpha$  Ori with profiles by Ossenkopf et al. (1992, labeled as OHM) and Draine & Lee (1984, labeled as DL). The OHM profile is the dashed line; the dotted line is the DL profile. We produced the  $\alpha$  Ori profile by summing only the rows containing the outer emission region, dividing by a  $280 \text{ K}$  blackbody, and smoothing the result.

Our reconstructions show very little silicate dust along the line of sight (LOS) directly toward  $\alpha$  Ori. This result is not consistent with any spherically symmetric shell because in such a model, the LOS must pass through the shell in front of and behind the star. For example, in the hollow shell of Bester et al. (1991), the central row in our reconstructions would contain 95% of the silicate flux in either adjacent row. For any spherically symmetric model, this fraction is still large. There are other geometries which would be consistent with our work and the interferometry results of Bester et al. (1991) and Dyck & Benson (1992). The emission might arise from clumps around  $\alpha$  Ori with a characteristic separation of  $0''.9$ , or the dust might be distributed in a biconical geometry.

We thank R. Canterna for providing us with computer facilities for data reduction. We used IDL (Interactive Data Language) to reduce and analyze our data and found it to be a wonderful package. The LRS data base at the Center for Astrophysics and Space Astronomy at CU Boulder also proved very useful. It is maintained by R. Stencel, who along with H. M. Dyck and R. Canterna, provided us with helpful discussions and comments. We are also grateful to M. Cohen and F. Witteborn, who furnished us with their corrected spectrum of  $\alpha$  Tau, and J. Mathis, who sent us a preliminary version of the manuscript of OHM. Astronomy at WIRO is supported by the State of Wyoming and the Air Force Office of Scientific Research.

## REFERENCES

- Adams, H. A., & MacCormack, E. 1935, *ApJ*, 81, 119  
 Bester, M., Danchi, W. C., Degiacomi, C. G., Townes, C. H., & Geballe, T. R. 1991, *ApJ*, 367, L27  
 Cohen, M., Walker, R. G., & Witteborn, F. C. 1992, *AJ*, in press  
 Cohen, M., Witteborn, F. C., Carbon, D., Augason, G., Wooden, D., Bregman, J. D., & Goorvitch, D. 1992, *AJ*, in press  
 Deutsch, A. J. 1956, *ApJ*, 123, 210  
 Draine, B. T. 1985, *ApJS*, 57, 587  
 Draine, B. T., & Lee, H. M. 1984, *ApJ*, 285, 89 (DL)  
 Dyck, H. M., & Benson, J. A. 1992, *AJ*, 104, 377  
 Gillett, F. C., Low, F. J., & Stein, W. A. 1968, *ApJ*, 154, 677  
 Grasdaen, G. L., Sloan, G. C., & LeVan, P. D. 1992, *ApJ*, 384, L25 (Paper I)  
 Gull S. F., & Skilling, J. 1984, *Proc. IEEE*, 131, 646  
 ———. 1989, *Quantified Maximum Entropy "MEMSYS 3" Users' Manual* (London: Maximum Entropy Data Consultants Ltd.)  
 Howell, R. R., McCarthy, D. W., & Low, F. J. 1981, *ApJ*, 251, L21  
 Landau, R., Grasdaen, G., & Sloan, G. C. 1992, *A&A*, 259, 696  
 LeVan, P. D. 1990, *PASP*, 102, 190  
 Little-Marenin, I. R., & Little, S. J. 1990, *AJ*, 99, 1173  
 McCarthy, D. W., Low, F. H., & Howell, R. 1977, *ApJ*, 214, L85  
 Nuth III, J. A., & Hecht, J. H., 1990, *Ap&SS*, 163, 79  
 Ossenkopf, V., Henning, Th., & Mathis, J. S. 1992, *A&A*, 261, 567 (OHM)  
 Press, W. H., Flannery, B. P., Teukolsky, S. A., & Vetterling, W. T. 1988, *Numerical Recipes in C: The Art of Scientific Computing* (Cambridge: Cambridge Univ. Press)  
 Simpson, J. P. 1991, *ApJ*, 368, 570  
 Stencel, R. E., Nuth III, J. A., Little-Marenin, I. R., & Little, S. J. 1990, *ApJ*, 350, L45  
 Sutton, E. C. 1979, in *IAU Colloq. 50, High Angular Resolution Stellar Interferometry*, ed. J. Davis & W. J. Tango (Sydney: Univ.), 16  
 Volk, K., & Kwok, S. 1988, *ApJ*, 331, 435  
 Weymann, R. 1962, *ApJ*, 136, 844  
 Woolf, N. J., & Ney, E. P. 1969, *ApJ*, 155, L181



**Appendix H**  
**Spatially Resolved Spectra of the Unidentified Infrared Features Around HD 44179**  
**(The Red Rectangle)**

**SPATIALLY RESOLVED SPECTRA  
OF THE UNIDENTIFIED INFRARED  
FEATURES AROUND HD 44179  
(THE RED RECTANGLE)<sup>1</sup>**

G.C. Sloan<sup>2</sup>

Department of Physics and Astronomy, University of Wyoming  
P.O. Box 3905, Laramie, WY 82071

G.L. Grasdalen

G-star Enterprises

286 S. Pennsylvania, Denver, CO 80209

Paul D. LeVan<sup>3</sup>

Phillips Laboratory

PL/GPOB, Hanscom AFB, MA 01731

To be published by: *The Astrophysical Journal*, **409**, 1993 May 20

Received 1992 September 8; accepted 1992 November 16

---

<sup>1</sup>Contribution 137 of the Wyoming Infrared Observatory

<sup>2</sup>Present address: Phillips Laboratory, PL/GPOB, Hanscom AFB, MA 01731

<sup>3</sup>Present address: Phillips Laboratory, PL/VTRP, Kirtland AFB, NM 87117

## Abstract

We have observed HD 44179 and the surrounding unidentified infrared (UIR) emission with a long-slit 10  $\mu\text{m}$  spectrometer. By applying maximum entropy reconstruction methods to our images, we have found spatial variations in the spectra not apparent in previous work with beam sizes of several arcseconds diameter. We find that no UIR emission arises in the inner-most regions of the source; instead, we observe only cool continuum emission. After its abrupt appearance 0.5 arcsec from the central source, the UIR emission decays steadily with distance, except for an enhancement in the intensity of the 11.3  $\mu\text{m}$  feature roughly 1.5 arcsec away from the central source. The intensity of the 7.7  $\mu\text{m}$  feature drops more quickly with distance than the intensity of the 8.6 and 11.3  $\mu\text{m}$  features, and the wavelength of peak intensity of this feature appears to shift from 7.9  $\mu\text{m}$  near the central source to roughly 7.4  $\mu\text{m}$  further away. These observations indicate that we have detected the formation of the carriers of the UIR emission features and changes in their emission properties as they move outward. In particular, the behavior of the 8.6 and 11.3  $\mu\text{m}$  features suggest the material is growing increasingly hydrogenated with distance. We suggest that all the unusual spectral properties of this system can be explained in terms of an accretion disk around a degenerate object.

*Subject headings:* infrared: interstellar: continuum — ISM: individual (Red Rectangle) — stars: individual (HD 44179)

## 1. Introduction

HD 44179 was detected as a bright infrared source in the Air Force Cambridge Research Laboratory's rocket sky survey (Walker and Price 1975). It has since become one of the most studied sources of the unidentified infrared (UIR) emission features. Cohen et al. (1975) associated the infrared source with the star HD 44179 and a nearly rectangular object extended  $\sim 40$  arcsec north/south on the red Palomar Sky Survey plates. The central star, which they classified as B9-A0 III, is embedded in a bipolar reflection nebula. We will refer to the central source as HD 44179 and the surrounding nebulosity as the Red Rectangle. Because of its unusual morphology, its carbon-rich nature, its galactic latitude ( $-12^\circ$ ), and the lack of interstellar material in the region, Zuckerman et al. (1976) argue that the object is a proto-planetary nebula.

The UIR features were first detected by Gillett, Forrest, and Merrill (1973) in spectra of the planetary nebulae BD +30°3639 and NGC 7027. Merrill soon after observed these features in the Red Rectangle (Cohen et al. 1975). Since that time, several hypotheses have been introduced to explain the carriers of the features. Most invoke small particles which are briefly heated to 1000 K by the absorption of a UV photon and are sufficiently refractory to survive intact, an idea advanced by Sellgren (1984) to explain the near-infrared continuum she observed in reflection nebulae. For this reason, carbon has been the basis of all the models, an argument strongly supported by the correlation between C/O ratio and  $7.7\ \mu\text{m}$  flux discovered for several planetary nebulae by Cohen et al. (1986).

A widely accepted explanation of the UIR features is the polycyclic aromatic hydrocarbon (PAH) model, which suggests that the features arise from C-H and C-C bonds in large molecules consisting of hydrogenated aromatic rings (Allamandola, Tielens and Barker 1985, 1989; Léger and Puget 1984; Léger, d'Hendecourt, and Défourneau 1989). Other models include hydrogenated amorphous carbon (HAC; Jones, Duley, and Williams 1990; Blanco, Bussoletti, and Colangeli 1988; and references therein) and quenched carbonaceous composites (QCC; Sakata et al. 1984, 1987, 1990).

HD 44179 is extended on the order of 1 arcsec in the near-infrared (Dainty et al. 1985; Leinert and Haas 1989). Geballe et al. (1989) have found that emission from the  $3.3\ \mu\text{m}$  UIR feature is detectable in a 5 arcsec beam centered 5 arcsec north of HD 44179. While the feature emission is 60 times weaker than in the central region, it is nevertheless clear that its shape differs, having a higher proportion of emission at  $3.4\ \mu\text{m}$  and other features not seen in the central region as well.

We chose to observe the Red Rectangle with a long-slit  $10\ \mu\text{m}$  spectrometer to extend these studies of the spatial nature of the UIR emission to features seen in the  $10\ \mu\text{m}$  band. Spatial variations in the nature of the UIR emission may allow us to

distinguish between the different models of the carriers of the UIR emission. In Grasdalen, Sloan, and LeVan (1992, hereafter Paper I), we published preliminary results of our observations. By fitting a spatial profile to the object at each wavelength in our spectral images, we showed that the object was spatially extended at the wavelengths of all four UIR features detected between 7 and 14  $\mu\text{m}$ . To gain a better understanding of the behavior of the UIR features with position in our images, we have chosen to apply maximum entropy techniques to our data. Here, we present the results of our maximum entropy reconstructions.

## 2. Observations and Data Reduction

We observed the Red Rectangle with the Air Force Geophysics Laboratory 10  $\mu\text{m}$  Array Detector Spectrometer (GLADYS; LeVan 1990) mounted at the Cassegrain focus of the 2.3 m reflecting telescope of the Wyoming Infrared Observatory (WIRO). We made our observations by reading a 10 $\times$ 62 portion of the Si:Ga array; each of the 10 rows spans 0.88 arcsec of the sky along the slit. We performed background subtraction using the three-beam chop method described by Landau, Grasdalen and Sloan (1992), chopping at 1.5 Hz with a throw of 23 arcsec north and south of the object. The slit was oriented in the same direction as the chop.

Observations taken on 1991 February 10 consisted of 40 images of the Red Rectangle and 40 images of  $\alpha$  Tau, which we used as a spectroscopic and point source reference. The data were taken in two sets, with the Red Rectangle observations sandwiched between observations of our standard in each. In the first set each image of the Red Rectangle consisted of 240 chops, while each  $\alpha$  Tau image represents 80 chops. We improved the focus and increased the integration time for the second set of data, collecting 320 chops in each Red Rectangle image and 160 in each  $\alpha$  Tau image.

The images were flat-fielded as described in Paper I. Before extracting spectra, we used maximum entropy techniques to reconstruct our images, using a modification of the MEMSYS algorithm of Gull and Skilling (1984, 1989). In our study of  $\alpha$  Ori (Sloan, Grasdalen, and LeVan 1992; hereafter Paper II), we optimized our maximum entropy algorithm by carefully studying its effects on observations of point sources, simulations of extended sources, and the  $\alpha$  Ori images themselves. The resultant algorithm is described in Paper II. We used our observations of  $\alpha$  Tau to determine the behavior of the point spread function (PSF) with wavelength.

We reconstructed each of the 40 Red Rectangle images separately. We originally tried to improve the signal/noise ratio of our reconstructions by combining the images before reconstruction. The poorer spatial resolution of the sum compromised the quality of the reconstructions, so we chose to reconstruct all the images individually. We then summed the 20 individually reconstructed images of

each set and examined these two sums separately. The final reconstruction has 19 rows of 0.44 arcsec extent each. Figure 1 illustrates the effects of reconstruction on our images.

We corrected our data for atmospheric and instrumental transmission by dividing by a spectrum extracted from the  $\alpha$  Tau images and multiplying by a  $\lambda^{-2}$  Rayleigh-Jeans distribution fixed at 840 Jy at 8.7  $\mu$ m. A photometrically calibrated infrared spectrum of  $\alpha$  Tau has recently become available (Cohen, Walker and Witteborn 1992). The spectrum shows deviations from a Rayleigh-Jeans distribution (of approximately 15% at 8  $\mu$ m), but they will not affect our conclusions about relative changes in the spectra with spatial position.

### 3. Analysis

Figure 2 presents the spectrum of the central row of the reconstruction of our better focused integration of HD 44179. *The UIR features are completely absent in the central row.* Our reconstructions have resolved the UIR emission region and the central continuum source.

Despite the poorer focus of our first set of images of the Red Rectangle, we found that outside of the three central rows (9, 10, and 11), where the maximum entropy reconstruction algorithm had a difficult time disentangling UIR emission from continuum emission, the quality of both sets of reconstructions was similar. We produced Figure 3 by summing rows equidistant from the central continuum source on either side in groups of two. With the exception of rows 9 and 11 in the more poorly focused data set, we used all off-center rows from both reconstructions.

The side row spectra in Figure 3 contain very little of the continuum present in the central row; the features at 7.7, 8.6, 11.3, and 12.7  $\mu$ m dominate the emission. These features show no obvious deviations from symmetry on either side of HD 44179. They continue to the edge of the slit, where they disappear into the noise.

The character of the spectra changes dramatically with distance from HD 44179 (as illustrated in Figure 3). The spectrum from the central region of the nebula (within 1 arcsec) dominates the emergent UIR flux and resembles very closely the nature of the UIR emission in all previously published spectra of the Red Rectangle. From 1 to 2 arcsec from the center, the strength of the 7.7  $\mu$ m feature drops much more quickly than the strength of the 8.6 and 11.3  $\mu$ m features and a second peak in the 7.7  $\mu$ m feature becomes apparent at roughly 7.4  $\mu$ m. Further from the center, this peak dominates the 7.9  $\mu$ m flux, and the features at 8.6, 11.3, and 12.7  $\mu$ m features sink into the noise.

The rise in flux at 7.0  $\mu\text{m}$  and 13.5  $\mu\text{m}$  close to the edge of the slit may be attributable to the poor transmission at the edges of the 10  $\mu\text{m}$  window. At the edges of the window, the difficulty in accurately determining the PSF as well as noise in the spectra of the Red Rectangle and  $\alpha$  Tau all contribute to a low signal/noise ratio in the reconstructed spectra. For this reason, we doubt that the apparent feature at 7.0  $\mu\text{m}$  is real.

To more carefully analyze the nature of the emission from the UIR features with position in the slit, we extracted the flux from each feature in each row of both our reconstructions. For a given feature, we held the wavelength interval over which we measured the flux fixed in all rows. We fitted the continuum to the data on either side of each feature. Separating the emission from the 7.7 and 8.6  $\mu\text{m}$  features was not trivial. We first determined the total flux from the blended features, then fitted a linear "continuum" underneath the 8.6  $\mu\text{m}$  feature running from the shoulder of the 7.7  $\mu\text{m}$  feature at 8.0  $\mu\text{m}$  to the continuum at 9.0  $\mu\text{m}$ . The flux above this line we attributed to the 8.6  $\mu\text{m}$  feature. By subtracting this from the total flux of the blended feature, we isolated the contribution of the 7.7  $\mu\text{m}$  feature.

In Figure 4 we plot the flux of each feature against distance from HD 44179. Each point is a mean of four data: one from either side of the central source in each of the two reconstructions. We derived the error bars from the distribution of these four points. Because MEMSYS constrains the reconstructions to be positive, their statistics are decidedly non-gaussian. This behavior means it would be incorrect to determine formal errors in the feature fluxes by traditional methods, such as using the root mean square of the deviations in the continuum. We have not included feature fluxes beyond four rows from HD 44179 in the reconstructions because we do not consider our measured fluxes beyond that point to be statistically meaningful.

The plots of three of the four feature fluxes, at 7.7, 8.6, and 12.7  $\mu\text{m}$ , fall steadily from a maximum 0.5 arcsec from HD 44179. The 11.3  $\mu\text{m}$  feature behaves quite differently, initially dropping in strength, but then climbing to a secondary maximum 1.4 arcsec (3 pixels) from the central source. This effect was seen on either side of HD 44179, in both sets of data. No such effect is seen in the other features.

## 4. Discussion

### 4.1. The Central Source

The clean separation of the continuum source and the UIR features illustrated in Figure 2 allows us to examine the character of the spectrum of the central source without having to remove the effects of the UIR emission. The best fit to the central spectrum is a 370 K blackbody. Dainty et al. (1985) and Leinert and Haas (1989) have used speckle techniques in the near-infrared (from J to M) to resolve the central

source of the Red Rectangle into a central component roughly 0.2 arcsec across and a larger component extended roughly 0.4 arcsec east/west and 0.9 arcsec north/south. Based on the lack of polarization from the emission, Dainty et al. attributed the flux to thermal radiation. We believe that the central continuum source we have observed corresponds to both the components seen at shorter wavelengths.

The lack of UIR emission in the central row of our reconstructions could be explained by a disk which is optically thick in the infrared. Given the geometry of the Red Rectangle, we would expect such a disk to be elongated east/west, in contradiction to the near-infrared speckle results. It is therefore more likely that there is a lack of carriers of the UIR features in the immediate vicinity of HD 44179. *We believe we have observed the formation of the carriers roughly 0.5 arcsec from HD 44179.*

#### **4.2. The 7.7 $\mu\text{m}$ Feature**

In the PAH model, several C-C stretching modes blend to form the 7.7  $\mu\text{m}$  feature, while the 8.6  $\mu\text{m}$  feature arises from a C-H bend in the plane of the aromatic ring. Sakata et al. (1987) were not able to obtain either feature in their QCC samples until they allowed them to oxidize; they explain the origin of these features as a cross-conjugated ketone. Blanco, Bussolletti, and Colangeli (1988) have not been able to produce the 7.7 and 8.6  $\mu\text{m}$  features with their HAC model. They suggest that a mixture of hydrogenated amorphous carbon and PAHs may be necessary to fit the observed spectral characteristics. There is also a possibility that various molecular groups originally invoked by Duley and Williams (1981) may contribute to the nature of the emission in this wavelength regime.

Differences in the peak wavelength and relative shape of the 7.7  $\mu\text{m}$  feature have been emphasized by Cohen et al. (1989) and Bregman (1989). They have noticed that the peak wavelength of this feature is closer to 7.8  $\mu\text{m}$  in planetary nebulae while in reflection nebulae and H II regions, the peak occurs at shorter wavelengths, 7.7 and 7.6  $\mu\text{m}$  respectively. High spectroscopic resolution observations of NGC 7027 by Bregman et al. (1986) explain this shift by showing that the 7.7  $\mu\text{m}$  feature is actually a combination of two features, at roughly 7.8 and 7.6  $\mu\text{m}$ . The peak wavelength depends on the relative intensities of the two blended features.

We believe that for the first time, the peak wavelength of the 7.7  $\mu\text{m}$  feature has been observed to shift with spatial position within an object. In the Red Rectangle, the feature appears to have two components, one at 7.9 and the other at roughly 7.4  $\mu\text{m}$ . As the distance from HD 44179 increases, the intensity of the 7.9  $\mu\text{m}$  feature decreases with respect to the intensity of the 7.4  $\mu\text{m}$  feature, resulting in a shift of the peak wavelength of the blend to shorter wavelengths. Because of the poor atmospheric transmission shortward of 8  $\mu\text{m}$ , the signal-to-noise ratio is lower here than at longer wavelengths and raises the concern that the apparent wavelength



shift may not be real. We have tested our reconstruction method and do not believe that this effect is an artifact of our algorithm. Nonetheless, we suggest that this result be treated cautiously until it is independently confirmed.

We can rule out the possibility that the emission at 7.4  $\mu\text{m}$  is due to the Pfund  $\alpha$  recombination line of hydrogen. Thronson (1982) gives an upper limit ( $2\sigma$ ) to the flux from the Brackett  $\gamma$  line of  $1.5 \times 10^{-15} \text{ W m}^{-2}$ . Assuming a temperature of  $10^4 \text{ K}$  and a density of  $10^4 \text{ cm}^{-3}$ , and taking into account the difference in extinction between 2.2 and 7.4  $\mu\text{m}$ , the upper limit to the flux from Pfund  $\alpha$  would be  $8.5 \times 10^{-15} \text{ W m}^{-2}$ , about 5% of the flux actually measured. Estimates based on the radio free-free upper limits reported in Cohen et al. (1975) produce upper limits to the Pfund  $\alpha$  emission which are smaller by at least a factor of 50.

The PAH model ascribes the 7.7  $\mu\text{m}$  feature to a blend of C-C stretches, so a shift in peak wavelength with distance from HD 44179 could indicate changes in composition of the dust or in the physical conditions of the nebula. Given the uncertain nature of the specific components of the 7.7  $\mu\text{m}$  feature in the different models of the UIR features, it is difficult to relate the shift in peak wavelength at 7.7  $\mu\text{m}$  to any specific mechanism.

#### 4.3. The 8.6, 11.3, and 12.7 $\mu\text{m}$ Features

The UIR emission appears to arise from two spatially distinct zones. The 7.7  $\mu\text{m}$  feature dominates in the inner zone, within 1 arcsec of the central source, while emission from the UIR features at 11.3 and 8.6  $\mu\text{m}$  becomes much more significant 1 to 2 arcsec away. If the 7.7  $\mu\text{m}$  feature truly arises from a C-C stretch and the other features from C-H bends, this dichotomy may indicate the degree of dehydrogenation close to the central source.

All the proposed carriers of the UIR emission will produce the 11.3  $\mu\text{m}$  feature from an out-of-plane bend of a C-H bond on the periphery of an aromatic ring. The precise wavelength of the feature depends on the number of adjacent H atoms on the same ring. If the H atom is isolated (solo mode), the feature appears at 11.3  $\mu\text{m}$ . If the bend occurs in an H atom with a single neighbor (duo mode), the transition is seen at roughly 11.9  $\mu\text{m}$ , while the trio mode (two neighbors) radiates at roughly 12.7  $\mu\text{m}$ . Studies of IRAS Low Resolution Spectrometer data by Cohen, Tielens, and Allamandola (1985) and higher resolution spectroscopy by Witteborn et al. (1989) support this model. They found that a feature at 12.7  $\mu\text{m}$  frequently accompanies the 11.3  $\mu\text{m}$  feature, although the 11.9  $\mu\text{m}$  emission is usually weak or nonexistent, possibly because it is smeared into the emission plateau which runs from 11 to 13  $\mu\text{m}$ . They argue that the low excitation of some of their sources rules out the possibility that the 12.7  $\mu\text{m}$  flux actually arises from the [Ne II] emission line at 12.78  $\mu\text{m}$ , and we will assume this to be the case in our discussion below. High-resolution spectroscopy would settle this issue.

The sharp increase of emission at  $11.3\ \mu\text{m}$  compared to the emission at  $12.7\ \mu\text{m}$  at roughly  $1.5\ \text{arcsec}$  from HD 44179 indicates that the solo mode dominates at this distance. This effect could result from a favorable grain geometry or because the molecules or grains are partially dehydrogenated. Higher levels of hydrogenation further from HD 44179 could explain why this enhancement does not persist with increasing distance.

#### 4.4. The Nature of the Red Rectangle

Leinert and Haas emphasize that the current model of the Red Rectangle has problems. At a distance of  $330\ \text{pc}$  (Cohen et al. 1975), the energy output from the Red Rectangle corresponds to  $920\ L_{\odot}$ , while the luminosity from a B9-A0 III star could be at most  $240\ L_{\odot}$ . Rowan-Robinson and Harris (1983) attempted to resolve this difficulty by suggesting that either the object was much closer than  $330\ \text{pc}$  or that the power output was driven by a second, obscured star. Leinert and Haas were led to conclude that the second possibility was the best explanation. While it is plausible, it invokes two rare occurrences: a hidden component buried by many magnitudes of extinction and an object with the rare spectral type B9-A0 III.

We propose that it is possible to explain the Red Rectangle with a simpler model, that of an accretion disk around a degenerate star. An accretion disk would naturally produce a bipolar outflow morphology. In addition, the broad, flat spectral energy distribution (Leinert and Haas 1989, their Fig. 11) is very suggestive of emission from an accretion disk. The central object must be degenerate because a larger object could not produce the observed luminosity without an unreasonably large mass infall rate.

In this scenario, the  $10^4\ \text{K}$  blackbody and the B9-A0 III spectrum could both arise from radiation from the inner, gaseous portions of the accretion disk. This model would explain several unusual characteristics of the spectrum of HD 44179. Greenstein and Oke (1977) were unable to fit any B type model atmosphere to its large Balmer jump. They further pointed out the inconsistency of a spectral class of late B with the appearance of the O I and C I absorption lines reported by Cohen et al. (1975). The bizarre ultraviolet spectrum of HD 44179, with its emission and absorption features of CO and related carbon molecules (Sitko 1983) represents yet another inconsistency with a classification of late B. Accretion disk models naturally produce a variety of spectral features which cannot be reconciled with a single spectral type.

The tremendous velocity widths observed by Sitko (1983) of  $1000\ \text{km s}^{-1}$  imply that the escape velocity from the central object must be much larger than that appropriate to a normal late B giant. Furthermore, the H and K absorption lines observed by Cohen et al. (1975) are redshifted with respect to the star by  $30\ \text{km s}^{-1}$ ,

suggesting infall in the line of sight toward HD 44179. These kinematic features fit easily into our picture of an accretion disk around a degenerate object.

## **5. Summary**

For several reasons, we believe we have observed the evolution of the particles responsible for the UIR emission features in the outflow from HD 44179. There is no UIR emission in the immediate vicinity of the central continuum source, suggesting that the UIR carriers have not yet formed this close to the outflow source. The peak wavelength of the  $7.7\text{ }\mu\text{m}$  feature appears to shift to shorter wavelengths further from HD 44179, indicating a change in the nature of the emitting material. The drop in relative significance of the  $7.7\text{ }\mu\text{m}$  feature from 1 to 2 arcsec from HD 44179 suggests the material may be growing increasingly hydrogenated as it evolves. This idea is further strengthened by the enhancement of the  $11.3\text{ }\mu\text{m}$  feature at these distances and its decline in strength relative to the  $8.6$  and  $12.7\text{ }\mu\text{m}$  features further away.

A model of HD 44179 as an accretion disk around a degenerate object would eliminate many difficulties with present models and explain all of the observed properties of the Red Rectangle in terms of one simple model.

## **Acknowledgements**

We are grateful to R. Canterna for providing the computer facilities on which we analyzed our data. H.M. Dyck made many valuable comments on the manuscript. Astronomy at WIRO is supported by the State of Wyoming and the Air Force Office of Scientific Research.

## References

- Allamandola, L.J., Tielens, A.G.G.M., & Barker, J.R., 1985, *ApJ*, **290**, L25.  
 ———, 1989, *ApJ Suppl.*, **71**, 773.  
 Blanco, A., Bussoletti, E., & Colangeli, L., 1988, *ApJ*, **334**, 875.  
 Bregman, J.D., 1989, in *Interstellar Dust*, ed., L.J. Allamandola & A.G.G.M. Tielens (Dordrecht: Kluwer), 109.  
 Bregman, J.D., Allamandola, L.J., Tielens, A.G.G.M., Witteborn, F.C., Rank, D.M., & Wooden, D., 1986, *Summer School on Interstellar Processes: Abstracts of Contributed Papers* (Moffett Field, CA: NASA), 117.  
 Cohen, M., et al., 1975, *ApJ*, **196**, 179.  
 Cohen, M., Allamandola, L., Tielens, A.G.G.M., Bregman, J., Simpson, J.P., Witteborn, F.C., Wooden, D., & Rank, D., 1986, *ApJ*, **302**, 737.  
 Cohen, M., Tielens, A.G.G.M., & Allamandola, L.J., 1985, *ApJ*, **299**, L93.  
 Cohen, M., Tielens, A.G.G.M., Bregman, J., Witteborn, F.C., Rank, D.M., Allamandola, L.J., Wooden, D.H., & de Muizon, M., 1989, *ApJ*, **341**, 246.  
 Cohen, M., Walker, R.G., & Witteborn, F.C., 1992, *AJ*, **104**, 2030.  
 Dainty, J.C., Pipher, J.L., Lacasse, M.G., & Ridgway, S.T., 1985, *ApJ*, **293**, 530.  
 Duley, W.W., & Williams, D.A., 1981, *MNRAS*, **196**, 269.  
 Geballe, T.R., Tielens, A.G.G.M., Allamandola, L.J., Moorhouse, A., & Brand, P.W.J.L., 1989, *ApJ*, **341**, 278.  
 Gillett, F.J., Forrest, W.J., & Merrill, K.M., 1973, *ApJ*, **183**, 87.  
 Grasdalen, G.L., Sloan, G.C., & LeVan, P.D., 1992, *ApJ*, **384**, L25. (Paper I)  
 Greenstein, J.C., & Oke, J.B., 1977, *PASP*, **89**, 131.  
 Gull S.F., & Skilling, J., 1984, *Proc. I.E.E.*, **131**, 646.  
 ———, 1989, *Quantified Maximum Entropy "MEMSYS 3" Users' Manual* (London: Maximum Entropy Data Consultants Ltd.).  
 Jones, A.P., Duley, W.W., & Williams, D.A., 1990, *QJRAS*, **31**, 567.  
 Landau, R., Grasdalen, G., & Sloan, G.C., 1992, *A&A*, **259**, 696.  
 Léger, A., d'Hendecourt, L., & Défourneau, D., 1989, *A&A*, **216**, 148.  
 Léger, A., & Puget, J.L., 1984, *A&A*, **137**, L5.  
 Leinert, Ch., & Haas, M., 1989, *A&A*, **221**, 110.  
 LeVan, P.D., 1990, *PASP*, **102**, 190.  
 Rowan-Robinson, M., & Harris, S., 1983, *MNRAS*, **202**, 767.  
 Sakata, A., Wada, S., Tanabé, T., & Onaka, T., 1984, *ApJ*, **287**, L51.  
 Sakata, A., Wada, S., Onaka, T., & Tokunaga, A.T., 1987, *ApJ*, **320**, L63.  
 ———, 1990, *ApJ*, **353**, 543.  
 Sellgren, K., 1984, *ApJ*, **277**, 623.  
 Sitko, M.L., 1983, *ApJ*, **265**, 848.  
 Sloan, G.C., Grasdalen, G.L., & LeVan, P.D., 1993, *ApJ*, **404**, 328. (Paper II)  
 Thronson, H., 1982, *AJ*, **87**, 1027.  
 Walker, R., & Price, S.D., 1975, *AFCRL Infrared Sky Survey*, AFCRL-TR-75-0373. ADA016397

Witteborn, F.C., Sandford, S.A., Bregman, J.D., Allamandola, L.J., Cohen, M.,  
Wooden, D.H., & Graps, A.L., 1989, *ApJ*, **341**, 270.  
Zuckerman, B., Gilra, D.P., Turner, B.E., Morris, M., & Palmer, P., 1976, *ApJ*,  
**205**, L15.

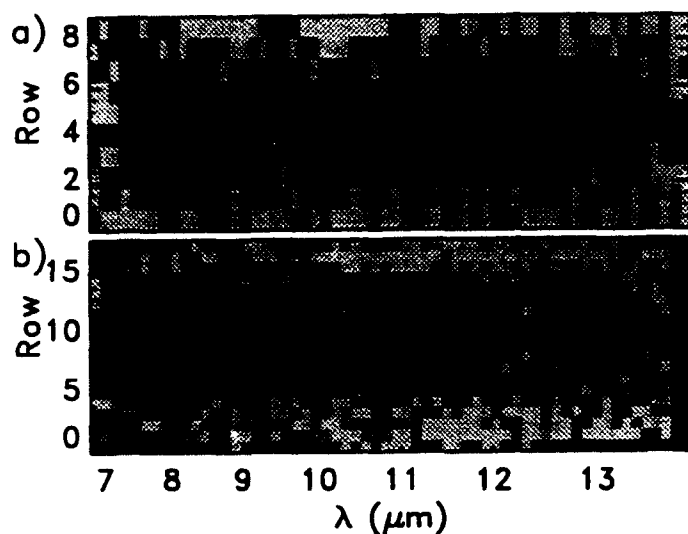


Figure 1. The results of MEMSYS maximum entropy reconstruction, illustrated by plotting the logarithm of the flux with grey-scale images. (a) A single HD 44179 image before reconstruction. (b) The sum of 20 reconstructed HD 44179 images from our second set of data. The reconstruction re-gridded the original 10-row data onto 19 rows and corrected for the angle between the dispersion axis and the array apparent in the top panel. The extended nature of the UIR features is evident in the reconstruction.

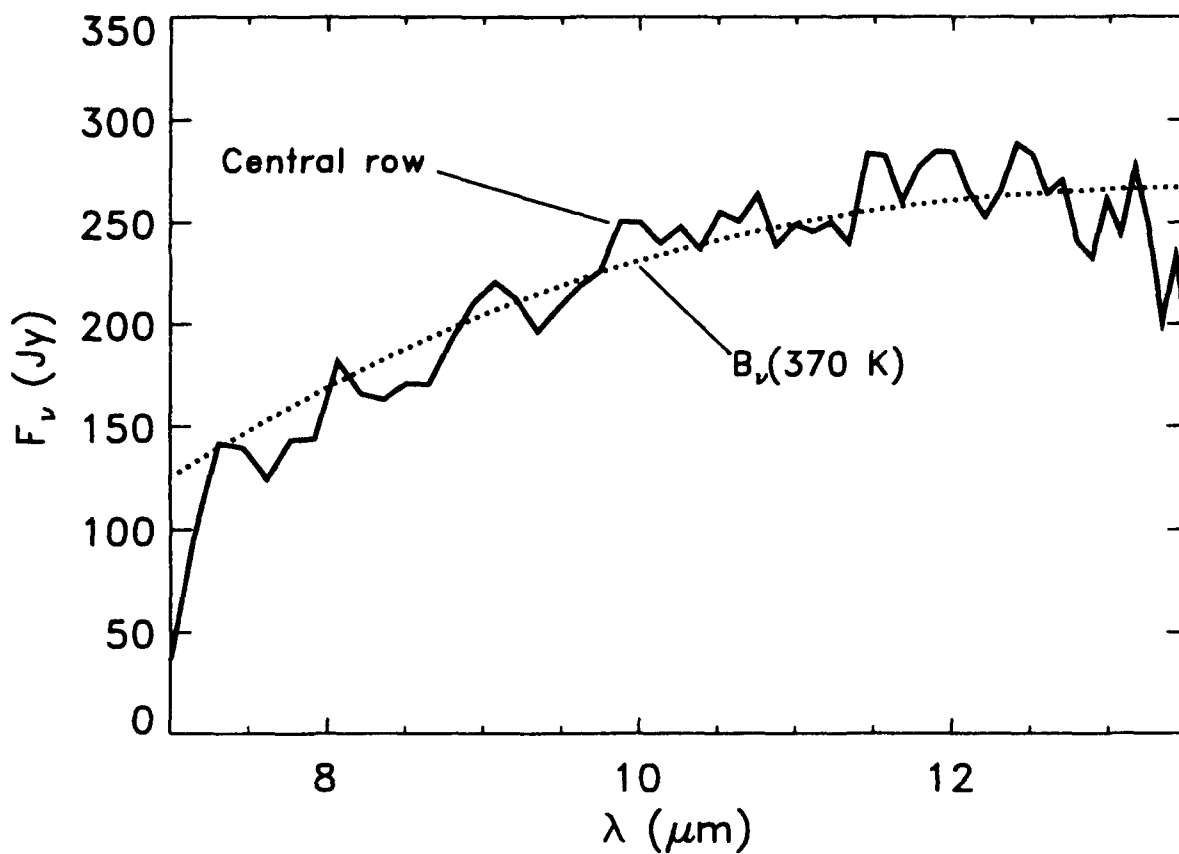


Figure 2. Comparison of the spectrum from the central row of our reconstruction of one set of HD 44179 images (solid line) with a 370 K blackbody (dotted line).

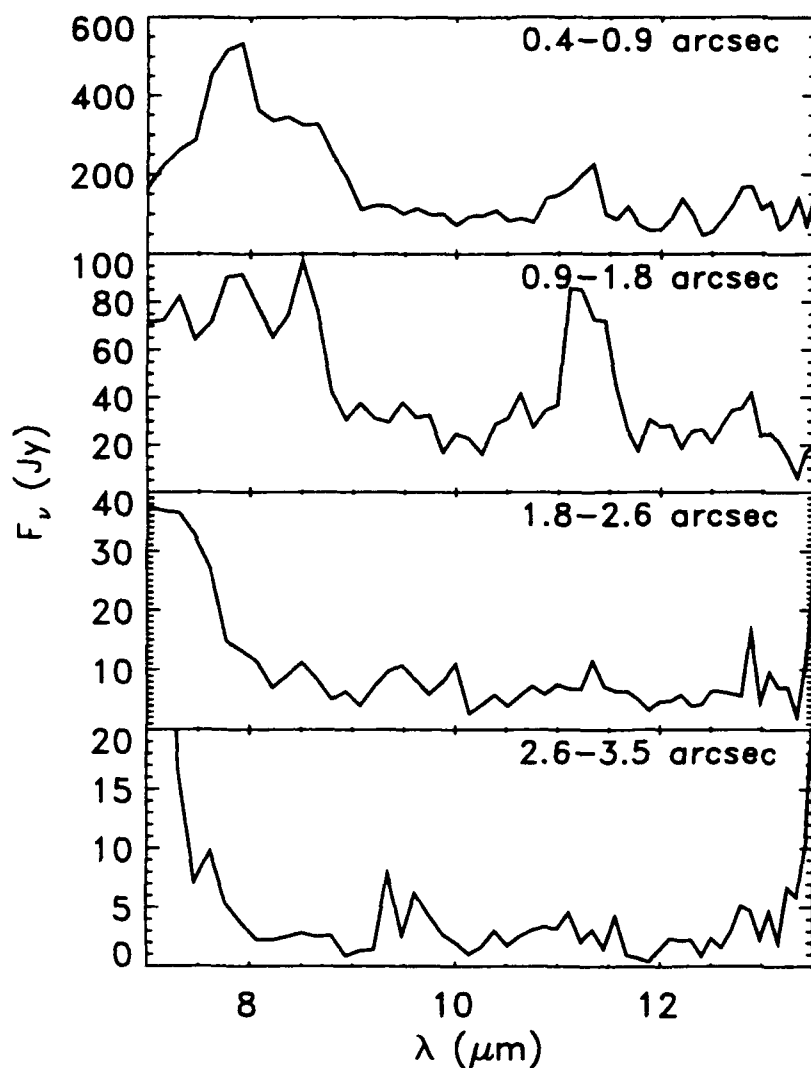


Figure 3. Spectra of emission from the Red Rectangle, moving from near HD 44179 (top) to the edge of the slit (bottom). Each spectrum is the sum of 8 individual spectra: 2 adjacent rows on each side of the central source from both data sets. The exception is the top spectrum, which does not include the contribution from the rows adjacent to the central source in the set of images with the poorer focus.



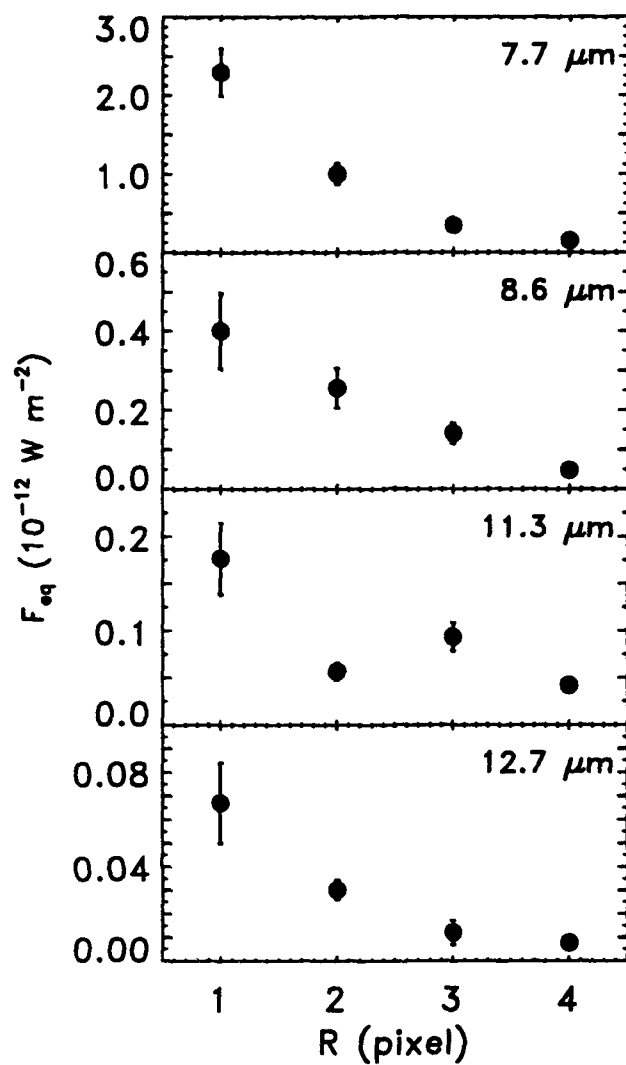


Figure 4. The flux of the four UIR features plotted against distance from the central source. One pixel is 0.44 arcsec in the reconstructions.



## **Appendix I**

### **Maximum Entropy Reconstruction Techniques for Long-Slit Spectroscopy**

**MAXIMUM ENTROPY  
RECONSTRUCTION TECHNIQUES  
FOR LONG-SLIT SPECTROSCOPY<sup>1</sup>**

G.C. Sloan<sup>2</sup>

Department of Physics and Astronomy, University of Wyoming  
P.O. Box 3905, Laramie, WY 82071

G.L. Grasdalen

G-star Enterprises

286 S. Pennsylvania, Denver, CO 80209

To be submitted to: *Astronomy and Astrophysics* (1993)

---

<sup>1</sup>Contribution 138 of the Wyoming Infrared Observatory

<sup>2</sup>Present Address: Phillips Laboratory/GPOB, 29 Randolph Road,  
Hanscom AFB, MA 01731-3010

## **Abstract**

We describe an algorithm for applying maximum entropy techniques to long-slit 10  $\mu\text{m}$  spectroscopic images. A good description of the point spread function (PSF), which varies strongly with wavelength at 10  $\mu\text{m}$ , is essential. We found that fitting a model analytical profile to observations of a point source at each wavelength provides the best description of the PSF. Our best analytical profile is the sum of a gaussian and exponential. We tested our algorithm on unresolved stars and found that the reconstructions are very close to point sources. Further tests performed with synthetic images show that our algorithm can fully resolve objects separated by more than 1 arcsec.

*Subject headings:* infrared: spectra — image processing

## 1. Introduction

Maximum entropy reconstruction techniques have proven to be an effective method of improving the spatial quality of astronomical images by correcting for the effects of atmospheric seeing and diffraction from the telescope and instrument. At the Wyoming Infrared Observatory (WIRO), these techniques have been applied to raster-scanned infrared images (e.g. Bentley et al. 1984, Dietz et al. 1989) using techniques described by Grasdalen, Hackwell, and Gehrz (1983). More recently at WIRO, the maximum entropy algorithm of Gull and Skilling (1984, 1989) has been applied to IRAS survey and pointed observations (Hackwell et al. 1988; Canterna et al. 1989, 1992).

With the advent of digital long-slit infrared spectrometers, the need for an application of maximum entropy techniques to two-dimensional spectroscopic images has arisen. A key requirement of any maximum entropy algorithm is an adequate description of the point spread function (PSF). For spectroscopic data, determining the behavior of the PSF with wavelength makes the maximum entropy problem very different than for standard images. The nature of the PSF can change dramatically with wavelength, so the PSF must be modeled at all wavelengths covered by the spectrometer.

The Geophysics Laboratory Array Detector Spectrometer (GLADYS) is a long-slit spectrometer which is used with the 2.3 m telescope at WIRO to observe spectra from 7 to 14  $\mu\text{m}$ . GLADYS uses a NaCl prism to disperse infrared radiation onto an array of Si:Ga photoconductors. In its present configuration, GLADYS uses a  $10 \times 62$  pixel area of the array, with the 10-pixel axis oriented along the slit. A more thorough description of GLADYS can be found in LeVan (1990).

The pixel spacing along the slit is 0.88 arcsec per pixel, on the order of the Airy disk from the telescope at 10  $\mu\text{m}$ , so GLADYS images are spatially undersampled. Many objects are spatially extended on the order of 1-2 arcsec and are thus marginally resolvable. By applying maximum entropy techniques to the data from GLADYS, we can improve the spatial resolution to study small-scale spatial variations in the spectra of extended objects. Maximum entropy reconstruction offers several other advantages as well.

None of the key optical axes in GLADYS are aligned exactly with the array axes. The dispersion axis is slightly inclined to the spectroscopic axis of the array, shifting about 1 pixel from one side of the array to the other. Lines of constant wavelength are not orthogonal to either array axis. Any standard technique to re-orthogonalize the data would require some type of interpolation routine to estimate values for the data in the new coordinate system, which would degrade the resolution.

While the 2.3 m telescope at WIRO tracks very accurately, it is impossible to completely eliminate all motion of an object in the slit during an integration. To combine several images together would require a shift-and-add procedure, which again would require interpolation and a reduction of resolution.

We have chosen to use the MEMSYS reconstruction method of Gull and Skilling (1984, 1989), which has been used at WIRO previously to reconstruct IRAS survey and pointed observations (Canterna et al. 1989, 1992). When we use MEMSYS to remove the effects of the PSF, we can also re-orthogonalize the data without interpolation. Because we can shift the reconstructed image to any desired position in the reconstructed data matrix, a shift-and-add procedure is unnecessary to co-add the data.

## **2. The MEMSYS Algorithm for GLADYS Images**

The MEMSYS algorithm requires that the user provide a means of convolving a test image with the PSF. We perform this task by supplying what we refer to as a "kernel," a surface consisting of the one-dimensional PSF in each column (at each wavelength) of our array. The variations in the character of the PSF from 7 to 14  $\mu\text{m}$  are quite dramatic. Figure 1 illustrates the width of the PSF, determined by fitting a gaussian profile to each wavelength of a GLADYS image of  $\alpha$  Tau. In general, the PSF grows wider with increasing wavelength.



We obtain the data for the kernel by observing a bright point source close to our program object in the sky. After several images, the slow drifting of the source along the slit provides us with a large number of samples of the PSF across each pixel, offset by a fraction of a pixel from one another. The net effect is to produce a heavily oversampled characterization of the PSF at each wavelength.

To determine the precise location of an object in the slit, we must first find the fractional pixel position of the center of the PSF at each wavelength. We perform this task by fitting a gaussian to the spatial profile of the object in each column. Figure 2 illustrates the behavior of the center of the PSF with wavelength for a typical image. We then fit a line to the centers of the PSF across the array to find the fractional pixel location of the object in the slit. We do this for each image containing PSF data to find the relative offsets.

Our initial method of constructing empirical kernels was to correct the point source data for the offsets in each image and simply bin the result. The results of this method are plotted in Figure 3, along with the raw point source data. Figure 4 illustrates the appearance of a kernel produced in this manner; it is only a rough approximation of the actual PSF at each wavelength. It suffers from noise in the side rows, which limits the quality of the reconstructions. In addition, since the kernel extends over more space than our slit covers, we were forced to set all values of the kernel outside the slit to zero.

To produce better reconstructions, a more realistic kernel is needed. For this reason, we decided to model the PSF at each wavelength with a test function and use this to produce the kernel. Our initial function, a gaussian, proved inadequate. While it fits the inner core which contains most of the flux, it underestimates the wings of the distribution. The best function we found was a sum of a gaussian (to fit the inner core) and an exponential (to fit the wings):

$$F(x) = a_1 e^{-(x-x_0)^2/2\sigma_1^2} + a_2 e^{-|x-x_0|/a_2}.$$

We used the downhill simplex method (Press et al. 1988) to fit this function to the point source data at each wavelength, minimizing the sum of the squares of the differences. The five parameters we fit are the position of the star ( $x_0$ ), the amplitude of the gaussian and the exponential ( $a_1$  and  $a_2$ ), and their widths ( $\sigma_1$  and  $\sigma_2$ ). We typically ran the simplex three or more times, using the results of the previous run as the starting point for the next. We chose as the best fit that with the least associated error and repeated this process for each wavelength in our data.

The solid lines in Figure 3 represent our best fit to the data at two wavelengths. At the longer wavelength, the difference between the two methods is more obvious, because the lower signal/noise ratio affects the binning method more strongly than the fitting method. Figure 5 illustrates the kernel which results from this method. It is clearly smoother, and we believe it more accurately reflects the nature of the PSF and its behavior with wavelength. Another advantage to the

fitting method is that we can extrapolate beyond the edge of the slit; we aren't forced to truncate the kernel beyond a certain point.

Figure 6 compares reconstructions using the two kernels. We have mapped the reconstruction of the 10-row input image onto 19 rows. In the input data, each row spans 0.88 arcsec, while in the output, a row covers only 0.44 arcsec. As Figure 6 demonstrates, smoothing the kernel has a dramatic impact on the quality of our reconstructions for extended sources such as  $\alpha$  Ori.

In addition to removing the effects of the PSF from the data, our kernel also allows the MEMSYS algorithm to re-orthogonalize the images and shift each of them to the same position on the array. The kernel provides a thorough description of how a point-source spectrum is affected by the atmosphere, telescope, and instrument. By misaligning the centers of the PSF in our kernel as they are in our data, we force MEMSYS to re-align the reconstructions. The shift in position of the PSF with wavelength is apparent in Figures 4 and 5. Similarly, by moving the entire PSF across the kernel, we also force MEMSYS to correct for the relative position of an object in the slit. For each image we wish to reconstruct, we determine the offset of the object in the slit and shift the PSF the same amount in the kernel. To remove the misalignment of a line of constant wavelength, we convolve the kernel with a 3-column matrix which effectively tilts a given spatial profile to the misalignment angle.

Another important input to the MEMSYS routine is a noise map, which MEMSYS uses to constrain the reconstructed data. When we record a GLADYS image at the telescope, we save the mean and uncertainty of several frames from the instrument. For pixels exposed to bright sources, the uncertainty is usually larger than for pixels exposed to sky or fainter sources because of seeing and transmission effects. We have found that integrating on the sky produces a map of the inherent noise in each pixel suitable for use with MEMSYS. This noise map is fairly constant from one night to the next.

Our present algorithm only corrects for blurring along the slit (i.e. spatial blurring). We have made no attempt to improve the spectral resolution of our data by correcting for blurring in the wavelength direction, which arises from a variety of sources, including motion of the object across the slit, seeing effects, telescope diffraction, and instrumental diffraction. To describe the two-dimensional nature of the PSF, we would have to observe a monochromatic point source in the lab, or a point-like emission line source at the telescope. To fully determine the behavior of the two-dimensional PSF with wavelength, this would need to be done at several wavelengths.

### 3. Discussion

We tested our algorithm by processing images of unresolved stars such as  $\alpha$  Tau and  $\beta$  Gem. In all cases, the reconstructed image had virtually all the flux in one row (see Figure 6, panel b), exactly what would be expected for a point source.

We tested the sensitivity and resolving ability of our algorithm by processing synthetic images generated from data of  $\alpha$  Tau. One synthetic image consisted of the sum of a GLADYS image and two secondary images generated from the first by multiplying by 0.1 and shifting one pixel up or down the slit. This image resembled what one would expect from a star with two faint emission sources 1 arcsec to either side. We generated a second synthetic image with the faint emission 2 arcsec to either side of the central spectrum.

Figure 7 illustrates the results of our tests (again, we map 10 input rows onto 19 output rows). MEMSYS had no difficulty resolving the side spectra spaced 2 arcsec away. However, the reconstructions of the synthetic image with 1-arcsec spacing were less successful. While the reconstructed image is not a point source, MEMSYS did not place the side emission 2 rows away from the central source as it should have. Instead it placed it only one row (0.44 arcsec) away.

MEMSYS is a conservative algorithm; it will generate no more structure than necessary to fit the data within the noise. The spacing of the test image with 2-

arcsec separation was sufficiently large compared to the size of the PSF that MEMSYS was forced to place the emission away from the central source. In the test with 1-arcsec separation, however, the spacing was only on the order of the size of the PSF and MEMSYS instead shifted the emission even closer to the central source to avoid creating any more structure than necessary.

Maximum entropy techniques do not produce images with uniform resolution. In general, the lower the signal/noise ratio in a portion of an image, the larger the resolution element. Because our spectroscopic data cover such a large range of wavelengths, we must also pay attention to the dependence of the width of the PSF (and thus the resolution element) on wavelength. In general, the width of the PSF increases with wavelength, although it is also larger wherever the atmospheric transmission is low (Figure 1). This effect is significant at both the long and short wavelength edges of the 10  $\mu\text{m}$  window and within the telluric ozone absorption feature at 9.5  $\mu\text{m}$ . Since the signal/noise is also a function of the atmospheric transmission, the resolution of a reconstruction strongly depends on wavelength.

All of the images we have used with maximum entropy reconstruction were taken in 1991 February. Our observing technique at that time was adequate for these purposes, but experience with maximum entropy reconstruction has allowed us to improve it somewhat. To produce good reconstructions, it is essential to obtain high quality observations of a calibration source in order to accurately determine the

behavior of the PSF with wavelength. Ideally, the same object can serve as both a spectrophotometric and point source reference. The signal/noise ratio of the point source observations should be as good as that of the program object. Both the program object and the point source reference should be observed at about the same air mass. Because of the strong temporal variations of atmospheric transmission and seeing at 10  $\mu\text{m}$ , it is very important to observe point source data as close in time to program observations as possible. We suggest that observations of the program source and calibration source be interleaved.

We hope to improve our algorithm by correcting for blurring in the spectral direction. This modification will increase our spectral and spatial resolution, but will require a three-dimensional kernel for the MEMSYS code which will substantially increase computational time. Our present reconstructions typically take 5 minutes per image on a Sun work-station.

Another complication arises from changes of the position of an object across the slit from one image to the next. This motion has the effect of offsetting the spectrum in the spectroscopic direction. While the effects are subtle, they do complicate corrections for atmospheric and instrumental transmission, which we perform by dividing a program spectrum by a calibration spectrum. If the two spectra are shifted in the wavelength direction from one another, this division will not completely correct

for transmission. Once we implement a three-dimensional kernel, we plan to include a wavelength shift to correct this problem.

We have applied our present MEMSYS algorithm to observations of  $\alpha$  Ori and HD 44179. The results of these reconstructions are published separately (Sloan, Grasdalen, and LeVan 1993a, 1993b) and have proven very successful.

### **Acknowledgements**

We are grateful to P. LeVan and R. Canterna for their many comments on the manuscript. R. Canterna provided use of computer facilities and software used to develop our maximum reconstruction algorithm. Astronomy at WIRO is supported by the State of Wyoming and the Air Force Office of Scientific Research.



## References

- Bentley, A.F., Hackwell, J.A., Grasdalen, G.L., & Gehrz, R.D., 1984, *ApJ*, **278**, 665.
- Canterna, R., Hackwell, J.A., & Grasdalen, G.L., 1989, in *The Interstellar Medium in External Galaxies: Summaries of Contributed Papers* (Washington: NASA), 301.
- Canterna, R., Hackwell, J.A., Hermann, R., & Grasdalen, G.L., 1992, *AJ*, submitted.
- Dietz, R.D., Gehrz, R.D., Jones, T.J., Grasdalen, G.L., Smith, J., Gullixson, C., & Hackwell, J.A., 1989, *AJ*, **98**, 1260.
- Grasdalen, G.L., Hackwell, J., & Gehrz, R.D., 1983, *Topical Meeting on Information Processing in Astronomy and Optics* (Optical Society of America).
- Gull S.F., & Skilling, J., 1984, *I.E.E. Proc.*, **131**, 646.
- \_\_\_\_\_, 1989, *Quantified Maximum Entropy "MEMSYS 3" Users' Manual* (London: Maximum Entropy Data Consultants Ltd.).
- Hackwell, J.A., Friesen, L.M., Canterna, R., & Grasdalen, G.L., 1988, *BAAS*, **20**, 667.
- LeVan, P.D., 1990, *PASP*, **102**, 190.
- Press, W.H., Flannery, B.P., Teukolsky, S.A., & Vetterling, W.T., 1988, *Numerical Recipes in C: The Art of Scientific Computing* (Cambridge: Cambridge Univ. Press).
- Sloan, G.C., Grasdalen, G.L., & LeVan, P.D., 1993a, *ApJ*, **404**, 328.
- \_\_\_\_\_, 1993b, *ApJ*, **409**, in press.

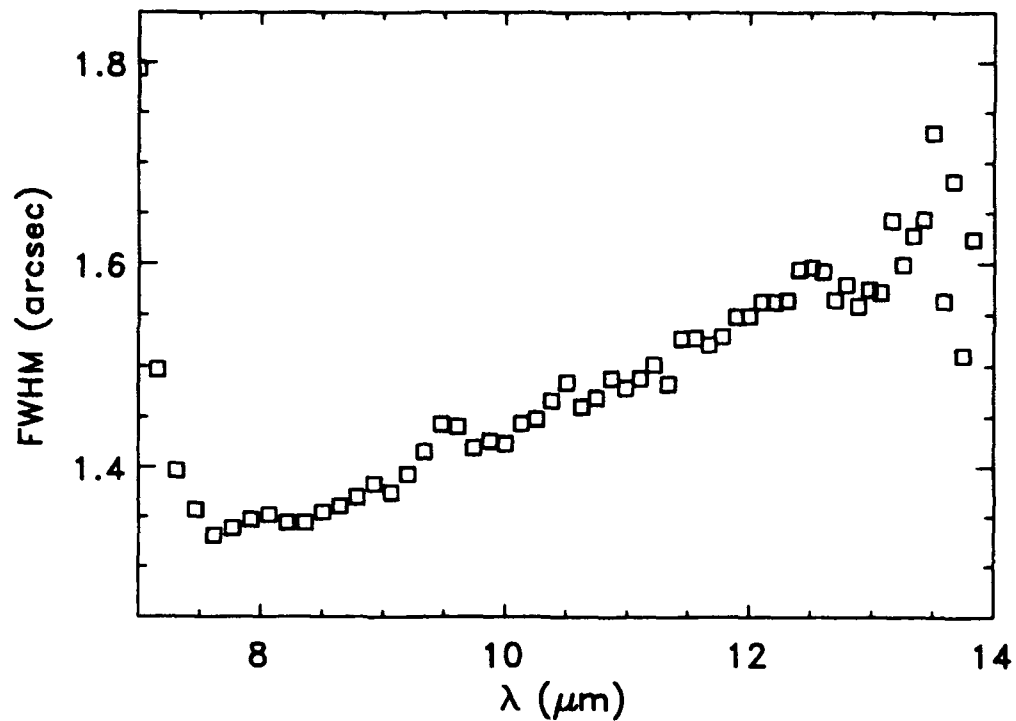


Figure 1. A spatiogram, or plot of width versus wavelength, for observations of  $\alpha$  Tau. The width of  $\alpha$  Tau has been determined by fitting a gaussian profile to the spatial profile at each wavelength. While the width of a point source generally increases with wavelength from 7 to 14  $\mu\text{m}$ , the width also increases where the transmission is low (at both edges of the window and in the telluric ozone absorption feature at 9.5  $\mu\text{m}$ ).

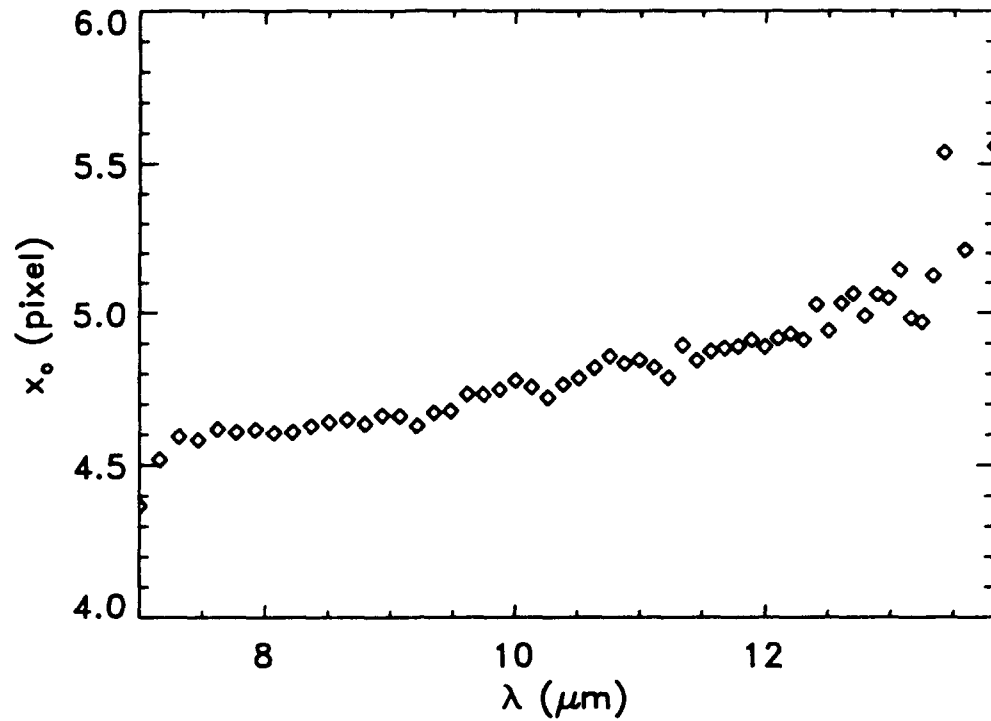


Figure 2. The position of  $\alpha$  Tau with wavelength in a GLADYS image. At each wavelength, a gaussian has been fit to the spatial profile to determine the position of the object ( $x_o$ ). This plot illustrates the misalignment of the dispersion axis with the spectroscopic axis of the array.

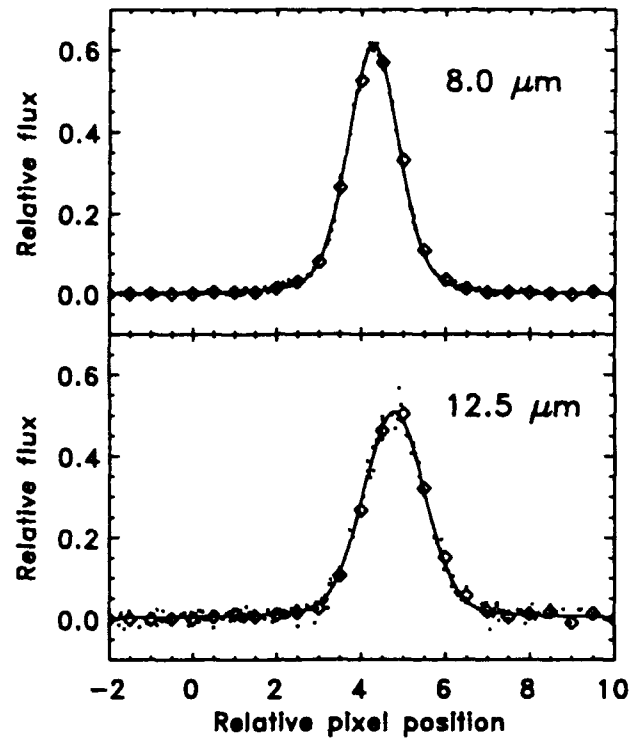
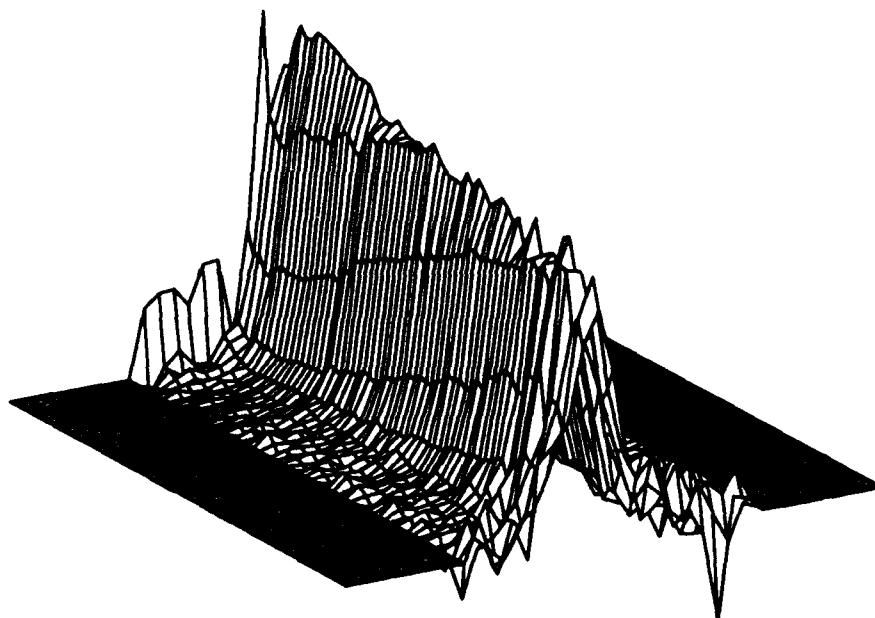
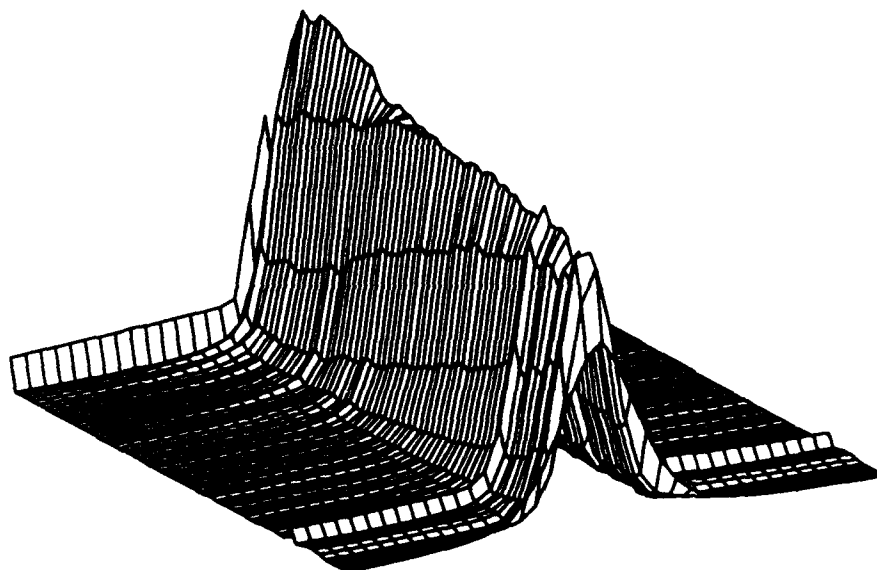


Figure 3. Sample profiles of a point source from our observations of  $\alpha$  Tau (dots). The diamonds represent the results of the binning method. The solid lines are the best fits of our model function. The difference between the two methods is much more significant at longer wavelengths, where the point source data are noisier.



**Figure 4.** A sample kernel constructed using the binning method. Wavelength runs from 7  $\mu\text{m}$  at the back of the surface to 14  $\mu\text{m}$  at the front. The horizontal axis represents position in the slit. At each wavelength, a spatial cut gives our estimate of the PSF. The field of zeros on either side of the kernel results from a lack of data beyond the edges of the slit.



**Figure 5.** A sample kernel constructed by fitting our model function to the point source data at each wavelength. This kernel is much smoother than the one in Figure 4. The axes are defined as in Figure 4.

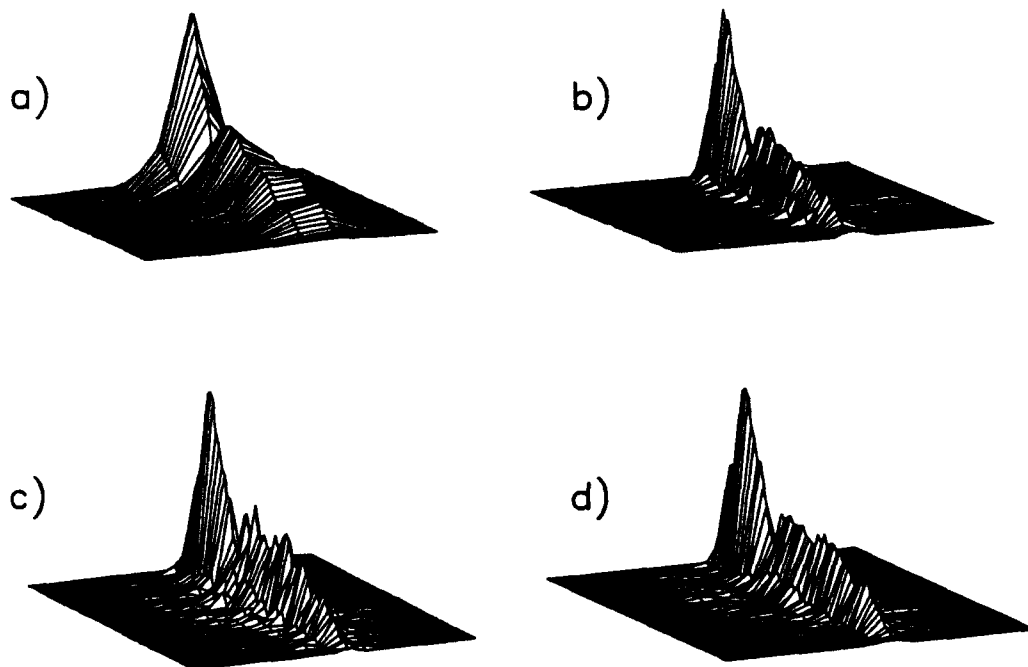


Figure 6. A comparison of reconstructions. The axes are defined as in Figure 4. (a) An image of  $\alpha$  Ori before reconstruction. The deep trough at  $9.5\ \mu\text{m}$  results from strong telluric ozone absorption. (b) A reconstruction of  $\alpha$  Tau. It is very close to a point source. (c) A reconstruction of  $\alpha$  Ori using the kernel illustrated in Figure 4. (d) A reconstruction of  $\alpha$  Ori using the kernel in Figure 5. This reconstruction is much cleaner than the one in panel (c); it is clearly not a point source. The emission in the row adjacent to the central row and the side rows further out arises from circumstellar silicate material (Sloan, Grasdalen, and LeVan 1993a).

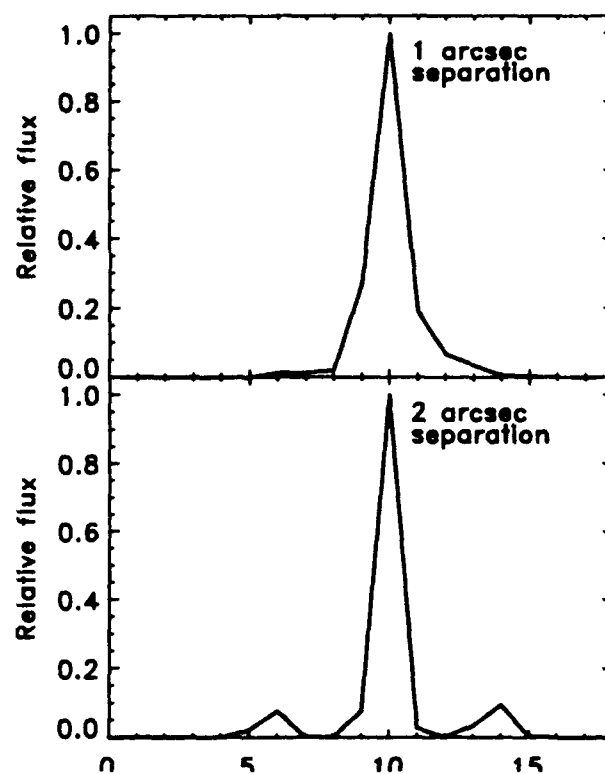


Figure 7. Results of reconstructions of synthetic images with faint emission one arcsec (top) and two arcsec (bottom) on either side of a bright central source. We have plotted the profile of the reconstruction summed from 10 to 11  $\mu\text{m}$ . The bottom panel shows that the MEMSYS routine can resolve objects spaced 2 arcsec apart. The top panel shows that the reconstruction is clearly broader than a point source, but just at the edge of the resolution of the algorithm.